

PEM Fuel Cell Fundamentals

Xiao-Zi Yuan and Haijiang Wang

1.1 Overview

1.1.1 Introduction

A fuel cell is an electrochemical device that continuously and directly converts the chemical energy of externally supplied fuel and oxidant to electrical energy. Fuel cells are customarily classified according to the electrolyte employed. The five most common technologies are polymer electrolyte membrane fuel cells (PEM fuel cells or PEMFCs), alkaline fuel cells (AFCs), phosphoric acid fuel cells (PAFCs), molten carbonate fuel cells (MCFCs) and solid oxide fuel cells (SOFCs). However, the popularity of PEMFCs, a relatively new type of fuel cell, is rapidly outpacing that of the others.

Unlike most other types of fuel cells, PEMFCs use a quasi-solid electrolyte, which is based on a polymer backbone with side-chains possessing acid-based groups. The numerous advantages of this family of electrolytes make the PEM fuel cell particularly attractive for smaller-scale terrestrial applications such as transportation, home-based distributed power, and portable power applications. The distinguishing features of PEMFCs include relatively low-temperature (under 90 °C) operation, high power density, a compact system, and ease in handling liquid fuel.

1.1.1.1 A Brief History of PEM Fuel Cells

Invention of the Fuel Cell—1839

The idea of the gaseous fuel cell can be traced back to Sir William Grove, a Welsh judge, inventor, and physicist, who is recognized as “the father of the fuel cell.” A reproduction of his drawing of a fuel cell, from 1838, can be seen in Figure 1.1. In 1839 Grove found that electrolysis (using electricity to split water into hydrogen and oxygen) could be performed in reverse with the right catalyst, producing electricity. In 1842, Grove developed a stack of 50 fuel cells, which he called a “gaseous voltaic battery”. However, for almost a century after Grove’s discovery

the fuel cell did not make any practical progress, remaining only a scientific curiosity.

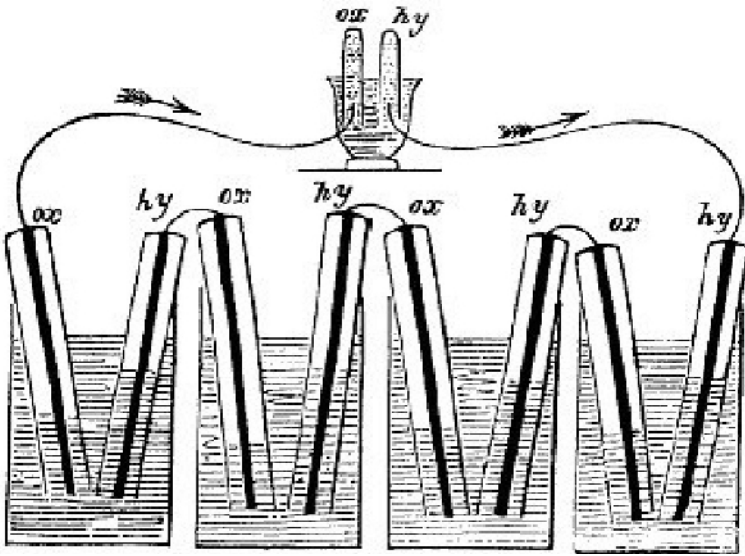


Figure 1.1. The first fuel cell. (Originally printed in Grove, W. R. (1838). On a new voltaic combination. *Philosophical Magazine and Journal of Science* 13, 430.)

In 1937, Francis T. Bacon, an Englishman, started to work on practical fuel cells. By the end of the 1950s [1] he had developed a 40-cell stack capable of 5 kW. The stack was able to power a welding machine, circular saw, and forklift.

PEM Fuel Cell Development—1960s

The PEM fuel cell was invented at General Electric (GE) in the early 1960s, through the work of Thomas Grubb and Leonard Niedrach. Initially, sulfonated polystyrene membranes were used as the solid electrolytes, but these were soon replaced by Nafion® membranes in 1966. The Nafion membrane has proved to be superior in performance and durability, and it is still the most popular membrane in use today.

Gemini Space Program—1950–1970

PEM fuel cell technology served as part of NASA's Gemini Program (Figure 1.2), the main objective of which was to test equipment and procedures for Apollo. GE's PEM fuel cells were selected, but the earliest model PB2 cell repeatedly encountered technical difficulties, including internal cell contamination and leakage of oxygen through the membrane. Gemini I through IV flew with batteries instead. Due to PB2's malfunctions and poor performance, a new model, P3, was designed. The first mission to utilize PEMFCs was Gemini V. However, they were replaced by alkaline fuel cells in the Apollo program and in the space shuttle. This delayed the development of PEM fuel cells for a decade [2, 3].

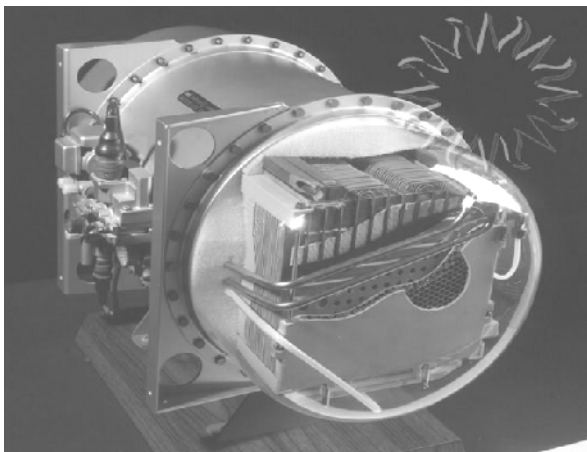


Figure 1.2. Gemini space mission used fuel cells. (Image courtesy of NASA.)

Ballard Breakthrough—1980–2000

Due to their high cost, fuel cell systems were limited to space missions and other special applications. It was not until the late 1980s and early 1990s, when research by Ballard Power Systems (founded in 1979) resulted in a resurgence in interest in PEMFCs and the development of fuel cells, that fuel cells became a real option for wider applications. In 1983, Ballard began developing PEM fuel cells. Proof-of-concept fuel cells followed, and sub-scale and full-scale prototype systems (Figure 1.3) were developed to demonstrate the technology. Their milestones in the 1990s are as follows:

Mk900 (2000)	Mk800 (1997)	Mk700 (1995)	Mk500 (1993)	Mk300 (1991)
80 kW	50 kW	25 kW	10 kW	5 kW

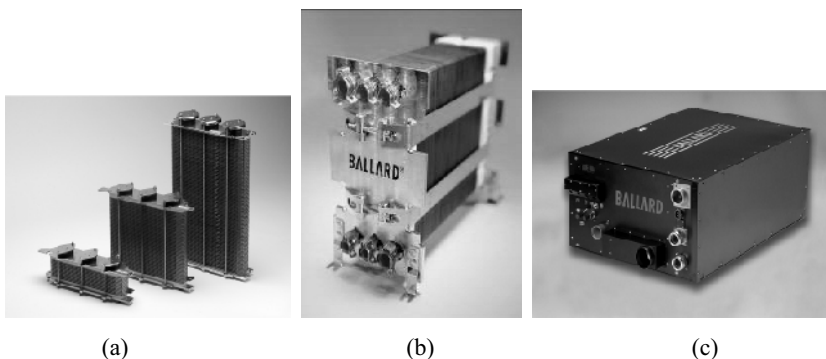


Figure 1.3. Fuel cells produced by Ballard Power Systems. (a) Mark1020 ACS™, (b) Mark1030™ V3, (c) Heavy-Duty Fuel Cell Module (HD6). (Images courtesy of Ballard Power Systems.)



Figure 1.4. A map of the Hydrogen Highway in British Columbia, Canada. (Image courtesy of BC Hydrogen Highway™.)

PEM Fuel Cells Today

Since interest in PEM fuel cell research and development has intensified, more and more universities and institutes all over the world are becoming involved. So far several key innovations, such as low platinum catalyst loading, novel membranes, and new bipolar plates, make the application of PEMFC systems more or less realistic. Demonstration activities in every corner of the world are overwhelming. Figure 1.4 shows an example of a hydrogen and fuel cell demonstration project, the Hydrogen Highway in British Columbia, Canada. British Columbia's Hydrogen Highway is actually both a demonstration program and a market development program; it features an evolving network of hydrogen and fuel cell technologies, including vehicle fuelling infrastructure. The project leaders and participants come from British Columbia's hydrogen and fuel cell industries, government, industry associations, and academic institutions. Fully implemented in time for the 2010 Olympic and Paralympic Winter Games, the program will operate a fleet of 20 buses in Victoria and Whistler.

After the Canadian government announced funding for the world's first hydrogen highway, California's Governor Schwarzenegger committed to the building of a California Hydrogen Highway Network on a similar timescale, by signing an executive order creating a public/private partnership.

1.1.1.2 Principles of PEM Fuel Cells

The conversion of chemical energy to electrical energy in a PEM fuel cell occurs through a direct electrochemical reaction. It takes place silently without combustion. The key part of a PEM fuel cell, which is known as a membrane electrode assembly (MEA), consists of a polymer electrolyte in contact with an anode and a cathode on either side. To function, the membrane must conduct hydrogen ions (protons) and separate either gas to pass to the other side of the cell. A schematic representation of a PEM fuel cell is shown in Figure 1.5.

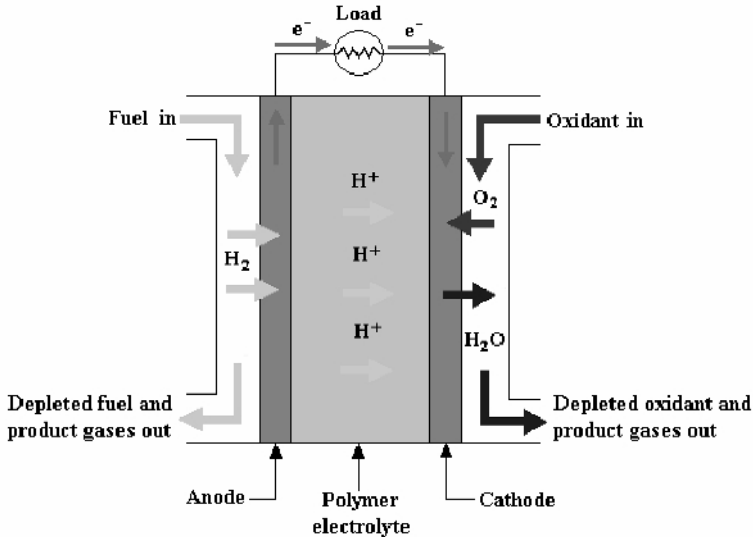


Figure 1.5. Diagram of PEM fuel cell principle

Unlike in a conventional battery, the fuel and oxidant are supplied to the device from external sources. The device can thus be operated until the fuel (or oxidant) supply is exhausted. As seen in Figure 1.5, on one side of the cell, hydrogen is delivered through the flow field channel of the anode plate to the anode. On the other side of the cell, oxygen from the air is delivered through the channeled plate to the cathode. At the anode, hydrogen is decomposed into positively charged protons and negatively charged electrons. Positively charged protons pass through the polymer electrolyte membrane (PEM) to the cathode, whereas the negatively charged electrons travel along an external circuit to the cathode, creating an electrical current. At the cathode, the electrons recombine with the protons, and together with the oxygen molecules, form pure water as the only reaction by-product, which flows out of the cell.

The splitting of the hydrogen molecule is relatively easy using a platinum catalyst. However, the splitting of the stronger oxygen molecule is more difficult, which causes significant activation loss. So far platinum is still the best option for the oxygen reduction reaction (ORR). Another significant source of performance loss is the resistance of the membrane to proton flow, which is minimized by making it as thin as possible (around 50 μm). Nevertheless, the PEM fuel cell is a

system whose successful operation with a high power output depends on all the sub-systems; its performance depends on components such as flow field design, catalyst, and membrane, and also on parameters such as temperature and humidity.

1.1.1.3 Single Cell, Stack, and System

Single Cell

A single PEM fuel cell includes only one anode and one cathode; therefore, the operating voltage of a single cell is less than 1 V. When it is operated under a given current, the voltage is even less. An acceptable performance for a state-of-the-art single cell is at least 1 A/cm² at a voltage of 0.6 V. Here are two examples of single cell designs.

An in-house fabricated single cell designed by the National Research Council of Canada Institute for Fuel Cell Innovation (NRC-IFCI) is shown in Figure 1.6. The single cell components include the bladder plate, piston, plastic plate, anode current collector, anode plate, gaskets, cathode plate, cathode current collector, and another plastic plate and bladder plate. The graphite plate/current collector are isolated from the aluminum end plate by a plastic plate, which also serves as a gas manifold. Gaskets are used to seal the MEA. A variable pressure bladder, controlled with nitrogen gas, is used to compress and seal the cell assembly. Cell heating is accomplished by two pairs of heat tape pieces. The inner 60 W heat tape, which is glued onto the copper current collector plates, allows the cell to operate at temperatures up to 120 °C.

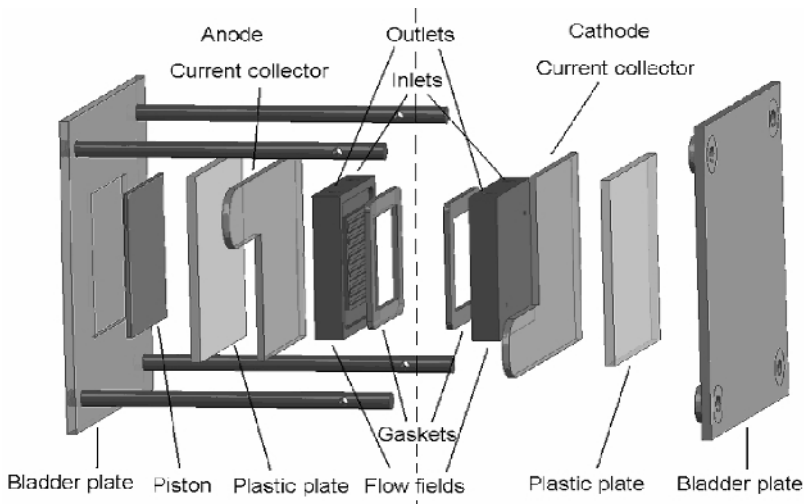


Figure 1.6. A single PEM fuel cell with an active area of 4.4 cm² designed by NRC-IFCI. (Reproduced by permission of ECS—The Electrochemical Society, from Tang Y, Zhang J, Song C, Liu H, Zhang J, Wang H, et al. Temperature-dependent performance and *in situ* AC impedance of high-temperature PEM fuel cells using the Nafion-112 membrane.)

Figure 1.7 shows the assembly diagram of a diagnostic modeling PEM fuel cell also designed by NRC-IFCI. The active area of this single cell is 192 cm². A

straight channel configuration is chosen for the cathode plate to simplify the modeling process, ease the integration of sensors, and result in a relatively small pressure drop. Two-path serpentine channels are used for the anode plate, with the coolant channels in the back covering the entire active area. Two additional plates are used in the assembly of the single cell. One is the end plate, which seals the coolant channels on the anode plate. It is a blank plate, void of any distribution channels or seal grooves, marked only by holes for the reactant gases, coolant, and alignment pin. The other is the coolant plate, which cools the cathode plate and consists of a hole for the alignment pin, a seal groove, and coolant channels. At one end of the distribution plates, the manifold has ports for the hose fittings to connect to the distribution channels in the various plates. The relatively soft insulating material is able to electrically isolate the fuel cell. Between the plates and the insulators are the current collectors, which have a high electrical conductivity. The main components of the compression hardware are the alignment plate, tie rods, tie rod screws, bushings, and compression plate and bladder. The compression plate and bladder provide the compression force. It is a pneumatic system allowing accurate control of the compressive force, which ensures proper sealing and guarantees that the MEA is in contact with the reacting gases. A picture of the assembled diagnostic single cell is shown in Figure 1.8.

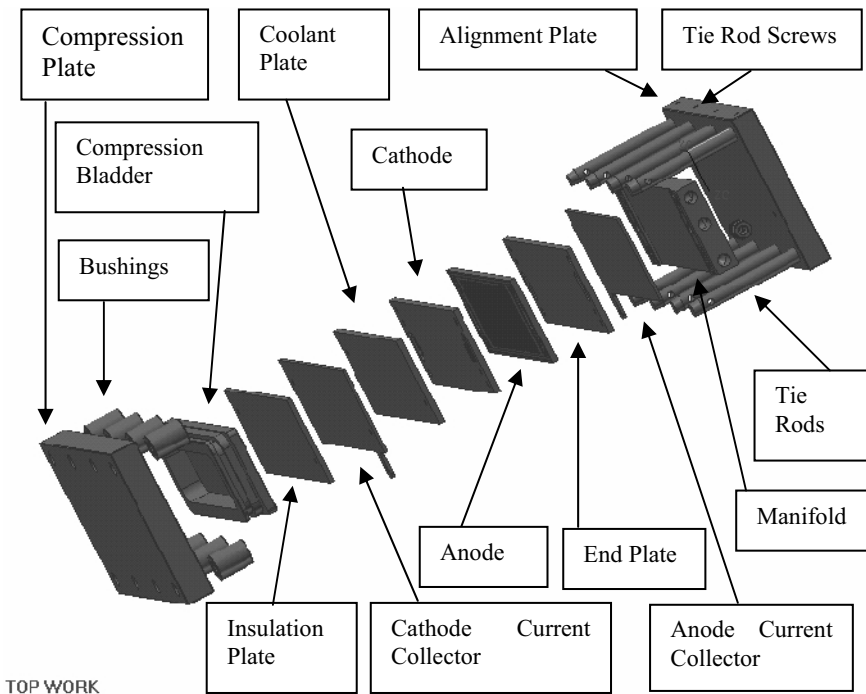


Figure 1.7. Assembly diagram of a diagnostic modeling PEM fuel cell with an active area of 192 cm², designed by NRC-IFCI [6]



Figure 1.8. Assembled diagnostic modeling cell [6]

Stack

Single cells produce less than 1 V of electricity, which is far from enough to power a vehicle. In order to produce a useful voltage, multiple cells must be assembled into a fuel cell stack. This can be achieved in a parallel and/or a series mode to supply feed gas to the stacks. In a parallel gas supply fuel cell stack, all cells are fed in parallel from a common hydrogen/air inlet. In the serial configuration the gas from the outlet of the first cell is fed to the inlet of the second cell and so on until the last cell, which helps prevent non-uniform gas distribution. To avoid a large pressure drop this arrangement can be used only for stacks with a small number of fuel cells [7].

A discussion of the distribution of the reactant gases must address the flow field design. The essential requirement for flow field design is uniform distribution of the reactant gases over the respective active electrode surface. A non-uniform distribution will result in a non-uniform current density distribution leading to lower catalyst utilization, lower energy efficiency, and, last but not least, a reduced cell life. Usually, flow fields are designed around their maximum power operating point with the goals of maximizing performance and minimizing pressure drop between the inlet and outlet of the flow field. Nevertheless, when designing a flow field, several considerations must be taken into account, including flow rate, water management, thermal management, and pressure drop.

For a typical planar PEMFC design, feeding channels are often designed with one of three basic flow field structures: serpentine, parallel, or interdigitated [8]. Due to the length of the channels, serpentine flow fields have large pressure losses between the inlet and the outlet. The straight parallel design exhibits lower pressure differences; however, inhomogeneous reactant gas distribution can easily

occur. The interdigitated flow field, which consists of dead-ended inlet and outlet channels, forces the reactant gas to flow through the electrode in order to exit, and helps solving the cathode-flooding problem.

In most commercial fuel cell stacks, the separator plates are designed to be bipolar, with one side of the plate being the anode of one cell and the other side being the cathode of the adjacent cell. The series electrical connection between cells is made through the electrically conducting separator plate. The potential power generated by a series-connected fuel cell stack depends on the number and size of the individual fuel cells that comprise the stack and the surface area of the PEM.

A typical PEM fuel cell stack is shown in Figure 1.9. Individual cells are electrically connected with interconnects. The interconnect becomes a separator plate, which provides an electrical series connection between adjacent cells and a gas barrier that separates the fuel and oxidant of adjacent cells.

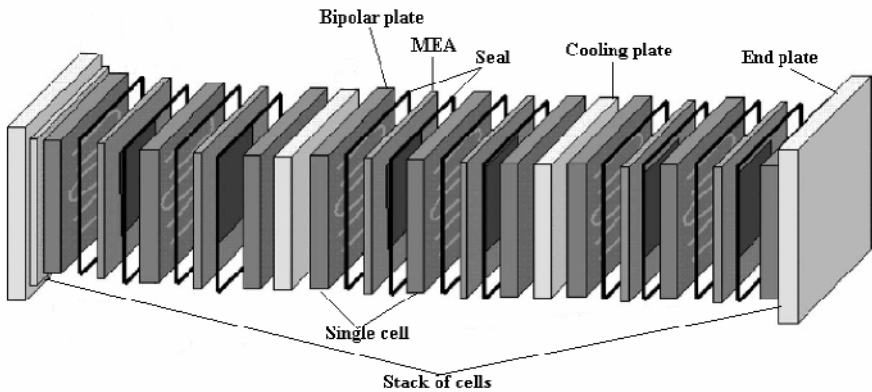


Figure 1.9. PEM fuel cell stack. (Reprinted and modified from [9]. Journal of Power Sources, 114(1), Mehta Viral and Cooper Joyce Smith, Review and analysis of PEM fuel cell design and manufacturing, 70–79, ©2003, with permission from Elsevier.)

System

In addition to the stack, practical fuel cells such as those in fuel cell vehicles (FCVs) require several other sub-systems and components to work as a system. Generally speaking, most fuel cell systems contain the following:

- Hydrogen reformer or hydrogen purification: When a fuel other than hydrogen are used, it must be reformed to form a hydrogen-rich anode feed mixture. Even if hydrogen gas is used, it can contain impurities, which can cause deactivation of the catalysts. The impurities are removed through a process of purification.
- Air supply: This includes air compressors or blowers as well as air filters.
- Water management: Inlet gases normally must be humidified, and water is a reaction product.
- Thermal management: All fuel cell systems require careful management of the fuel cell stack temperature [10].

The specific arrangement of the fuel cell systems varies, depending on the fuel cell type, the fuel choice, and the application. An example of a fuel cell system with direct hydrogen gas feeding is depicted in Figure 1.10(a).

Methanol and some other liquid fuels can be fed to a PEM fuel cell directly without being reformed, thus forming a direct methanol fuel cell (DMFC), direct ethanol fuel cell (DEFC), direct formic acid fuel cell (DFAFC), and so on.

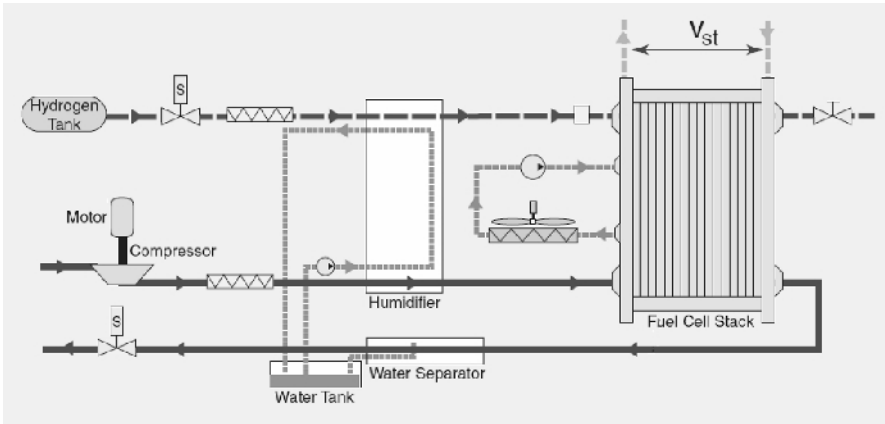


Figure 1.10(a). Block diagram of a PEM fuel cell system [11]. (Pukrushpan JT, Stefanopoulou AG, Peng H. IEEE Control Systems Magazine, Control of fuel cell breathing. ©2004 IEEE. Reprinted with permission.)

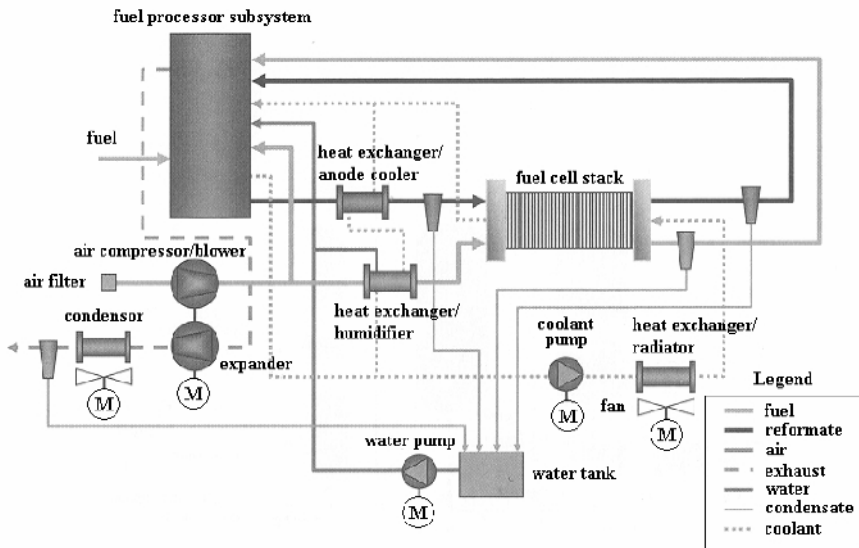


Figure 1.10(b). A complete fuel cell system integrated with a fuel processor [1]. (Reprinted from Barbir F. PEM fuel cells: theory and practice. New York: Elsevier Academic Press, ©2005, with permission from Elsevier.)

Typical systems utilize on-board reformation, processing the gasoline, methanol, or other carbon-based fuel into hydrogen-rich gas. A complete fuel cell system integrated with a fuel processor is shown in Figure 1.10(b). The system contains the four sub-systems explained above. Currently, complete systems such as this are available in the market. The most well-known manufacturers of PEM systems include Ballard Power Systems, UTC Power (also known as UTC Fuel Cells), PEMEAS USA, E-TEK Inc., DuPont, 3M, Johnson Matthey, WL Gore, Hydrogenics, and Plug Power [3].

1.1.2. Main Cell Components and Materials

1.1.2.1 Membrane

The main function of the membrane in PEM fuel cells is to transport protons from the anode to the cathode; membrane polymers have sulfonic groups, which facilitate the transport of protons. The other functions include keeping the fuel and oxidant separated, which prevents mixing of the two gases and withstanding harsh conditions, including active catalysts, high temperatures or temperature fluctuations, strong oxidants, and reactive radicals. Thus, the ideal polymer must have excellent proton conductivity, chemical and thermal stability, strength, flexibility, low gas permeability, low water drag, low cost, and good availability [12].

Different types of membranes have been tested for use in PEM fuel cells. The membranes are usually polymers modified to include ions, such as sulfonic groups. These hydrophilic ionic moieties are the key for allowing proton transport across the membrane. The favored polymer structure has changed to improve membrane lifetime and slow down membrane degradation [13].

The very early membranes, fabricated by Grubb and Niedrach of GE, were phenol-formaldehyde sulfonic acids produced by the condensation of phenolsulfonic acid and formaldehyde. Unfortunately, they hydrolyzed easily and were extremely weak. These were followed by membranes with a partially sulfonated polystyrene backbone. Their performance was also unsatisfactory, achieving a lifetime of only 200 hours at 60 °C. The first membranes to have sufficient physical strength were “D” membranes, manufactured by American Machine Foundry. They were fabricated by grafting styrene-divinylbenzene into a fluorocarbon matrix, followed by sulfonation. “D” membranes achieved life spans of 500 hours at 60 °C and were utilized in the fuel cells as auxiliary power sources for seven Gemini space missions [14].

Degradation of the “D” membranes was linked to the reactivity of the alpha C-H bond in the polymer. A series of membranes that did not contain this bond were then synthesized. α,β,β -trifluorostyrene sulfonic acid was determined to have chemical and thermal stability, but poor physical properties (Figure 1.11(a) [15]). This was somewhat improved by using a triethyl phosphate plasticizer to combine polyvinylidene fluoride with the trifluorostyrene sulfonic acid polymer, reaching a lifetime of up to 5000 hours at 80 °C. This lifetime was doubled by a fluorocarbon matrix grafted with trifluorostyrene, and then further improved by a membrane composed of trifluorostyrene and substituted trifluorostyrene copolymers [16, 17]. The latter membrane (Figure 1.11(b)), developed by Ballard Power Systems,

achieved a performance time of more than 15,000 hours (for the BAM3G series) [14, 18].

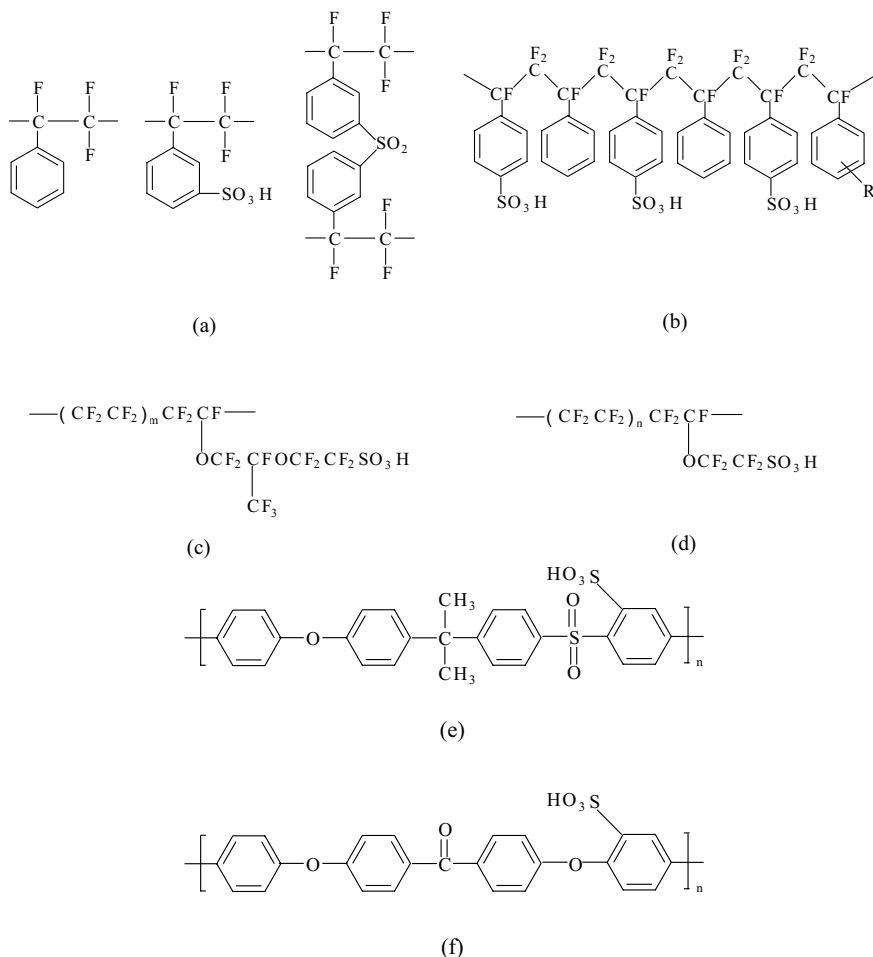


Figure 1.11. Types of PEMs: (a) Monomer units of α,β,β -trifluorostyrene sulfonic acid (b) BAM3G (c) Nafion (d) Dow membrane (e) polysulfone (f) polyetherketone [24]. (Reprinted from International Journal of Hydrogen Energy, 31, Colliera A, Wang H, Yuan XZ, Zhang J, Wilkinson DP. Degradation of polymer electrolyte membranes, 1838–54, ©2006 with permission from Elsevier.)

One of the most widely used membranes today is Nafion, a polymer created by the DuPont company. Nafion (Figure 1.11(c) [13]) has an aliphatic perfluorinated backbone with ether-linked side chains ending in sulfonate cation exchange sites [14, 19]. It is a copolymer of tetrafluoroethylene and sulfonyl fluoride vinyl ether [20] and has a semi-crystalline structure [21]. This structure, which resembles Teflon, gives Nafion long-term stability in oxidative or reductive conditions [12]. In the dry state it has reverse micelle morphology, in which the ionic clusters are

dispersed in a continuous tetrafluoroethylene phase. When the membrane absorbs water, the ionic domains swell and form proton-conducting channels above a critical water content. The conductivity increases with the water content up to a point. As the water content increases further, the concentration of protons is diminished and the conductivity is decreased. Nafion 120 was reported to reach 60,000 hours of operation (43 °C–82 °C) [14].

The Dow Chemical Company manufactured a similar membrane (Figure 1.12(d) [13]) with shorter side chains, which was shown to attain a power density more than double that of Nafion. However Nafion remains the most popular membrane due to lower cost and ease of fabrication [22]. Nafion is still quite expensive, and the industry is striving to find a more affordable substitute to allow commercialization.

Several other types of polymers, such as polyetherketones, polyimide, and polyethersulfone (Figures 1.11(e) and 1.11(f)) are also being studied [18, 23].

Generally, it is the lifetime of the PEM that determines the life of the PEMFC. Thinner membranes, although they increase performance efficiency and proton conductivity, have lower physical strength and higher gas permeability, allowing more gas crossover, which accelerates degradation. According to H₂/air PEMFC testing, Nafion 112 has reached a maximum lifetime of just over 10,000 hours [14]. The technology for solid polymeric electrolytic membranes calls for the thinnest film that is electrochemically stable. At present, polymeric solid state fuel cell membranes, thinner than 50 microns, seldom work mechanically during fuel cell operation. When approaching the thin film limits, interfacial effects become significant to structure dynamics and consequently, the stability of the membranes [25].

1.1.2.2 Electrodes

Platinum has been considered to be the best catalyst for both the anode and the cathode though there is a large difference between the ORR and the hydrogen oxidation reaction (HOR) using the same catalyst. A great deal of effort has been made by many researchers toward developing appropriate catalyst materials, especially for the ORR, and platinum is so far still the best option. Therefore, in many PEMFCs, the anode and the cathodes use an identical catalyst: platinum.

Usually, the platinum catalyst is formed into small particles on a surface of somewhat larger particles that act as a supporter, known as carbon powder. A widely used carbon-based powder is Vulcan XC72[®] (by Cobalt). This way the platinum is highly divided and spread out, so that a very high proportion of the surface area will be in contact with the reactant, resulting in a great reduction of the catalyst loading with an increase in power. In the early days of PEM fuel cell development, the catalyst was used at the rate of 28 mg/cm² of platinum. In recent years the usage has been reduced to around 0.2 mg/cm² with an increase in power. The basic raw-material cost of the platinum in a 1 kW PEMFC at such loadings would be about \$10—a small portion of the total cost [26].

Basically, there are two methods to form the MEA of a PEM fuel cell. One alternative is using appropriate techniques to add the carbon-supported catalyst to a porous and conductive material, such as carbon cloth or carbon paper, called a gas diffusion layer (GDL). Normally, polytetrafluoroethylene (PTFE) and Nafion

solution are added. PTFE, which is hydrophobic, can expel the product water to the surface where it can evaporate. Nafion can help attach the catalyst layer to the membrane, and it also helps increase the ionic conductivity of the catalyst layer. Then the catalyst-surfaced GDL is hot-pressed together with the pre-treated membrane, which has catalyst on each side. This fairly standard procedure for fabricating an MEA is described in many papers. For example, Lee et al. [27], cleaned the electrolyte membrane by immersing it first in boiling 3% hydrogen peroxide in water for 1 hour, and then in boiling sulfuric acid for the same amount of time, to ensure as full protonation of the sulfonate group as possible. The membrane was rinsed in boiling deionised water for 1 hour to remove any remaining acid. The electrodes were then put onto the electrolyte membrane and the assembly was hot pressed at 140 °C at high pressure for 3 minutes to complete the process.

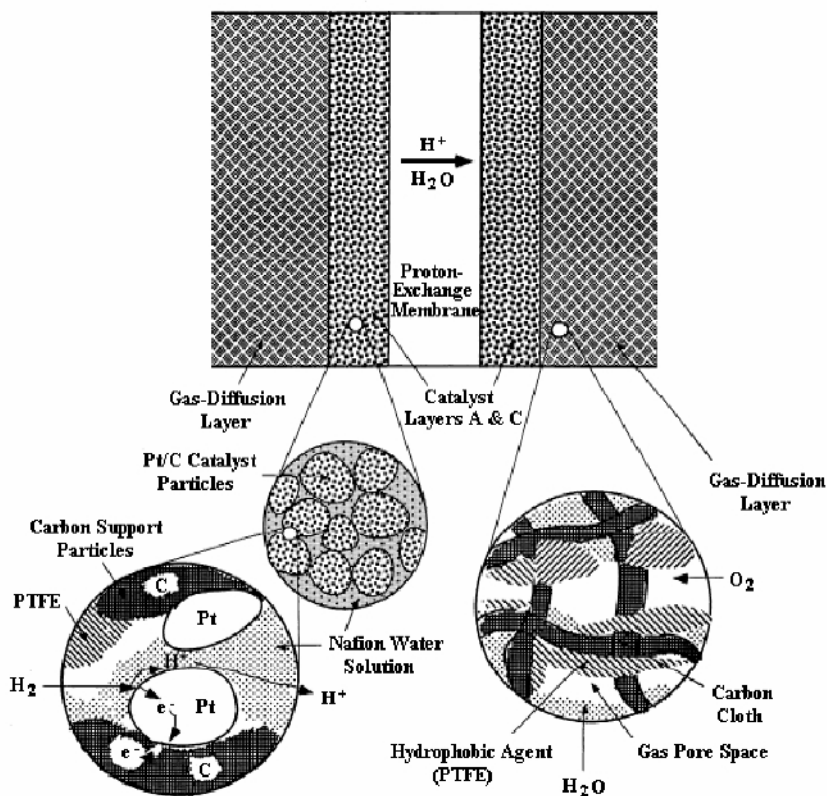


Figure 1.12. Diagram of a typical MEA structure [31]. (Reprinted from *Catalysis Today*, 67(1–3), Thampan Tony, Malhotra Sanjiv, Zhang Jingxin and Datta Ravindra, PEM fuel cell as a membrane reactor, 15–32, ©2001, with permission from Elsevier.)

Another method is to build the electrode directly onto the membrane. In this method, the catalyst mixed with hydrophobic PTFE is directly manufactured onto

the membrane using various techniques such as rolling methods [28], spraying [29], or an adapted printing process [30]. However, the literature seldom gives details about the method used. Once the catalyst is fixed to the membrane, a GDL is then applied when assembling the cell.

The MEAs manufactured by both of the above methods have similar sandwich-like structures. As depicted in Figure 1.12, the outer layers of the sandwich are GDLs. The membrane is in the middle, with catalysts between the GDL and membrane. The anode, the negative side of the fuel cell, conducts the electrons freed from the hydrogen oxidation so that they can be used in an external circuit. The cathode, the positive side of the fuel cell, conducts the electrons back from the external circuit to the catalyst, where they can recombine with the hydrogen ions and oxygen to form water. The PEM—a specially treated material—conducts only positively charged ions and blocks the electrons, which is crucial to PEM fuel cell technology.

The thickness of the membrane in an MEA varies with the type of membrane. The thickness of the catalyst layer depends upon how much platinum is used in each electrode. For catalyst layers containing about 0.15 mg Pt/cm^2 , the thickness of the catalyst layer is close to $10 \text{ }\mu\text{m}$. The thickness of an MEA depends on the thickness of the membrane, catalysts, and GDL. The MEA, with a total thickness of about $200 \text{ }\mu\text{m}$, can generate more than 0.5 A/cm^2 at a voltage of 0.7 V when encased in well-chosen key materials—membrane, backing layers, bipolar plates, catalysts, and other components, such as flow fields, and current collectors [32].

1.1.2.3 Gas Diffusion Layer

GDLs are critical components in PEMFCs. The GDLs (or the backing layers), together with the flow fields and current collectors, are designed to achieve high performance from the operation of the PEM fuel cell. But the GDLs may or may not be an integral part of the MEA [26].

The main function of the GDL is to diffuse the gas. The porous nature of the backing material facilitates the effective diffusion of each reactant gas to the catalyst on the MEA. The GDL is also an electrical connection between the carbon-supported catalyst and the bipolar plate or other current collectors. In addition, the GDL also helps in managing water in the fuel cell as it carries the product water away from the electrolyte surface [32].

The GDL is usually made of a carbon-based porous substrate, such as carbon paper or carbon cloth, with a thickness of about 0.2 to 0.5 mm and a dual-layer structure. A schematic of the GDL between the flow field and the catalyst layer is presented in Figure 1.13. The first layer of the GDL, in contact with the flow field and the inlet gas in the flow channels, is a macro-porous carbon substrate, serving as a current collector, a physical support for the catalyst layer, and an elastic component of the MEA. The elastic component is necessary for the fuel cell to handle the compression needed to establish an intimate contact. The second layer of the GDL, in contact with the catalyst layer, is a thinner microporous layer consisting of carbon black powder and some hydrophobic agent, which provides proper surface pore size and hydrophobicity to avoid flooding and to enhance intimate electronic contact at its interface with the catalyst layer [33].

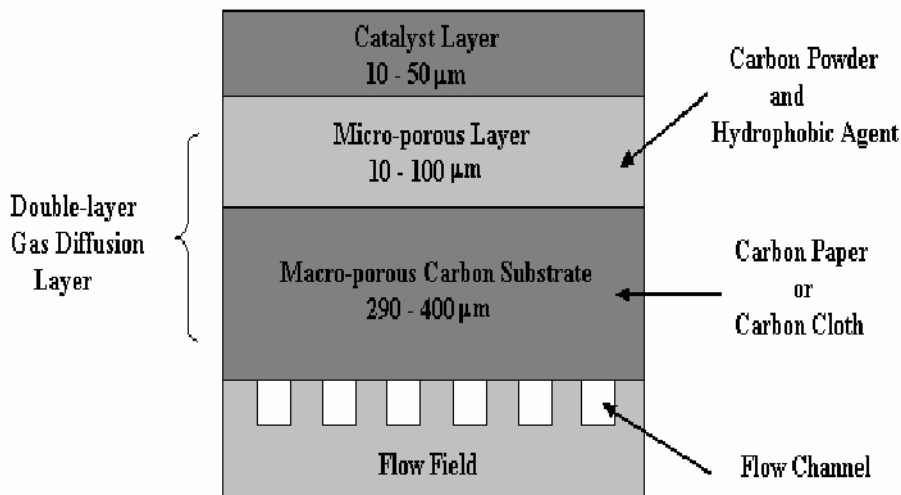


Figure 1.13. Schematic of a double-layer GDL [33]. (Reproduced by permission of ECS—The Electrochemical Society, from Williams MV, Begg E, Bonville L, Kunz HR, Fenton JM. Characterization of gas diffusion layers for PEMFC.)

An ideal GDL is required to effectively transport the gas reactants to the catalyst layers, have low electronic resistance, have a surface that enhances good electronic contact, and have proper hydrophobicity for each application. In particular, for the highest power output when the fuel cell is operated at a relatively high current density, a higher flux of gas feed is needed, which requires the ideal GDL to effectively transport reactant gases to the catalyst surfaces at a high rate [33].

1.1.2.4 Bipolar Plates

Among the components of the fuel cell stack, the bipolar plate is considered to be one of the most costly and problematic. In addition to meeting cost constraints, bipolar plates must possess a host of other properties. The search for suitable, low-cost bipolar plate materials is a key concern in PEMFC stack development [34].

The bipolar plate is a multi-functional component. Its primary function is to supply reactant gases to the gas diffusion electrodes (GDEs) via flow channels. The effectiveness of the reactant transport depends partially on the art of the flow-field design [35], so an alternative name for the bipolar plate is the flow-field plate. Bipolar plates must provide electrical connections between the individual cells. They have to remove the water produced at the cathode effectively [36]. Bipolar plates must also be relatively impermeable to gases, sufficiently strong to withstand stack assembly, and easily mass-produced. For transport applications, low weight and low volume are essential [37]. As bipolar plates operate in constant contact with the acidic water ($\text{pH} \approx 5$) that is generated under the operating conditions of the stack, high chemical stability and corrosion resistance are required. Not only can oxides formed during corrosion migrate and poison the catalyst but they can also increase the electrical resistivity of the plates, and

therefore result in reduced fuel cell performance. In addition, the bipolar plate material must be able to resist a temperature of 80°C or more, high humidity, and an electrical potential [38]. To summarize, the PEMFC bipolar plate technical design criteria or major constraints are as follows:

1. Low cost (< \$2/plate)
2. Ease of gas flow
3. High electric conductivity (> 100 Scm⁻¹)
4. Low impermeability to gases
5. High manufacturability
6. Reasonable strength
7. Low weight
8. Low volume
9. High chemical stability and corrosion resistance (< 16 μAcm⁻²)
10. Low thermal resistance

Potential bipolar plate materials should meet all of these requirements and, in the long run, should be inexpensive and readily available for the purpose of mass production [39].

Generally speaking, graphite is an excellent material for fuel cell bipolar plates, but both the material cost and the processing cost are very high for large-scale production. Although graphite plates are not considered to be the most effective material for PEM fuel cell applications, they are preferred for space applications due to their superior corrosion resistance without coating when compared to metal plates. Now more attention is being paid to composites and metals. It has been concluded that the most promising for fuel cell commercialization are the graphite polymer composites and metallic materials with coatings. Carbon polymer composites and sheet metal are potentially low-cost materials and are especially suitable for mass production because flow fields can be molded directly into carbon polymer composites, and thin sheet metal can be stamped to plates in an established mass production process. Nevertheless, there is still a great deal of work needed to obtain satisfactory bipolar plate materials. Not only should an optimal bipolar plate meet the property requirements above, but its fabrication process should also be easy fabrication and inexpensive. The art of the flow-field design of bipolar plates is another important feature for the performance of the fuel cells. The fate of potential materials will ultimately determined by all these factors [34].

1.1.3 PEM Fuel Cell Operation

1.1.3.1 Operation Conditions

The principle of how a PEM fuel cell generates electricity is straightforward. However, the cell power output depends on material properties, cell design and structure, and operation conditions, such as the gas flow, pressure regulation, heat, and water management. High performance of a PEM fuel cell requires maintaining optimal temperature, membrane hydration, and partial pressure of the reactants

across the membrane to avoid any degradation of performance. These critical operation parameters must be controlled over a wide range of current [11].

Operating Pressure

A PEM fuel cell can be operated at ambient pressure or at a higher pressure. A fuel cell usually obtains better performance when the pressure is increased. But note that to increase the operating pressure, extra compression power is needed. From the system point of view, the net gain of pressurized operation is questionable when compression power is taken into account. In addition, the issue of pressurization is related to the issue of water management [1].

Very often, the reactant gas is fed from a pressurized tank to the fuel cell at the inlet. The pressure, known as the backpressure, is controlled by a pressure regulator installed at the outlet. This backpressure regulator keeps the desired pressure at the fuel cell outlet, while the inlet pressure is sometimes not even recorded. However, the inlet pressure, which is always higher than the outlet pressure as there is a pressure drop between the inlet and outlet along the flow channels, is sometimes the pressure that matters. For example, there are two types of air supply systems for the cathode inlet [1].

Air blowing: In an air-blowing system, air is supplied to the cathode by a mechanical device, a compressor or a blower. The compressor or the blower must be able to deliver the air at the required flow rate and desired pressure. The backpressure regulator may still be installed to control the backpressure either at ambient pressure or at a higher pressure.

Air breathing: Conventional air-blowing PEM fuel cell systems are limited for portable applications because they need power-consuming auxiliary devices, such as pumps, valves, fans, and humidifiers. Thus, air-breathing PEM fuel cells have been developed to overcome these limitations. In an air-breathing system, air is supplied to the cathode by diffusion and natural convection from the surroundings without humidification, so that the entire system is simplified. Nevertheless, there are obstacles for the air-breathing system despite the advantages of its system design. For example, the cell performance of an air-breathing cell is not as good as that of an air-blowing cell due to the poor transportation of air to the cathode, and there is no convective flow for the cathode to help manage the water balance in the system, which is crucial to the PEM fuel cell system [40].

Operating Temperature

The cell temperature is another operating parameter that plays an important role in the cell operation. Generally speaking, a higher operating temperature results in higher cell potential or performance. However, for each fuel cell design there is an optimal operating temperature. Better performance will be obtained when the cell is operated at the optimal temperature, but a PEM fuel cell does not have to be heated up to this temperature in order to become operational. From the system point of view, the operating temperature of a practical fuel cell should be selected, as with the operating pressure, by taking into account not only the cell performance, but also the system requirements, such as the parasitic power requirements of the heat management sub-system.

The fuel cell reaction is exothermic; therefore it generates heat as a by-product. To maintain the desired temperature, heat must be removed from the system. Some heat dissipates from the outer surface of the fuel cell and the rest must be taken away with a cooling system. The cooling medium may be air, water, or a special coolant. The inner design of the fuel cell must allow the coolant to pass through, for example, a coolant plate or coolant channel on the back of the anode or cathode plate. Small fuel cells need a heater to reach the operating temperature because so much heat is being taken away from the outer surface [1]. The heat balance within a fuel cell can be written as

$$Q_{gen} + Q_{react,in} = Q_{dis} + Q_{react,out} + Q_{cool} \quad (1.1)$$

where Q_{gen} , $Q_{react,in}$, Q_{dis} , $Q_{react,out}$, and Q_{cool} refer to the heat generated in the fuel cell, the heat brought into the cell with reactant gases, the heat dissipation from the cell surface to the surroundings, the heat taken away by the reactant gases leaving the cell, and the heat carried away by the coolant, respectively.

In addition, the temperature inside a fuel cell may not be uniform. It may vary from the inlet to the outlet, from the inside to the outside, or from the cathode to the anode. Very often the measured fuel cell temperature could be the surface temperature, the temperature of the air leaving the cell, or the temperature of the coolant leaving the cell.

Reactant Flow Rate

The reactant flow rate at the inlet of a fuel cell must be equal to or higher than the consuming rate of the reactant in the cell. A reactant-starved condition is detrimental to the fuel cell performance, since starvation can lead to cell reversal, which is often recognized by a negative cell potential. In this case, a hydrogen-starved anode is forced to oxidize water to generate oxygen and an oxygen-starved cathode is forced to reduce protons to hydrogen. Then, the presence of oxygen in the hydrogen electrode and hydrogen in the oxygen electrode can result in local hot spots on the membrane, leading to membrane degradation and failure of the fuel cell [7]. The solution is to ensure adequate gas flow to all the cells by using high stoichiometric gas flow rates (λ_{air} and λ_{H_2}) and proper flow-field designs to prevent one cell or a group of cells from receiving most of the gas flow while other cells become reactant starved during operation.

The usage of the cathode and anode reactants can be calculated based on Faraday's law. For each mole of oxygen, four electrons are transferred; therefore,

$$O_2 \text{ usage} = \frac{I}{4F} \text{ mol} / s \quad (1.2)$$

$$\text{Air usage} = \frac{I}{4F} \times \frac{1}{0.21} \text{ mol} / s \quad (1.3)$$

For each mole of hydrogen, two electrons are transferred,

$$\text{H}_2 \text{ usage} = \frac{I}{2F} \text{ mol} / \text{s} \quad (1.4)$$

For a stack with n cells, the reactant usages become

$$\text{Air usage} = \frac{I}{4F} \times \frac{n}{0.21} \text{ mol} / \text{s} \quad (1.5)$$

$$\text{H}_2 \text{ usage} = \frac{In}{2F} \text{ mol} / \text{s} \quad (1.6)$$

Adding the cathode and anode excess gas ratio, λ_{air} and λ_{H_2} , the two equations can be written as

$$\text{Air usage} = \frac{I}{4F} \times \frac{n}{0.21} \times \lambda_{Air} \text{ mol} / \text{s} \quad (1.7)$$

$$\text{H}_2 \text{ usage} = \frac{In}{2F} \times \lambda_{H_2} \text{ mol} / \text{s} \quad (1.8)$$

As most fuel cell test stations are controlled by regulating the flow rate at standard liter per minute (slpm), the above two equations are then transferred with a unit of slpm by using the ideal gas law. The results are as follows:

$$\text{Air usage} \approx 0.0166nI\lambda_{air} \text{ slpm} \quad (1.9)$$

$$\text{H}_2 \text{ usage} \approx 0.0070nI\lambda_{H_2} \text{ slpm} \quad (1.10)$$

Reactant consumption using other units is listed in Table 1.1.

Table 1.1. Reactant consumption (under the condition of per Ampere, per cell, 25 °C, and ambient atmosphere)

Unit	Oxygen consumption	Air consumption	Hydrogen consumption	Water generation
mols^{-1}	2.59×10^{-6}	1.23×10^{-5}	5.18×10^{-6}	5.18×10^{-6}
gs^{-1}	8.29×10^{-5}	3.94×10^{-4}	1.04×10^{-5}	9.33×10^{-5}
cm^3s^{-1}	0.063	0.302	0.126	9.33×10^{-5}
slpm	0.0038	0.0181	0.0076	N/A
sm^3h^{-1}	2.28×10^{-4}	1.08×10^{-3}	4.56×10^{-4}	N/A

Reactant Humidity

Water balance and management are an important concern in PEM fuel cell system control. Dynamic water balance and management have become one of the major technical challenges for PEM fuel cell design and operation because they have a direct influence on the performance and lifetime of PEM fuel cell systems.

Generally speaking, reactant gases with inlet relative humidity (RH) equal to or less than 100% are needed during the cell operation. The supply of reactant humidity is necessary and important because the membrane (e.g., Nafion) requires full hydration in order to maintain good performance and lifetime. It is widely recognized that membrane hydration can be achieved by supplying fully humidified reactant gas streams to both the anode and the cathode.

The conductivity of the membrane in a PEMFC is directly related to its water content, which depends on (1) the water carried by the humidified reactant gases; (2) the water generated at the cathode as a result of electrochemical reaction; (3) the electroosmotic drag—that is, the water carried by the protons from the anode to the cathode; and (4) the water back diffusion from the cathode to the anode. Therefore, it is obvious that water management is a complex issue.

Water management is very delicate for fuel cell users to control. Too much or too little water can degrade both the performance and therefore the lifetime of PEM fuel cells. If the membrane is too dry, it results in a direct decrease of membrane conductivity. If water is not removed adequately from the cell, especially at the cathode, liquid water flooding occurs, which leads to PEM fuel cell performance that is unpredictable, unreliable, and unrepeatable under identical operating conditions. Therefore, maintaining a perfect water balance during dynamic operation processes is crucial to fuel cell performance and lifetime [41].

It should be pointed out that in addition to the reactant humidity control, the flow channel layout, channel dimensions, and specifications of other cell components also influence water removal and the performance of the cell, which indicates that proper design of the flow fields and other components may help achieve better water balance and management in PEM fuel cells.

1.1.3.2 Failure Modes and Accelerated Testing [42]

Fuel cell commercialization has been delayed again and again due to technical barriers such as on-board storage, infrastructure for the hydrogen fuel and the fuel cell system and its durability. Durability, which is always defined as the maximum lifetime of a fuel cell system with no more than 10% loss in efficiency at the end of life, is one of the most stringent requirements for PEM fuel cells to be accepted as a viable product. The requirements for fuel cell lifetime vary significantly for different products. The fuel cell industry has set standards including: a lifetime durability of more than 40,000 hours and 8,000 hours of uninterrupted service at over 80% power for stationary applications. For buses and cars, more than 20,000 and 6,000 operating hours are required, respectively [43, 44].

Various studies have focused on the degradation mechanisms of either the fuel cell system or its components under steady or accelerated operational conditions. The major failure modes of different components of PEM fuel cells are listed in Table 1.2.

Table 1.2. Major failure modes of different components in PEM fuel cells

Component	Failure modes	Causes
Membrane	Mechanical degradation	Mechanical stress due to non-uniform press pressure; inadequate humidification or penetration of the catalyst particles; fluoride loss
	Thermal degradation	Thermal stress; drying of membrane
	Chemical/electrochemical degradation	Trace metal contamination (foreign cations, such as Ca^{2+} , Fe^{3+} , Cu^{2+} , Na^+ , K^+ , and Mg^{2+}); radical attack (e.g., peroxy and hydroperoxy)
Catalyst/Catalyst layer	Loss of activation;	Sintering or dealloying of electrocatalyst;
	Conductivity loss;	Corrosion of electrocatalyst support;
	Decrease in mass transport rate of reactants;	Mechanical stress;
	Loss of reformat tolerance;	Contamination;
	Decrease in control of water management	Change in hydrophobicity of materials due to Nafion or PTFE dissolution
GDL	Decrease in mass transport;	Degradation of backing material;
	Conductivity loss;	Mechanical stress (e.g., freeze/thaw cycle);
	Decrease in control of water management	Corrosion; Change in hydrophobicity of materials
Bipolar plates	Conductivity loss;	Corrosion; Oxidation;
	Fracture/deformation	Mechanical stress
Sealing gasket	Mechanical failure	Corrosion; mechanical stress

Traditional lifetime data analysis in engineering involves analyzing times-to-failure data obtained under normal operating conditions in order to quantify the life characteristics of the product, system, or component. For fuel cells, the times-to-failure data are always very difficult to obtain due to the prolonged test periods necessary and high costs. To reduce the experimental time, different strategies to accelerate PEM fuel cell and component degradation have been suggested. Generally accelerated test methods for PEM fuel cell lifetime analysis are summarized in Table 1.3.

Table 1.3. General accelerated test methods in PEM fuel cell lifetime analysis

Component	Methods
Fuel cell/stack	Open circuit voltage (OCV); dynamic load cycling; thermal cycling; reduced/variable humidity; fuel or oxidant contaminates; fuel or oxidant starvation
Membrane	OCV at reduced humidity for chemical stability; RH cycling for mechanical degradation
Catalyst/catalyst layer	Potential cycles; acid washing; elevated temperature; fuel or oxidant contaminates
GDL	Chemical oxidation in H ₂ O ₂ ; elevated potential; low humidity
Bipolar plates	Press-stress; acid treatment; potential cycling; temperature cycling
Sealing gasket	Temperature; acid treatment; deformation/press-stress

As a commercial product, the failure or reliability information of the fuel cell under typical operation conditions should be included. Basically, the durability of the fuel cell is not defined by a single lifetime test. Lifetimes at variable stresses are always statistical distributions. The detailed scheme of a typical statistical accelerated lifetime model is illustrated in Figure 1.14 [45, 46].

The process starts by collecting data from quantitative accelerated life tests followed by selecting an appropriate life distribution. Three different lifetime distributions, the 1-parameter exponential, the 2-parameter Weibull, and the lognormal distributions, are commonly used in accelerated life test analysis. Among them, the 1-parameter exponential is most commonly employed due to its simplicity. Then, the lifetime characteristic of the distribution at each stress level is estimated using the probability plotting method; this is followed by the selection of a life-stress relationship according to variables. The Arrhenius model is often utilized when the acceleration variable or stress is thermal, whereas the Eyring model and the inverse power law model are suitable for temperature-humidity stresses and non-thermal accelerated stresses, respectively. Finally, the real lifetime of the component or fuel cell under normal conditions can be predicted by extrapolation.

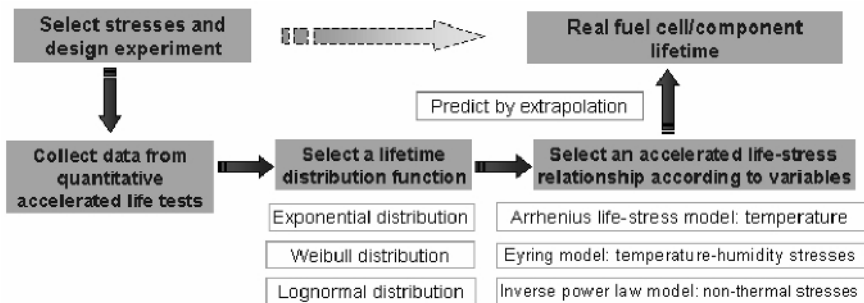


Figure 1.14. Principle of statistical accelerated lifetime testing model [42]

Based on the statistical model, Hicks [47] successfully predicted 3M MEA lifetimes under normal conditions (70 °C cell and 100% RH) from accelerated testing conditions. Weibull data distribution and the Arrhenius temperature model were employed. The statistical analysis and MEA lifetime prediction shown in Figure 1.15(a) were obtained. The load cycle with a near-open circuit voltage (OCV) setting was used in the accelerated tests, as shown in Figure 1.15(b).

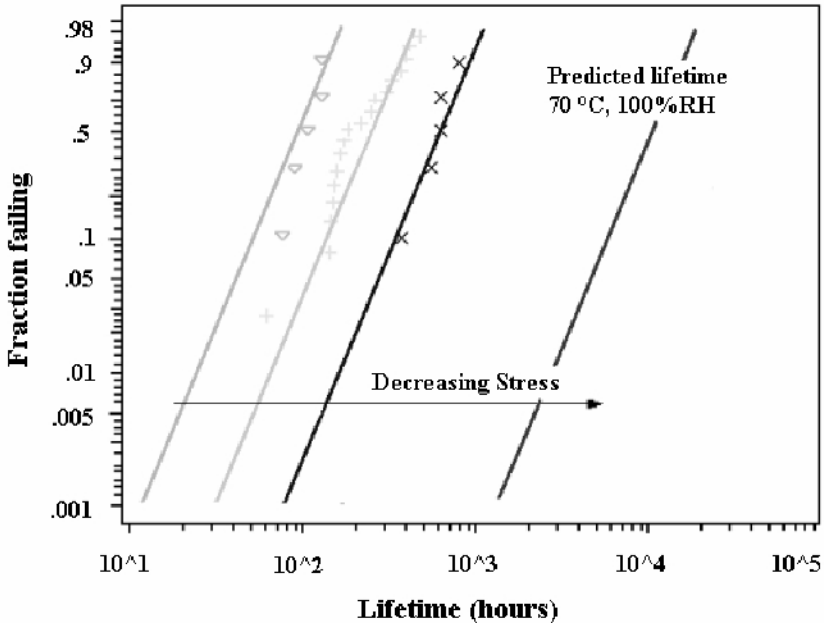


Figure 1.15(a). Statistical analysis of accelerated test data with MEA lifetime prediction done by 3M (Symbols—data points; lines—model fits) [47]. (Reprinted with permission from Hicks M. Membrane and catalyst durability under accelerated testing. In: Conference proceedings of fuel cell durability: stationary, automotive, portable. ©2005 Knowledge Press.)

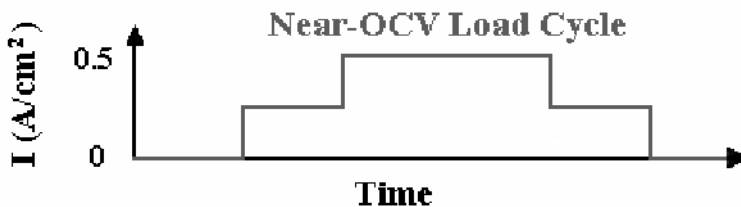


Figure 1.15(b). Near-OCV load cycle profile used in 3M accelerated testing [47]. (Reprinted with permission from Hicks M. Membrane and catalyst durability under accelerated testing. In: Conference proceedings of fuel cell durability: stationary, automotive, portable. ©2005 Knowledge Press.)

1.1.4 PEM Fuel Cell Applications

Since PEM fuel cells can generate power from a fraction of a watt to hundreds of kilowatts, they can be used in almost any application, from stationary power to vehicles of all sizes down to mobile phones. The application areas of PEM fuel cells with a variety of power levels are listed in Table 1.4.

Table 1.4. Application areas of PEM fuel cells with a variety of power level

Level of power	Applications
> 1 MW	Local distributed power station
100 kW–1 MW	Large transportation vehicles, such as naval ships, submarines, and buses; small portable power station; small stationary power station
10 kW–100 kW	Transportation vehicles such as cars and mid-size buses; backup power for mid-size communication station; small power station
1 kW–10 kW	Transportation vehicles such as motorcycles, utility vehicles, cars, yachts; various portable power devices used for field working, underwater platform; backup power; uninterruptible power, residential power system
100 W–1 kW	Simple riding devices such as bicycles, scooters, and wheelchairs; backpack power; power for exhibition or demo; UPS for small services, terminals, and computers
10 W–100 W	Portable power such as for emergency working power supply and military equipment; battery replacements; lighting; signal light power
< 10 W	Small portable power device; cell phone

Aside from military and space flight use, the less specialized fuel cell applications can be categorized into four main groups: transportation, stationary power, backup power, and portable power. PEM fuel cells are ideal for all these applications due to the availability of various power levels. Applications for transportation, such as automobiles, buses, utility vehicles, scooters, and bicycles have already been widely demonstrated. Applications for stationary power can be at the level of an individual home, a building, or a community, offering tremendous flexibility in power supply. Also, fuel cells are attractive as backup power generators compared with internal combustion engine generators (due to noise, fuel, reliability, and maintenance considerations) or batteries (due to weight, lifetime, and maintenance considerations). And small fuel cells as portable power generators offer several advantages over conventional batteries [1].

1.1.4.1 Transportation

The development of PEM fuel cell technology and the demonstration of its application to transportation vehicles have grown rapidly in the last 15 years. In 1993, Ballard demonstrated the first PEM fuel cell-powered bus. Then, following the announcement of the first fuel cell stack with a power density of 1 kW/l, a

Ballard phase 2 bus powered by a 200 kW unit was demonstrated. Later, demonstrations and testing of buses and cars powered by PEM fuel cells were like a rising wind and scudding clouds. Car producers have played an important role in these demonstrations. As air quality regulations grow steadily stricter, car manufacturers like Ford and Volkswagen are spending billions annually on the development of PEM fuel cell stacks for hybrid and electric cars [48].

Aside from buses and cars, there are many other types of transportation vehicles being demonstrated. Some transportation applications are shown in Figure 1.16.

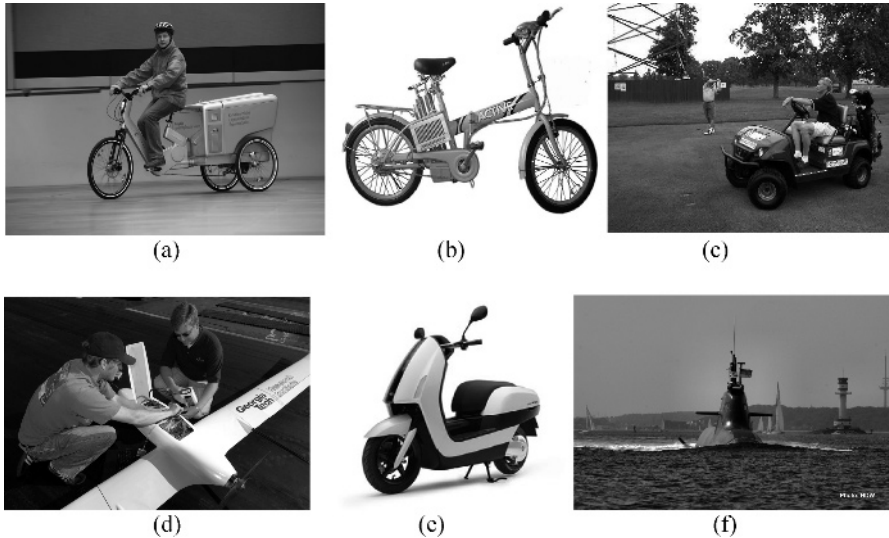


Figure 1.16. Some transportation applications of PEM fuel cells: (a) three-wheeled cargobike (image courtesy of Masterflex); (b) fuel cell bicycle (image courtesy of Pearl Hydrogen); (c) golf cart (image courtesy of Ohio State University); (d) PEMFC hydrogen aircraft (image courtesy of Georgia Institute of Technology); (e) Yamaha FC-AQEL scooter (image courtesy of Yamaha); (f) U212 submarine (image courtesy Howaldtswerke-Deutsche Werft GmbH).

An FCV can be powered directly using pure hydrogen as a fuel. Gaseous hydrogen is generally stored in high-pressure tanks so that it provides enough fuel to power the vehicle with a suitable driving range. Some hydrogen FCVs are powered by one electric motor. Others use a separate electric motor for each wheel, which together produce enough power to propel FCVs at speeds comparable to those of conventional vehicles.

Some FCVs employ a battery to store electricity produced from the fuel cell stack. The stored electricity can be used to help power the electric motor or other electrical devices. Some FCVs are designed to use a liquid fuel such as gasoline or methanol, which is stored in a conventional, non-pressurized tank. FCVs using these fuels need a reformer—a fuel processor that breaks the fuel down into hydrogen for the fuel cell, carbon dioxide, and water. Although this process

generates carbon dioxide, it produces much less than the amount generated by gasoline-powered vehicles [49].

1.1.4.2 Stationary Power

With the development of PEM fuel cell systems for transportation applications, the performance targets and cost objectives set by the car manufacturers define an attractive and competitive fuel cell system for stationary applications. Since the mid-1980s, PEM development has included stationary power applications, such as the GPU and Ballard 250 kW plant at Crane Naval Air Station in Indiana (1991); a 5 kW PEM unit powering a home in Albany, New York; and 6 PEM Alpha units tested by Bonneville Power Administration (2000).

Stationary power generation applications include not only large-scale utility plants but also smaller scale systems, such as those for distributed electricity and for heat generation in buildings and individual homes. The PEM fuel cell units for mobile applications in the range of 2 to 10 kW can be adapted to smaller stationary systems, which had been considered impractical with units in this capacity range. Battelle Memorial Institutes (USA) is identifying the most likely markets and the economic impacts of the stationary PEM fuel cells in the range of 1 to 250 kW in the United States by the year 2015. One likely scenario is that in 2015 PEM fuel cells will be limited to commercial and industrial customers in the range of 50 to 200kW with a market size of less than US\$ 5 billion a year [50].

Figure 1.17 presents some examples of stationary power generators; Figure 1.17(a) shows small-scale systems and Figures 1.17(b) to 1.17(e) show large-scale utility plants.

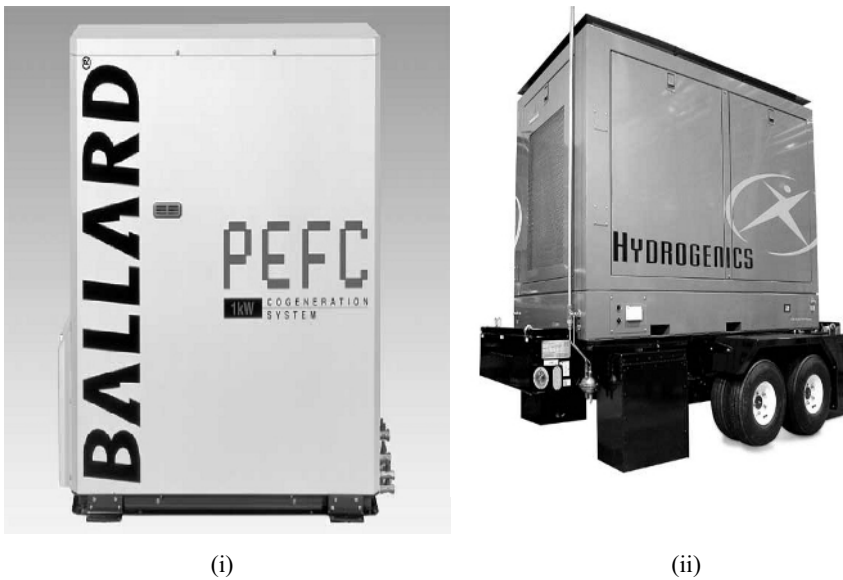


Figure 1.17(a). Small stationary fuel cells: (i) Ballard 1 kW PEM, (ii) Hydrogenics mobile 25 kW fuelcell. (Images courtesy of Ballard Power Systems (i) and Hydrogenics (ii).)

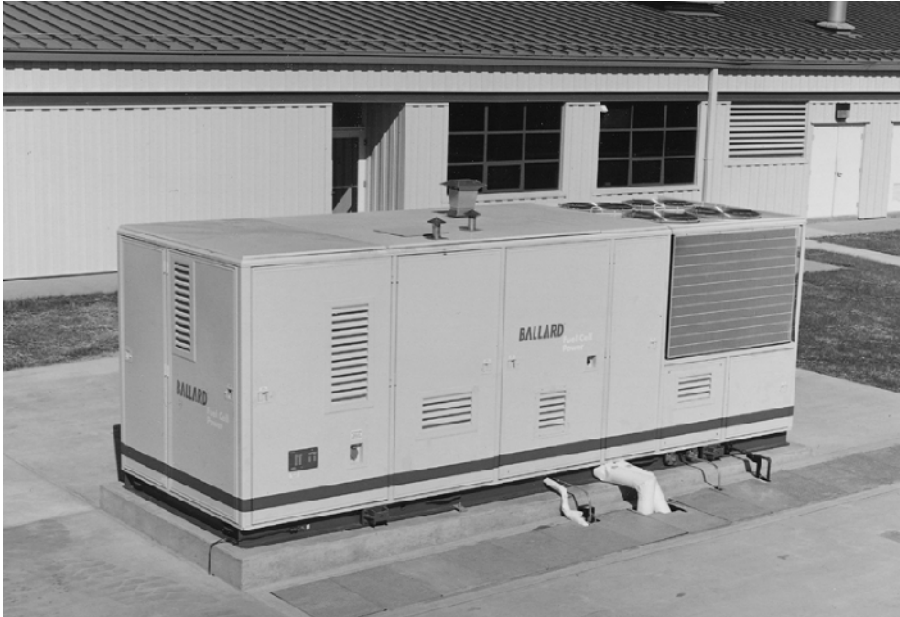


Figure 1.17(b). Ballard 250 kW power generator. (Image courtesy of Ballard Power Systems.)



Figure 1.17(c). UTC Fuel Cells PC25 6 × 200 kW. (Image courtesy of UTC Power Corporation.)



Figure 1.17(d). FuelCell Energy DFC3000™ 2 MW power generator. (Image courtesy of FuelCell Energy.)

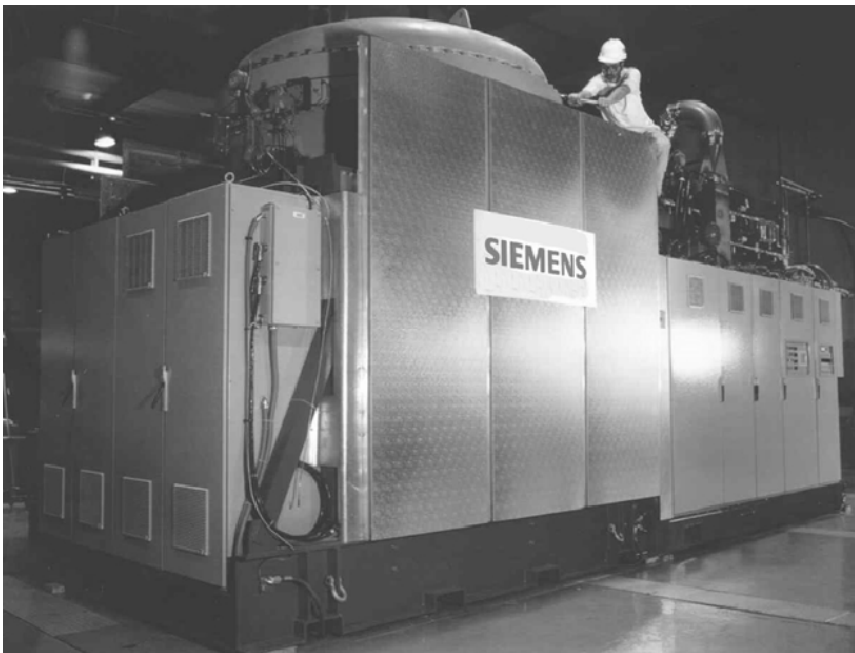


Figure 1.17(e). Siemens 220 kW power generator. (Image courtesy of Siemens.)

1.1.4.3 Backup Power

A backup power device provides an instantaneous, uninterruptible power source. The term UPS (uninterruptible power supply) is often used to refer to backup power. But it may also stand for systems that supply AC power, or systems that supply power for no more than 30 to 60 minutes. A more general definition of backup power covers all types of power outputs and all backup times. Typical applications for backup power include telecommunication systems, information technology and computer systems, manufacturing processes, security systems, utility substations, and railway applications.

Availability and reliability are two of the major concerns for backup power sources. The realization that the power generation system might be vulnerable to interruptions increased the need for backup power sources significantly. For many years, valve-regulated lead-acid battery systems and engine-generator sets have been the dominant sources for backup power. Ultra capacitors, flywheels, and new battery technologies later have joined the group of power providers. Most recently, backup power equipped with fuel cells has been employed by designing the systems to meet the requirements for backup power.

Normally, backup power will use hydrogen as fuel instead of reformat because one of the most important system requirements for backup power is to start instantly upon a power outage. In addition, backup power units are required to operate only intermittently, meaning that a short system lifetime is needed. The operational lifetime requirement for a fuel cell backup power is less than 2,000 hours. This duty cycle is more achievable with today's fuel cell technology than are those needed for FCVs and stationary power. Thus, backup power may become the first commercialized application of PEM fuel cells.

1.1.4.4 Small Portable Power

The convergence of voice, data, and multimedia is driving an endless demand for more power in cell phones, laptop computers, and other portable devices. PEMFCs or DMFCs may someday replace the batteries that power these portable electronic devices. PEM fuel cells have several advantages over batteries. The major drawbacks of batteries for these applications are limited capacity and slow recharging, whereas a fuel cell system can achieve higher power and energy capacity. In addition, battery performance deteriorates when the charge level drops, whereas fuel cells operate at a constant level as long as fuel is supplied.

During the past years, portable versions of fuel cells have emerged. The most promising miniature fuel cell is the DMFC, which is inexpensive and convenient, has a reasonable electrochemical performance, and does not require pressurized hydrogen gas.

In 2000, a portable fuel cell prototype produced 0.24 W and 0.9 V. A fuel cell stack made up of eight of these modules can power a cell phone. Toshiba developed a prototype fuel cell for a laptop, as shown in Figure 1.18, but as they describe the technology is in its infancy. The micro fuel cell on the left is able to provide 300 mW of continuous power with 99.5% pure methanol stored in a 10 mL tank. The picture on the right illustrates the refueling cartridge and refueling process.

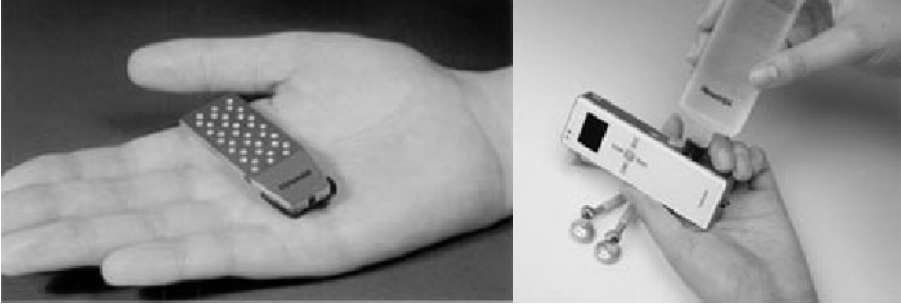


Figure 1.18. Toshiba fuel cell with refueling cartridge [51]. (Images courtesy of Toshiba of Canada Limited.)

1.2 Thermodynamics

1.2.1 Basic Reactions

A PEM fuel cell consists of an electrolyte sandwiched between two electrodes. At the surfaces of the two electrodes, two electrochemical reactions take place. At the anode, over which hydrogen gas passes, occurs the HOR. At the cathode, over which oxygen or air passes, occurs the ORR. The two electrode reactions are as follows:

Anode Reaction:



corresponding to an anode potential $E_a^0 = 0.00\text{V}$ (under standard conditions) versus SHE.

Cathode Reaction:



corresponding to a cathode potential $E_c^0 = 1.229\text{V}$ (under standard conditions) versus SHE. Therefore, the overall reaction of the fuel cell is



with the equilibrium standard electromotive force calculated to be 1.229 V.

1.2.1.1 Oxygen Reduction Reaction

The ORR is well recognized as sluggish. The slow kinetics constitutes one of the major voltage losses due to a high reduction overpotential in the performance of a

PEMFC, and is one of the most limiting factors in the energy conversion efficiency of the state-of-the-art PEMFC [52]. Thus, investigation of the ORR remains a major focus of PEMFC research [53–56].

Generally speaking, the ORR process on Pt catalysts includes several individual reactions, as shown in Figure 1.19. Two general processes are the most examined, with each process containing a few discrete steps. One is the production of water through a four-electron pathway, and the other is production of hydrogen peroxide through a two-electron pathway. The desired route for a successful ORR catalyst would reduce oxygen molecules to water through the four-electron pathway. Incomplete reduction of oxygen to hydrogen peroxide not only leads to low energy conversion efficiency, but also produces reactive intermediate that can further convert to harmful free radical species.

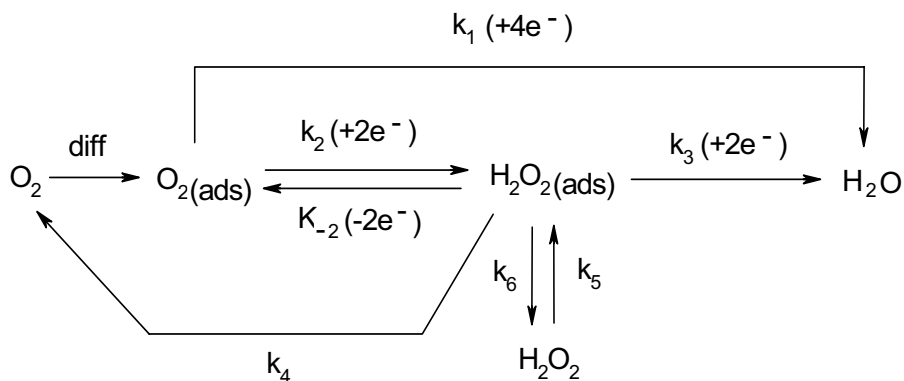


Figure 1.19. Oxygen reduction mechanism on noble catalysts [52]. (Reprinted from Journal of Power Sources, 152(2), Wang Bin, Recent development of non-platinum catalysts for oxygen reduction reaction, 1–15, ©2005, with permission from Elsevier.)

Table 1.5. ORR catalysts

Noble metals		Non-noble metal electrodes	Organometallic complexes
Bulk noble metals	Nanoparticulate noble metals		
Pt	Titanium dioxide nanoparticles on gold (Au/TiO ₂) [60]	Copper [65]	Transition metal complexes with porphyrin ligands [71–73]
Ru [57]		Ni [66]	
Cu/Ru [58]	Palladium nanoparticles on gold [62]	TiO ₂ on Ti [67]	Transition metal complexes with non-porphyrin ligands [74–78]
Au [59, 60]		Vanadium oxides [68]	
Pd /Co [61]	Palladium nanoparticles on carbon nanotubes [63]	WC+Ta [69]	
	Silver nanoparticles on carbon [64]	Lanthanum manganite [70]	

Minimizing the kinetic voltage loss resulting from the slow ORR on Pt catalysts has been studied over the past decades. As Pt is scarcely available even at a high price, alternative materials are highly sought after for fuel cell applications. To date, noble metal electrodes, non-noble metal electrodes, and organometallic complexes have been developed and studied to catalyze the ORR for PEMFCs, as listed in Table 1.5.

1.2.1.2 Hydrogen Oxidation Reaction

At the anode, hydrogen is stripped of its electrons and becomes protons and electrons. For electrochemical reactions, even if a simple one electron reaction is not that simple and is always with a reaction mechanism involving several steps. The overall reaction rate depends on the slowest elementary reaction, which is called the rate determining step. The steps of H₂ oxidation on Pt electrode include the following:



Platinum (Pt)-based catalysts are widely used as the anodic electrode material for hydrogen oxidation. The HOR on Pt catalysts has a lower oxidation overpotential and a higher kinetic rate. The apparent exchange current density of the HOR has been calculated to be $i_{\text{anode}}^0 = 0.1 \text{ A cm}^{-2}$, which is extremely high compared with that of ORR ($i_{\text{cathode}}^0 = 6 \mu \text{ A cm}^{-2}$), according to the charge transfer resistances of the cathode and anode obtained from electrochemical impedance spectroscopy (EIS) measurements done by Wagner et al. [79]. This proves the extreme fast reaction kinetics of HOR. Table 1.6 presents the exchange current densities of the hydrogen evolution reaction at different electrode materials in aqueous 1 M H₂SO₄ solution at ambient temperature [80].

Unfortunately, for many practical applications, the presence of a trace level (parts per million (ppm)) of carbon monoxide (CO) in the hydrogen-rich gas mixture produced by the reforming of other fuels is inevitable. CO can strongly adsorb on the Pt catalyst in the anode. The adsorbed CO, even mere traces (10 ppm), blocks the catalytically active area, thereby significantly decreasing its reactivity and causing so-called “CO poisoning.” Due to this, an excellent anode catalyst in PEM fuel cells has to show not only high catalytic activity toward hydrogen oxidation, but also enhanced activity in the presence of CO. The search for CO-tolerant catalysts has been a challenging task in the successful development of more efficient PEMFC systems [81].

Electrocatalysts based on Pt and oxophilic elements, such as ruthenium (Ru), tin (Sn), molybdenum (Mo), and tungsten (W), have shown significant improvement in CO tolerance compared to pure Pt. Two mechanisms have been proposed for explaining the enhanced CO tolerance of these materials, a bifunctional mechanism, through which the poisoning effect is reduced by the

occurrence of a surface reaction between Pt-adsorbed CO and oxygenated species produced at oxophilic neighbor sites, and an electronic effect, which is associated with an energy shift of the Pt electronic states caused by the second element and results in a weakening of the Pt-CO interactions [81].

Table 1.6. Exchange current densities of the hydrogen evolution reaction at different electrode materials in aqueous 1 M H₂SO₄ solution at ambient temperature [80]. (Reprinted from Wendt H, Spinacé EV, Oliveira Neto A, Linardi M. Electrocatalysis and electrocatalysts for low temperature fuel cells: fundamentals, state of the art, research and development. Quím Nova 2005;28:1066–75. With permission from Sociedade Brasileira de Química.)

Metal	i^0 / Acm^{-2}
Palladium, Pd	1.0×10^{-3}
Platinum, Pt	8.0×10^{-4}
Rhodium, Rh	2.5×10^{-4}
Iridium, Ir	2.0×10^{-4}
Nickel, Ni	7.0×10^{-6}
Gold, Au	4.0×10^{-6}
Tungsten, W	1.3×10^{-6}
Niobium, Nb	1.5×10^{-7}
Titanium, Ti	7.0×10^{-8}
Cadmium, Cd	1.5×10^{-11}
Manganese, Mn	1.3×10^{-11}
Thallium, Tl	1.0×10^{-11}
Lead, Pb	1.0×10^{-12}
Mercury, Hg	0.5×10^{-13}

PtRu, the current choice for HOR catalysts, exhibits excellent CO tolerance, which could be ascribed to a decrease in CO binding energy on Pt due to electronic substrate effects and to the oxidation of chemisorbed carbon monoxide being catalyzed at low potentials by the activation of H₂O [82]. Ternary Pt-based catalysts have also been investigated in which a third oxophilic component such as Sn, Ir, Rh, Os, Mo, W, WO₃, or Re is added to promote CO oxidation at lower potentials [83].

1.2.1.3 Methanol/Ethanol/Formic Acid Oxidation

In recent years, interest in the development of direct liquid fuel cell (DLFC) has increased considerably due to its advantages: easy handling and storing of the liquid fuel, no need for reforming, and favorable power capability for the use portable electronics powered by miniature fuel cells. Most investigators are

exploring DMFCs [84, 85] for this purpose, while some are focused on DEFCs and DFAFCs [86–90].

Besides methanol, ethanol, and formic acid, other liquid chemicals have also been investigated as fuels for different DLFCs, such as 2-propanol, dimethyl ether, ethylene glycol, dimethoxymethane, trimethoxymethane, tetramethyl orthocarbonate, and hydrazine [91].

Simple organic compounds, such as methanol, ethanol, and formic acid, have several advantages with regard to their use as fuels. They are easy to store and handle. They possess a high energy density in the order of 1 kWh/kg, and they can be readily generated from biomass. Last but not least, due to their simple structures they should have the simplest and most straightforward reaction mechanisms of all the possible organic fuels [92]. Although more complex organic fuels are of academic interest, they probably are more expensive and have more complicated reaction mechanisms due to the fact that a molecule possesses several carbon atoms.

Strategies for the development of novel catalytic materials and the design of highly active catalysts for DLFC applications largely depend on a detailed understanding of the reaction mechanism and, in particular, of the rate-limiting step(s) during the electrooxidation under continuous reaction conditions. The most commonly used technique in the electrochemical studies of fuel cell reaction mechanisms has been voltammetry, chronoamperometry (chronopotentiometry), *in situ* spectroscopic techniques, e.g., electrochemically modulated infrared spectroscopy (EMIRS) and infrared reflection-absorption spectroscopy (IRRAS), differential electrochemical mass spectroscopy (DEMS) and ex-situ techniques, e.g., X-ray photoelectron spectroscopy (XPS) [92].

Methanol Oxidation

The oxidation of methanol has been thoroughly studied for many years and the mechanism is now well established. The overall oxidation reaction involves six electrons and one water molecule,



corresponding to an anode potential $E_a^0 = 0.016\text{V}$ (under standard conditions) versus SHE, resulting in the equilibrium standard electromotive force of 1.213 V for a DMFC. The overall reaction of the cell is



As Pt is the best anode for hydrogen oxidation, numerous studies deal with the direct oxidation of methanol on Pt in acid media, as well as in alkaline media [93]. It is reported that the dissociative adsorption of methanol on Pt-based catalysts occurs via the formation of irreversibly adsorbed CO species (a reaction intermediate), either linearly bonded or bridge bonded to the Pt surface [94]; the CO species acts as a poison to the catalytic surface, rapidly lowering its activity.

The coverage degree by linearly bonded CO can reach 90% on a pure Pt electrode, so that most of the active sites are blocked.

Since the oxidation of methanol to CO includes six electrons, the reaction process must involve several steps with several products or intermediates. The results from mass spectral measurements, high performance liquid chromatography (HPLC), and gas chromatography (GC) absorbance have showed that H&O, HCOOH, HCOOCH, and CO₂ were all produced during the oxidation of methanol on Pt in acid solutions. These species were formed initially but eventually became CO [92]. In addition, some other adsorbed species such as (CHO)_{ads} or (COOH)_{ads} were identified by infrared reflectance spectroscopy or Fourier transform infrared reflectance spectroscopy. The detailed reaction mechanism of methanol oxidation on a Pt electrode is shown in Figure 1.20 [94].

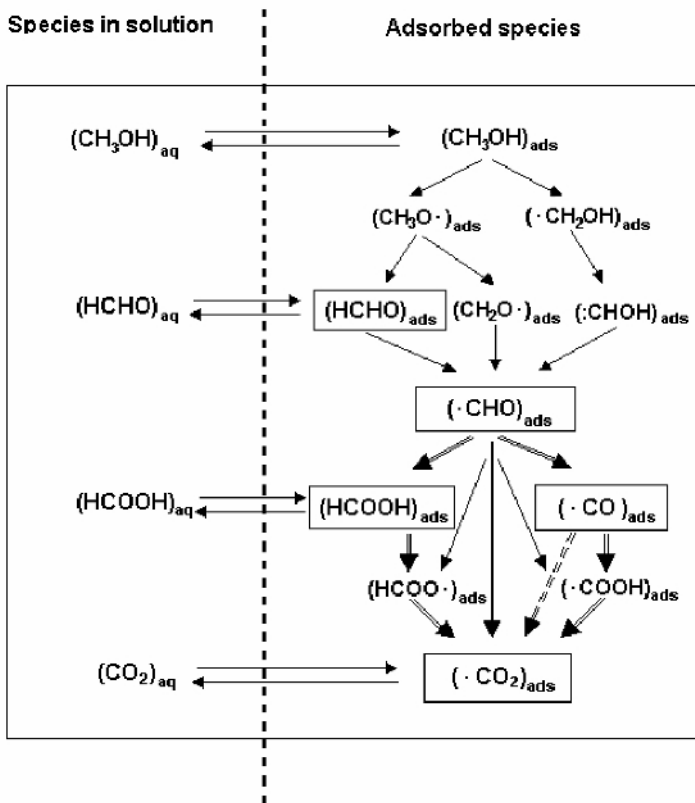
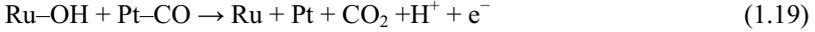


Figure 1.20. Detailed reaction mechanism of methanol oxidation on a Pt electrode [94]. (Reprinted from Journal of Power Sources, 105(2), Lamy C, Lima A, LeRhun V, Delime F, Coutanceau C, Léger J-M, Recent advances in the development of direct alcohol fuel cells (DAFC), 283–96, ©2002, with permission from Elsevier.)

In this mechanism, the adsorbed species $(\text{CHO})_{\text{ads}}$ plays a key role. Therefore, the strategy to develop efficient electrocatalysts is to favor this adsorbed species and to avoid the subsequent formation of adsorbed CO, either to prevent its

formation by blocking neighbouring Pt sites, to oxidize it at lower potentials, or to remove it [94].

To overcome CO deactivation, alloys of Pt with more oxophilic elements have been investigated as methanol electrooxidation catalysts. PtRu bifunctional catalysts are presently the most active for methanol oxidation. It is believed that Ru serves the role of removing CO_{ads} as CO_2 [93]:



Its role is thought to be a combination of two effects: (1) a bifunctional mechanism in which a partially oxidized Ru surface supplies the oxygenated species necessary for complete oxidation to CO_2 of the methanol adsorption residue, and (2) the ligand effect, in which the presence of Ru atoms close to Pt changes the electronic structure of Pt, allowing the weakening of the Pt-CO bond [95].

Studies of the temperature dependence of methanol oxidation indicate apparent activation energies of 41 to 56 kJ/mol [96] and 55 kJ/mol [97], which suggests that the methanol adsorption is rate determining because these values are comparable to the adsorption energies [96].

Ethanol Oxidation

Since ethanol is the major renewable bio-fuel and is less toxic than other alcohols, it is a promising alternative liquid fuel for directly fuelled DLFC systems. A schematic of a DEFC is shown in Figure 1.21.

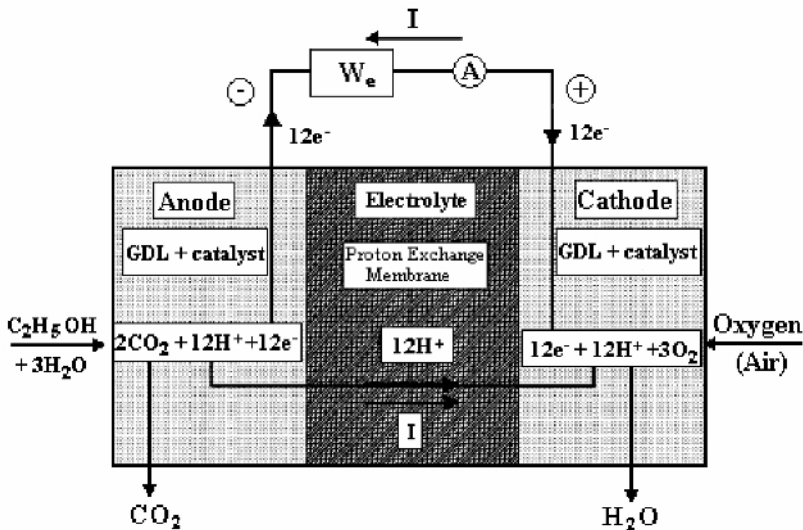
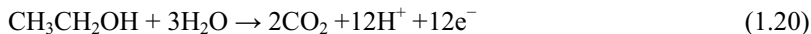


Figure 1.21. Schematic of a DEFC 95. (Reprinted from Journal of Power Sources, 105(2), Lamy Claude, Lima Alexandre, LeRhun Véronique, Delime Fabien, Coutanceau Christophe and Léger Jean-Michel, Recent advances in the development of direct alcohol fuel cells (DAFC), 283–96, ©2002, with permission from Elsevier.)

The electrode reactions of a DEFC are expressed as follows [98]:

Anode reaction:



corresponding to an anode potential $E_a^0 = 0.084V$ versus SHE as calculated from thermodynamic data [94].

Cathode reaction:



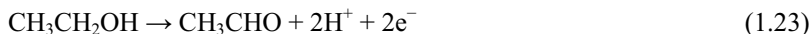
corresponding to a cathode potential $E_c^0 = 1.229V$ versus SHE.

Overall reaction:



Therefore, the equilibrium standard electromotive force can be calculated to be 1.145 V.

As the complete electrooxidation of ethanol in an acid medium yields two molecules of CO_2 and 12 electrons per ethanol molecule and involves the cleavage of the C–C bond, which requires rather high activation energy, the anodic ethanol electrooxidation on Pt is very sluggish, especially at low temperatures [99]. Despite significant efforts and numerous studies, the mechanism of the ethanol electrooxidation reaction still remains unclear; some studies are even contradictory. Nevertheless, electrooxidation of ethanol often does not proceed to completion, yielding adsorbed intermediates such as acetaldehyde [100, 101]:



Much of the effort on the electrooxidation of ethanol has been devoted mainly to identifying the adsorbed intermediates on the electrode and elucidating the reaction mechanism by means of various techniques, as differential electrochemical mass spectrometry, *in situ* Fourier transform infrared spectroscopy, and electrochemical thermal desorption mass spectroscopy. The established major products include CO_2 , acetaldehyde, and acetic acid, and it has been reported that methane and ethane have also been detected. Surface-adsorbed CO is still identified as the leading intermediate in ethanol electrooxidation, as it is in the methanol electrooxidation. Other surface intermediates include various C_1 and C_2 compounds such as ethoxy and acetyl [102]. There is general agreement that ethanol electrooxidation proceeds via a complex multi-step mechanism, which involves a number of adsorbed intermediates and also leads to different by-products for incomplete ethanol oxidation, as shown in Figure 1.22.

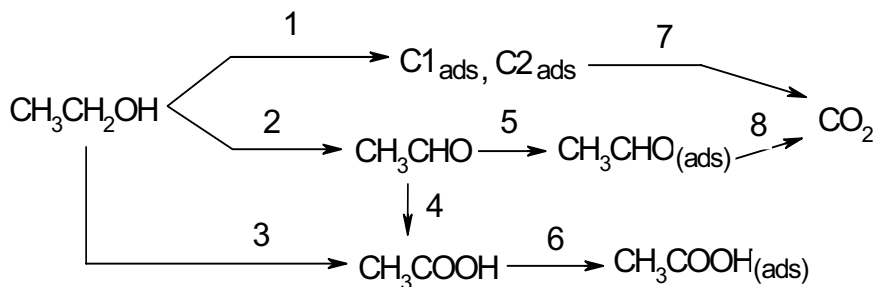


Figure 1.22. A probable reaction pathway for the electrooxidation of ethanol [103]. (Reproduced by permission of ECS—The Electrochemical Society, from Oliveira Neto A, Giz MJ, Perez J, Ticianelli EA, Gonzalez ER. The electrooxidation of ethanol on Pt-Ru and Pt-Mo particles supported on high-surface-area carbon.)

Total oxidation:



Partial oxidation:



CO_2 is the most common product. Other products and by-products such as acetaldehyde and acetic acid will inevitably decrease the fuel efficiency. The electrooxidative removal of CO-like intermediates and the cleavage of the C–C bond are the two main obstacles and rate determining steps. It is clear that ethanol electrooxidation involves more intermediates and products than that of methanol, and thus more active electrocatalysts are needed to promote ethanol electrooxidation at lower temperatures [102]. Although there are some similarities in the oxidation of low molecular weight alcohols on Pt (e.g., CO is produced as intermediate), the best catalyst is not the same for all situations. Contrary to what was found for the oxidation of methanol, the more effective catalyst for the oxidation of ethanol is not necessarily a Pt-Ru alloy [104].

The presence of both poisoning species and intermediate reaction products requires the development of new electrocatalysts able to break the C–C bond and to oxidize adsorbed CO at low temperatures [94]. Numerous studies have been carried out to develop more active electrocatalysts for ethanol electrooxidation. Besides Pt, other metals such as gold, rhodium, and palladium have been investigated as anode catalysts for ethanol electrooxidation and show certain activities [105]. On gold in an acid medium, the oxidation reaction leads mainly to the formation of acetaldehyde [94]. The oxidation of ethanol on rhodium proceeds mainly through the formation of acetic acid and CO.

Rousseau et al. [106] and Song et al. [107] investigated Pt-based catalysts for ethanol electrooxidation. Zhou et al. [102, 105] studied bi- and tri-metallic Pt-based catalysts with the addition of Ru, Pd, Sn and H. Wang et al. [108] developed ethanol electrooxidation catalysts on carbon-supported Pt, PtRu and Pt₃Sn. Colmati

et al. [104] also studied carbon-supported PtSn electrocatalysts. CuNi alloy-supported electrocatalysts has been investigated by Gupta et al. [93, 109]. Lux and Cairns [100, 101] developed lanthanide-platinum intermetallic compounds for ethanol oxidation.

Formic Acid Oxidation

As formic acid is nontoxic and has two orders of magnitude less crossover through a Nafion membrane than methanol [110], DFAFCs have been attracting increasing attention [88].

The electrooxidation of formic acid itself has been intensively investigated. The overall oxidation reaction of formic acid is



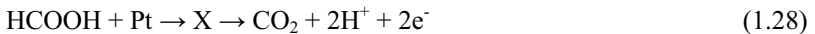
corresponding to an anode potential $E_a^0 = -0.171\text{V}$ (under standard conditions) versus SHE. Therefore, the equilibrium standard electromotive force of the overall cell reaction,



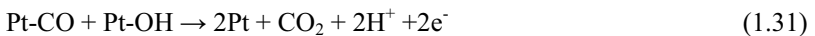
is calculated to be 1.400 V for a DFAFC [91].

In most cases, formic acid oxidation has been studied at Pt or modified Pt surfaces [111, 112]. Pt-Pd [113] and Pt-Ru [114] have also been studied. A variety of other catalyst investigations have been carried out, including palladium (Pd-C [115], Pd-P [116], Pd-M, where M is a base transition metal (M = Ti, Zr, Hf, V, Nb, Ta, Cr, Mo, W, or Au)), rhodium, iridium, and gold [117].

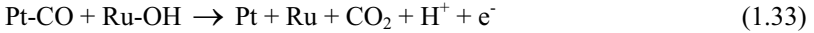
The oxidation of formic acid is not straightforward, although there is general agreement concerning the mechanism of formic acid electrooxidation on a Pt surface. The reaction is thought to branch into two pathways. In the first, formic acid is oxidized directly and relatively rapidly to CO_2 via a weakly bound reactive intermediate [113, 114, 118]:



In the second pathway, formic acid is indirectly oxidized to CO_2 relatively slowly through a strongly bound, poisoning CO intermediate:



The poisoning CO intermediate limits the activity of pure Pt toward formic acid oxidation by blocking the reaction sites. It is reported that Pt/Ru can activate water on the Ru atoms to create the added reaction pathway [114].



Since Ru forms surface hydroxides readily at lower potentials (0.3 V) than Pt (0.6 V), Reaction 1.33 occurs more swiftly than Reaction 1.31, which provides a faster pathway for CO oxidation and improves activity toward oxidation of formic acid [114].

1.2.2 Heat of Reaction

1.2.2.1 Enthalpy of Reaction

For a hydrogen fuel cell, the overall reaction (Equation 1.13) is the same as the reaction of hydrogen combustion, which is an exothermic process.



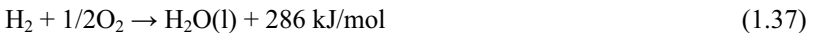
The heat or enthalpy of a chemical reaction is the difference between the heats of formation of products and reactants. For the above equation, the heat or enthalpy is

$$\Delta H = (h_f)_{\text{H}_2\text{O}} - (h_f)_{\text{H}_2} - 1/2(h_f)_{\text{O}_2} \quad (1.35)$$

The heat of formation of liquid water is -286 kJ/mol at $25 \text{ }^\circ\text{C}$ and heat of formation of elements is by definition equal to zero. Therefore,

$$\Delta H = -286 \text{ kJ/mol} - 0 - 0 = -286 \text{ kJ/mol} \quad (1.36)$$

The negative sign of the enthalpy means that this is an exothermic reaction. The fuel cell reaction can now be written as



This equation is valid at $25 \text{ }^\circ\text{C}$ only, meaning that both the reactant gases and the product water are at $25 \text{ }^\circ\text{C}$. At $25 \text{ }^\circ\text{C}$ and atmospheric pressure water is in liquid form [1].

The enthalpy of the hydrogen combustion reaction is also called the hydrogen's heating value. The value 286 kJ/mol is known as hydrogen's higher heating value (HHV), which means that 1 mol of hydrogen is fully combusted with $1/2$ mol of oxygen and cooled down to $25 \text{ }^\circ\text{C}$. If hydrogen is combusted with sufficient excess oxygen and cooled down to $25 \text{ }^\circ\text{C}$, the value will become 242 kJ/mol , which is known as hydrogen's lower heating value (LHV) [1].

1.2.2.2 Gibbs Free Energy

The change in Gibbs free energy (ΔG_f) of a reaction is the difference between the Gibbs free energy of the product and the Gibbs free energy of the reactants. For the hydrogen/oxygen fuel cell reaction (Equation 1.13), the change in Gibbs free energy is

$$\Delta G_f = G_{f,products} - G_{f,reactants} = G_{f,H_2O} - G_{f,H_2} - G_{f,O_2} \quad (1.38)$$

The change in Gibbs free energy varies with both temperature and pressure,

$$\Delta G_f = \Delta G_f^0 - RT \ln \left[\frac{p_{H_2} p_{O_2}^{1/2}}{p_{H_2O}} \right] \quad (1.39)$$

where ΔG_f^0 is the change in Gibbs free energy at standard pressure, which varies with the temperature T of the fuel cell, in Kelvin. p_{H_2} , p_{O_2} , and p_{H_2O} are the partial pressure of the hydrogen, oxygen, and vapor, respectively. R is the universal gas constant ($8.314 \text{ J}/(\text{kg} \cdot \text{K})$). The fact that the value of ΔG_f^0 is negative means that the energy is released from the reaction [119].

1.2.2.3 Reversible Fuel Cell Potential

If the fuel cell is reversible, which means that all the Gibbs free energy would be converted to electrical energy, the voltage of the fuel cell is related to the change of Gibbs free energy of the reaction by the following equation,

$$\Delta G_f = -nFE \quad (1.40)$$

where F is Faraday constant (96485 coulombs) and E is the voltage of the fuel cell. The number n in the equation is the number of electrons. In the case of a hydrogen fuel cell, for each mole of hydrogen two moles of electrons pass around the external circuit ($n = 2$). So the physical meaning of $2FE$ is the electrical work (charge \times voltage). E is called the reversible fuel cell potential, also known as the thermodynamic potential.

1.2.3 Effect of Operation Conditions on Reversible Fuel Cell Potential

1.2.3.1 Temperature Dependence of the Reversible Fuel Cell Potential

The reversible voltage of the fuel cell, also known as Nernst voltage, can be expressed using the Nernst equation,

$$E = \frac{-\Delta G_f}{2F} = \frac{-\Delta G_f^0}{2F} + \frac{RT}{2F} \ln \left[\frac{p_{H_2} p_{O_2}^{1/2}}{p_{H_2O}} \right] \quad (1.41)$$

At standard state (25 °C and 1 atm), the value of the term $\frac{-\Delta G_f^0}{2F}$ is

$$E = \frac{-\Delta G_f^0}{2F} = \frac{237,200\text{J/mol}}{2 \times 96485\text{As/mol}} = 1.229\text{ V} \quad (1.42)$$

Therefore, the reversible (theoretical) hydrogen/oxygen fuel cell potential is 1.229 V at standard state (25 °C and 1 atm). This value varies with temperature,

$$\frac{-\Delta G_f^0}{2F} = 1.229 + (T - T^0) \left(\frac{\Delta S^0}{2F} \right) \quad (1.43)$$

where T^0 is the standard-state temperature, which is 298.15 K, and ΔS^0 is the entropy change. The entropy change of a given reaction is approximately constant and can be set to the standard value, as follows [119]:

$$\frac{-\Delta G_f^0}{2F} = 1.229 - 0.85 \times 10^{-3} (T - 298.15) \quad (1.44)$$

The calculated change in the Gibbs free energy of the fuel cell reaction, ΔG_f^0 , and the reversible fuel cell voltage (reversible OCV) at standard pressure are given in Table 1.7. The reversible fuel cell potential at different temperatures and standard pressure is also depicted in Figure 1.23.

Table 1.7. Change in Gibbs free energy, reversible cell voltage, and efficiency limit (HHV basis) of hydrogen fuel cell reaction at different temperatures [26]. (From Larminie J, Dicks A. Fuel cell systems explained. ©2003 John Wiley & Sons Limited. Reproduced with permission.)

Form of Water Product	Temperature (°C)	ΔG_f^0 (kJ/mol)	Reversible cell voltage (V)	Theoretical Efficiency (%)
Liquid	25	-237.2	1.23	83
Liquid	80	-228.2	1.18	80
Gas	100	-225.2	1.17	79
Gas	200	-220.4	1.14	77
Gas	400	-210.3	1.09	74
Gas	600	-199.6	1.04	70
Gas	800	-188.6	0.98	66
Gas	1000	-177.4	0.92	62

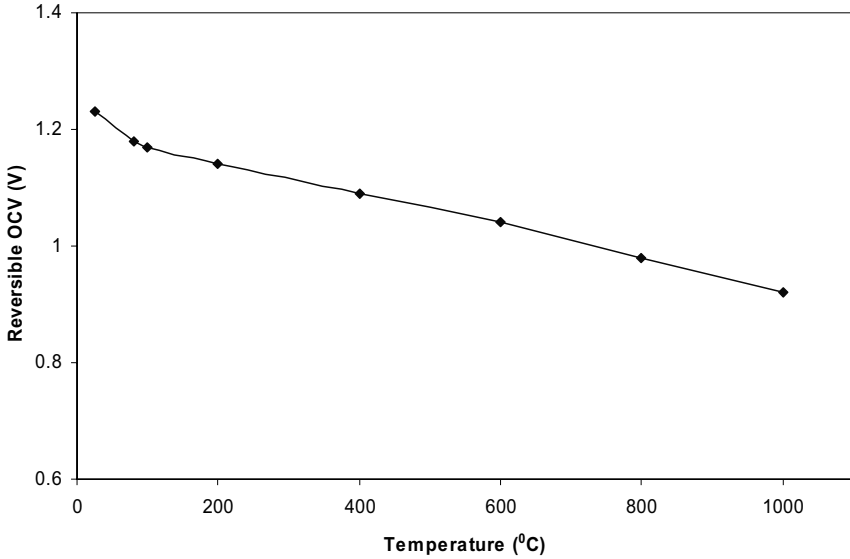


Figure 1.23. Reversible OCV at different temperatures and standard pressure

1.2.3.2 Pressure Dependence of the Reversible Fuel Cell Potential

The reversible cell potential or Nernst voltage of a hydrogen fuel cell is yielded according to Equation 1.41 and 1.44,

$$E_{Nernst} = 1.229 - 0.85 \times 10^{-3} (T - 298.15) + 4.3085 \times 10^{-5} T [\ln(p_{H_2}) + 1/2 \ln(p_{O_2})] \quad (1.45)$$

where T is expressed in Kelvin, and p_{H_2} , and p_{O_2} are expressed in atm. It can be seen in Equation 1.45 that both the temperature and the pressure will affect the reversible cell potential [119].

1.2.4 Open Circuit Voltage

1.2.4.1 Theoretical OCV

As described in Section 1.2.3.2, the reversible cell potential or Nernst voltage of a hydrogen fuel cell can be expressed as Equation 1.45. This value is what we call the theoretical OCV, and it is affected by both the temperature and the pressure.

A theoretical fuel cell OCV, E_{Theor}^{OCV} , can be written as

$$E_{Theor}^{OCV} = E_c^r - E_a^r \quad (1.46)$$

where E_c^r and E_a^r can be expressed in the Nernst form shown in Equation 1.47 and 1.48, respectively:

For cathode reaction: $O_2 + 4H^+ + 4e^- \leftrightarrow 2H_2O$

$$E_c^r = E_c^0 + \frac{RT}{4F} \ln(P_{O_2} [H^+]^4) \quad (1.47)$$

For anode reaction: $H_2 \leftrightarrow 2H^+ + 2e^-$

$$E_a^r = E_a^0 + \frac{RT}{2F} \ln\left(\frac{[H^+]^2}{P_{H_2}}\right) \quad (1.48)$$

In Equations 1.47 and 1.48, E_c^0 and E_a^0 are the standard cathode and anode potentials, respectively. E_c^0 is a temperature-dependent constant ($= 1.229 - 0.00085 \times (T - 298.15)$ [120]). E_a^0 is zero at any temperature. P_{O_2} and P_{H_2} are the partial pressures (atm) of O_2 and H_2 , respectively, and $[H^+]$ is the molar concentration of protons (mol/L). A theoretical OCV can be calculated by deriving Equations 1.47 and 1.48 to yield Equation 1.49, which can be further derived to yield Equation 1.45:

$$\begin{aligned} E_{theor}^{OCV} &= 1.229 - 0.00085(T - 298.15) + \frac{RT}{4F} \ln[P_{O_2} (P_{H_2})^2] \quad (1.49) \\ &= 1.229 - 0.85 \times 10^{-3} (T - 298.15) + 4.3085 \times 10^{-5} T [\ln(p_{H_2}) + 1/2 \ln(p_{O_2})] \end{aligned}$$

The theoretical OCV has the same value as the reversible cell potential. However, even when no current is drawn from a fuel cell, there is irreversible voltage loss, which means that the actual values of the OCV are always lower than the theoretically expected values. To date, a quantitative explanation for such OCV behavior has not been clear in the literature. One explanation attributes this behavior to H_2 crossover and/or internal current, as described in the fuel cell book written by Larminie and Dicks [26]. A mixed potential [121–124] has also been widely used to interpret the lower OCV. The combined effects of fuel crossover, internal short, and parasitic oxidation reactions occurring at the cathode are the source of the difference between the measured open circuit cell voltage and the theoretical cell potential. Therefore, the actual OCV is expressed as

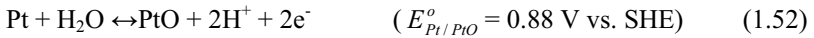
$$E_{OCV} = E_{theor}^{OCV} - E_{cross} - E_{mix} \quad (1.50)$$

1.2.4.2 Mixed Potential

In general, the mixed potential is composed of both the cathodic O_2/H_2O reaction potential



and the Pt/PtO anodic reaction potential



The local electrochemical reaction on the Pt surface creates a Pt-O surface coverage of 30%, and the remaining 70% remains as pure Pt. At steady-state mixed potential, a complete layer of Pt-O can never be achieved in order to keep the reaction of Pt to Pt-O continued due to the diffusion of Pt-O into the bulk metal. The reported mixed cathode potential is around 1.06 V (vs. SHE) at standard conditions (25 °C, 1 atm) with an O₂ partial pressure dependence of 15 mV atm⁻¹ [124, 125].

1.2.4.3 Fuel Crossover

Another OCV loss is caused by the crossover of fuel through the electrolyte. Ideally the electrolyte allows the transport of only ions. In reality, however, some fuel permeates across the membrane from the anode to the cathode. In addition, some direct transfer of electrons across the membranes can occur and cause electronic short. A fuel loss due to crossover leads to a current loss. The current loss associated with an electrical short is generally small (ca. few milli-amperes) relative to the typical operating current of a fuel cell, and therefore is not a significant source of current inefficiency. However, these effects have a significant effect on the OCV of the cell. This is particularly true of a low-temperature cell, in which activation losses are considerable [126].

Fuel that has crossed over can react with O₂ to produce a corresponding cathodic current density in the same order of magnitude, resulting in a depression of the cathode potential. It is believed that the H₂ that has crossed over can form a local half-cell electrochemical reaction on the cathode, such as $\text{H}_2 \leftrightarrow 2\text{H}^+ + 2\text{e}^-$, resulting in a mixed cathode potential, in a way similar to that of the half-cell reaction ($\text{Pt} + \text{H}_2\text{O} \leftrightarrow \text{PtO} + 2\text{H}^+ + 2\text{e}^-$).

H₂ Crossover

For a hydrogen fuel cell, H₂ crossover can be measured by linear sweep voltammetry or chronocoulometry. The linear sweep voltammetry procedure is similar to the cyclic voltammetry (CV) technique, with the principal difference being the irreversible scan. Humidified H₂ and N₂ are supplied to the anode and cathode sides of the fuel cell, respectively. The scan potential ranges from 0 to 0.8 V, with higher voltages being avoided to prevent Pt oxidation [127]. The experimental procedure involves controlling the potential of the fuel cell cathode (working electrode) and monitoring any electrochemical activity that occurs in the form of a current. Since N₂ gas is the only substance introduced into the cathode side, any current generated in the given potential range is attributed solely to the electrochemical oxidation of H₂ gas that crosses over from the anode side through the membrane. The crossover current typically increases with the scan potential and rapidly reaches a limiting value when the potential grows to around 300 mV [128]. At this value all crossover H₂ is instantaneously oxidized due to the high overpotential applied. Based on the limiting current, one can, ultimately, calculate

the flux of H_2 gas using Faraday's law. Using this diagnostic method, Song et al. [129] determined the hydrogen crossover rate through a Nafion 112 membrane at elevated temperatures up to 120 °C. A sample of a linear sweep voltammogram for different types of MEAs is presented in Figure 1.24 [127].

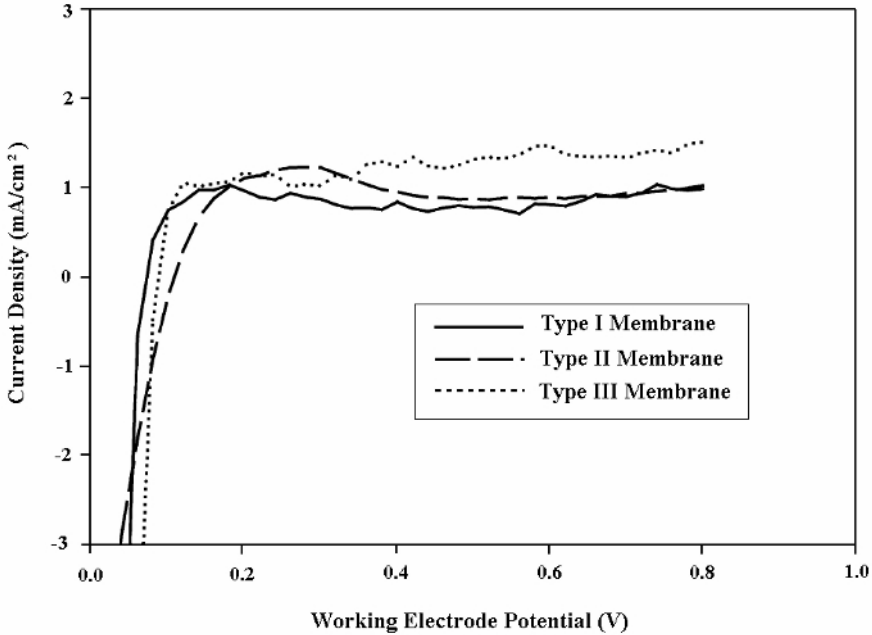


Figure 1.24. Sample of a linear sweep voltammogram on MEAs containing Nafion/PTA membranes of Types I–III (25% PTA loading). Scan rate 4 mV/s; room temperature; ambient pressure operation; 200 cm³ H₂ on anode; 200 cm³ N₂ on cathode [127]. (Reprinted from Journal of Membrane Science, 232, Ramani V, Kunz HR, Fenton JM, Investigation of Nafion[®]/HPA composite membranes for high temperature/low relative humidity PEMFC operation, 31–44 ©2004 with permission from Elsevier.)

Another method for measuring H_2 crossover through the membrane is chronocoulometry [130, 131]. The fuel cell is operated with hydrogen at the anode and nitrogen at the cathode. A certain potential, such as 0.5 V, is applied to the cathode side of the cell, which serves as the working electrode, instead of a potential scan. Hydrogen crossing over the membrane from the reverse electrode is oxidized completely at this potential. The electrical charge passing through this electrode is recorded as a function of time. By measuring the coulombs evolved by the oxidation, the H_2 crossover rate can be calculated as a mass transfer limited current.

Methanol Crossover

Fuel crossover occurs to some degree in all low-temperature fuel cells, particularly in DMFCs. For a DMFC, methanol crossover not only results in additional fuel consumption, but also reduces the cell voltage by the effect of mixed potential, and

the potential of the oxygen cathode is strongly influenced by the crossover of methanol through the membrane.

The most conventional method to determine methanol crossover in a DMFC is to monitor the CO₂ content in the cathode exhaust gas flux by using an optical infrared sensor, by gas chromatographic analysis, or by mass spectrometry [132]. However, these measurements are based on the assumptions that the crossed over methanol at the cathode is completely oxidized and that there is no CO₂ permeation from the anode to the cathode. In reality, in particular for operation at high current density, a large amount of CO₂ permeates from the anode to the cathode in the DMFC. So far, no reliable method is available to measure the methanol crossover through the membrane from the anode to the cathode at the operating status.

Nevertheless, efforts have been made to determine the CO₂ crossover. One method is to determine the CO₂ flux using half-cell measurements. At the anode, CO₂ is produced and passes together with methanol through the membrane to the cathode. At the cathode, nitrogen gas is flushed. The CO₂ flux through the membrane is determined because methanol is not oxidized at the cathode. Another method utilizes methanol-tolerant catalysts at the cathode in order not to oxidize the permeating methanol. The amount of CO₂ permeated to the cathode can be calculated from the missing CO₂ fraction in the anode exhaust by using a method of gravimetric determination of BaCO₃ [133].

1.2.5 Fuel Cell Efficiency

1.2.5.1 Carnot Efficiency

The efficiency of any energy conversion device is defined as the ratio between useful energy output and energy input. The efficiency limit for heat engines, such as steam and gas turbines, is known as the Carnot limit. If the maximum temperature of the heat engine is T_1 , and the heated fluid is released at temperature T_2 , which is never likely to be smaller than room temperature (about 290 K), then the Carnot limit of the efficiency can be calculated by

$$\text{Carnot limit} = \frac{T_1 - T_2}{T_1}, \quad (1.53)$$

where both the temperatures are in Kelvin. For a steam turbine operating at 400 °C (673 K) with water exhausted through a condenser at 50 °C (323 K), the Carnot efficiency limit is

$$\frac{673 - 323}{673} = 52\% \quad (1.54)$$

Basically, there must be some heat energy, proportional to the lower temperature T_2 that is always thrown away or wasted. Thus, the practical efficiency is always lower than the efficiency limit.

1.2.5.2 Theoretical Fuel Cell Efficiency

For a fuel cell, the useful energy output is the electrical energy produced, and energy input is the enthalpy of hydrogen. Assuming that all of the Gibbs free energy can be converted into electrical energy, the maximum possible (theoretical) efficiency of a fuel cell at 25 °C by using the hydrogen HHV is

$$\eta = \frac{\Delta G_f^0}{\Delta H^0} = \frac{237.1 \text{ kJ/mol}}{286 \text{ kJ/mol}} = 83\% \quad (1.55)$$

If both ΔG and ΔH are divided by nF , the fuel cell efficiency may be expressed as a ratio of two potentials:

$$\eta = \frac{\Delta G_f^0}{\Delta H^0} = \frac{\frac{-\Delta G_f^0}{nF}}{\frac{-\Delta H^0}{nF}} = \frac{1.23}{1.48} = 83\% \quad (25^\circ\text{C}, 1 \text{ atm}) \quad (1.56)$$

where 1.23 V is the theoretical cell potential, and 1.48 is the potential corresponding to hydrogen's HHV, or the thermoneutral potential.

The theoretical efficiency is sometimes also known as the thermodynamic efficiency or the maximum efficiency limit. The theoretical efficiency at different temperatures and standard pressure is shown in Figure 1.25. The data are also given in Table 1.7. It is clear that there is a connection between the reversible OCV of a cell and its theoretical efficiency (or maximum efficiency) based on the above equation.

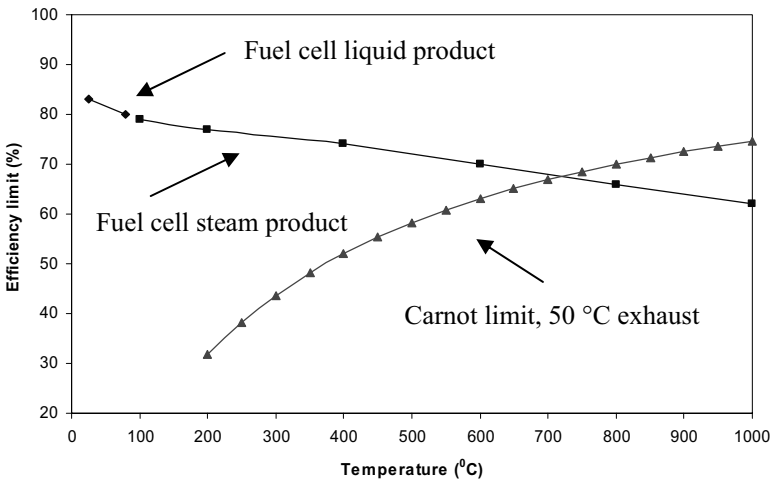


Figure 1.25. Theoretical H_2 fuel cell efficiency at standard pressure based on HHV [26]. (From Larminie J, Dicks A. Fuel cell systems explained. ©2003 John Wiley & Sons Limited. Reproduced with permission.)

1.2.5.3 Energy Conversion Efficiency for Fuel Cells

The actual efficiency of the cell is defined as the actual voltage divided by the thermoneutral potential, that is,

$$\text{Cell efficiency} = \frac{V_{cell}}{1.48} \times 100\% \quad (\text{based on HHV}) \quad (1.57)$$

If using the LHV, then

$$\text{Cell efficiency} = \frac{V_{cell}}{1.23} \times 100\% \quad (1.58)$$

In practice, a fuel cell is normally operated under conditions such that not all the fuel that is fed to the cell is consumed. Some fuel has to pass through unreacted. Therefore, there is another parameter that needs to be taken into account to calculate the cell efficiency, the fuel utilization coefficient, which is defined as

$$\mu_f = \frac{\text{mass of fuel reacted in cell}}{\text{mass of fuel input to cell}} \quad (1.59)$$

Thus, the fuel cell efficiency is expressed as [26]:

$$\text{Cell efficiency} = \mu_f \frac{V_{cell}}{1.48} \times 100\% \quad (\text{HHV}) \quad (1.60)$$

and

$$\text{Cell efficiency} = \mu_f \frac{V_{cell}}{1.23} \times 100\% \quad (\text{LHV}) \quad (1.61)$$

1.2.6 Summary

A comparison of the reactions, cell potentials, energy densities, theoretical efficiency, and other selected properties for PEM fuel cells with different fuels is summarized in Table 1.8.

Fuels	Reactions	$-\Delta G_f^\theta$ (kJ mol ⁻¹)	Theoretical potential, E^0 (V)	$-\Delta H^\theta$ (kJ mol ⁻¹)	Theoretical energy efficiency (%)
Hydrogen	Anode: $\text{H}_2 \rightarrow 2\text{H}^+ + 2\text{e}^-$	0	0.000		
	Cathode: $2\text{H}^+ + 2\text{e}^- + (1/2)\text{O}_2 \rightarrow \text{H}_2\text{O} (l)$		1.229		
	Overall: $\text{H}_2 + (1/2)\text{O}_2 \rightarrow \text{H}_2\text{O}$	237.1	1.229	285.8	0.830
Methanol	Anode: $\text{CH}_3\text{OH} (l) + \text{H}_2\text{O} \rightarrow \text{CO}_2 + 6\text{H}^+ + 6\text{e}^-$	9.3	0.016		
	Cathode: $6\text{H}^+ + 6\text{e}^- + (3/2)\text{O}_2 \rightarrow 3\text{H}_2\text{O} (l)$		1.229		
	Overall: $\text{HCOOH} (l) + (1/2)\text{O}_2 \rightarrow \text{CO}_2 + \text{H}_2\text{O} (l)$	270	1.400	254.3	0.967
Ethanol	Anode: $\text{C}_2\text{H}_5\text{OH} (l) + 3\text{H}_2\text{O} \rightarrow 2\text{CO}_2 + 12\text{H}^+ + 12\text{e}^-$	97.3	0.084		
	Cathode: $12\text{H}^+ + 12\text{e}^- + 3\text{O}_2 \rightarrow 6\text{H}_2\text{O} (l)$		1.229		
	Overall: $\text{C}_2\text{H}_5\text{OH} (l) + 3\text{O}_2 \rightarrow 2\text{CO}_2 + 3\text{H}_2\text{O} (l)$	1325	1.145	1367	0.969
Formic acid	Anode: $\text{HCOOH} (l) \rightarrow \text{CO}_2 + 2\text{H}^+ + 2\text{e}^-$	-33	-0.171		
	Cathode: $2\text{H}^+ + 2\text{e}^- + (1/2)\text{O}_2 \rightarrow \text{H}_2\text{O} (l)$		1.229		
	Overall: $\text{HCOOH} (l) + (1/2)\text{O}_2 \rightarrow \text{CO}_2 + \text{H}_2\text{O} (l)$	270	1.400	254.3	1.062
2-Propanol	Anode: $\text{C}_3\text{H}_7\text{OH} (l) + 5\text{H}_2\text{O} \rightarrow 3\text{CO}_2 + 18\text{H}^+ + 18\text{e}^-$	186.3	0.107		
	Cathode: $18\text{H}^+ + 18\text{e}^- + (9/2)\text{O}_2 \rightarrow 9\text{H}_2\text{O} (l)$		1.229		
	Overall: $\text{C}_3\text{H}_7\text{OH} (l) + (9/2)\text{O}_2 \rightarrow 3\text{CO}_2 + 4\text{H}_2\text{O} (l)$	1948	1.122	2005.6	0.971

Table 1.8. Comparison of selected properties for PEM fuel cells with different fuels under standard condition (25°C, 1 atm) [91]. (Reprinted from Journal of Power Sources, 154(1), Qian W, Wilkinson DP, Shen J, Wang H, Zhang J, Architecture for portable direct liquid fuel cells, 202–13, ©2006, with permission from Elsevier.)

Fuels	Reactions	$-\Delta G_f^\theta$ (kJ mol ⁻¹)	Theoretical potential, E ⁰ (V)	$-\Delta H^\theta$ (kJ mol ⁻¹)	Theoretical energy efficiency (%)
Hydrazine	Anode: $\text{N}_2\text{H}_4(\text{l}) \rightarrow \text{N}_2 + 4\text{H}^+ + 4\text{e}^-$	-149.2	-0.386		
	Cathode: $4\text{H}^+ + 4\text{e}^- + \text{O}_2 \rightarrow 2\text{H}_2\text{O}(\text{l})$		1.229		
	Overall: $\text{N}_2\text{H}_4(\text{l}) + \text{O}_2 \rightarrow \text{N}_2 + 2\text{H}_2\text{O}(\text{l})$	623.4	1.615	622.2	1.002
Dimethyl ether	Anode: $(\text{CH}_3)_2\text{O}(\text{g}) + 3\text{H}_2\text{O} \rightarrow 2\text{CO}_2 + 12\text{H}^+ + 12\text{e}^-$	35.4	0.031		
	Cathode: $12\text{H}^+ + 12\text{e}^- + 3\text{O}_2 \rightarrow 6\text{H}_2\text{O}(\text{l})$		1.229		
	Overall: $(\text{CH}_3)_2\text{O}(\text{g}) + 3\text{O}_2 \rightarrow 2\text{CO}_2 + 3\text{H}_2\text{O}(\text{l})$	1387.2	1.198	1460.3	0.950
Ethylene glycol	Anode: $\text{C}_2\text{H}_6\text{O}_2(\text{l}) + 2\text{H}_2\text{O} \rightarrow 2\text{CO}_2 + 10\text{H}^+ + 10\text{e}^-$	8.78	0.009		
	Cathode: $10\text{H}^+ + 10\text{e}^- + 5/2\text{O}_2 \rightarrow 5\text{H}_2\text{O}(\text{l})$		1.229		
	Overall: $\text{C}_2\text{H}_6\text{O}_2(\text{l}) + 5/2\text{O}_2 \rightarrow 2\text{CO}_2 + 3\text{H}_2\text{O}(\text{l})$	1176.7	1.220	1189.5	0.990
Dimethoxymethane	Anode: $(\text{CH}_3\text{O})_2\text{CH}_2(\text{l}) + 4\text{H}_2\text{O} \rightarrow 3\text{CO}_2 + 16\text{H}^+ + 16\text{e}^-$	2.18	0.002		
	Cathode: $16\text{H}^+ + 16\text{e}^- + 4\text{O}_2 \rightarrow 8\text{H}_2\text{O}(\text{l})$		1.229		
	Overall: $(\text{CH}_3\text{O})_2\text{CH}_2(\text{l}) + 4\text{O}_2 \rightarrow 3\text{CO}_2 + 4\text{H}_2\text{O}(\text{l})$	1894.6	1.227	1937.5	0.978

Table 1.8. (continued)

1.3 Reaction Kinetics

1.3.1 Electrode Reactions

A fuel cell is an electrochemical energy converter. Its operation is based on the following electrochemical reactions occurring simultaneously on the anode and the cathode [1]:

Anode Reaction:



At the anode, hydrogen is stripped of its electrons and become protons and electrons.

Cathode Reaction:



At the cathode, oxygen is oxidized, meaning that it takes the electrons and forms water. As described in Section 1.2, the HOR on Pt catalysts has a lower oxidation overpotential and a higher kinetic rate, whereas the ORR is sluggish, involving sequential and parallel steps.

1.3.2 Reaction Rate

More commonly, we use the following reaction to represent the anode and cathode reactions above.



where O_x stands for the oxidized form of the reactant and R_d stands for the reduced form of the reactant. The rate of an electrochemical reaction proceeding on the electrode surface is the speed at which the electrons are released or consumed.

1.3.2.1 Current Density and Exchange Current Density

Since electrode reactions are heterogeneous, their reaction rates are usually described in units of mol s^{-1} per unit area. In Equation 1.64, both elementary reactions are active at all times, and the rate of the forward process v_f ($\text{mol s}^{-1} \text{cm}^{-2}$) is

$$v_f = k_f C_{\text{O}_x} \quad (1.65)$$

whereas the rate of the reverse reaction is

$$v_b = k_b C_{Rd} \quad (1.66)$$

The rate constants, k_f and k_b , have dimensions of s^{-1} , and one can easily show that they are the reciprocals of the mean lifetimes of O_x and R_d , respectively. C_{O_x} , and C_{Rd} are the surface concentrations of the reacting species with a unit of mol/cm^2 . The net conversion rate of O_x to Rd is

$$v_{net} = k_f C_{O_x} - k_b C_{Rd} \quad (1.67)$$

The rate of an electrochemical reaction is determined by an activation energy barrier that the charge must overcome to move from electrolyte to a solid electrode or vice versa, and is described using the electrical current. Very often, we use current density (the current per unit area of the surface). The current density, i , is related to the charge transferred, the consumption of reactant, and the surface area by Faraday's law.

$$i = nFv \quad (1.68)$$

where F is Faraday's constant (96485 C/mol), and the physical meaning of nF is the charge transferred. v is the reactant consumed with a unit of $\text{mols}^{-1} \text{cm}^{-2}$.

The reaction rate, current density, is easy to measure. But note that this current density is a net current density, which is the difference between the forward and reverse current densities on the electrode. Generally, for a reaction in Equation 1.64, the net current density can be expressed as

$$i = nF(k_f C_{O_x} - k_b C_{Rd}) \quad (1.69)$$

where k_f is the forward reaction rate constant (s^{-1}), C_{O_x} is the surface concentration of the reacting species (mol cm^{-2}), k_b is the reverse reaction rate constant (s^{-1}), and C_{Rd} is the surface concentration of the reacting species (mol cm^{-2}).

At equilibrium, the net current is equal to zero. However, this does not mean that both the forward reaction and the backward reaction stop. Actually, both reactions proceed in opposite directions but with the same speed. The rate at which they proceed at equilibrium is called the exchange current density, i_0 [1].

$$i_0 = nFk_f C_{O_x} = nFk_b C_{Rd} \quad (1.70)$$

The value of the exchange current density depends on the inherent speed of the electrode reaction: a slow reaction (with a small exchange current density) will require a larger overpotential for a given current density than a fast reaction (with a large exchange current density).

1.3.2.2 Arrhenius Equation and Transition State Theory

The Arrhenius equation shows the dependence of the rate constant of chemical reactions on the temperature and activation energy. Its form is

$$k = A \exp\left(-\frac{E_a}{RT}\right) \quad (1.71)$$

where E_a is the activation energy, which has units of energy. A is known generally as the pre-exponential factor or frequency factor [134].

According to transition state theory, the rate constant for an electrochemical reaction is a function of the Gibbs free energy [1].

$$k = \frac{k_B T}{h} \exp\left(\frac{-\Delta G}{RT}\right) \quad (1.72)$$

where k_B is Boltzmann's constant and h is Planck's constant.

The Gibbs free energy for electrochemical reactions is considered to consist of both chemical and electrical terms. Therefore, for reduction reaction

$$\Delta G = \Delta G_{ch} + \alpha_{Rd} nFE \quad (1.73)$$

and for oxidation reaction

$$\Delta G = \Delta G_{ch} - \alpha_{Ox} nFE \quad (1.74)$$

where ΔG_{ch} is the chemical component of the Gibbs free energy, α is the transfer coefficient, F is Faraday's constant, and E is the potential. The value of α is theoretically between 0 and 1, and most typically for the reactions on a metallic surface it is around 0.5. The relationship of α_{Rd} and α_{Ox} is as follows:

$$\alpha_{Rd} + \alpha_{Ox} = 1 \quad (1.75)$$

Thus, the forward reduction and backward oxidation reaction rate constant can be expressed as

$$k_f = k_{0,f} \exp\left[\frac{-\alpha_{Rd} nFE}{RT}\right] \quad (1.76)$$

$$k_b = k_{0,b} \exp\left[\frac{\alpha_{Ox} nFE}{RT}\right] \quad (1.77)$$

where $k_{0,f}$ and $k_{0,b}$ are the standard rate constants for the forward reaction and backward reaction, respectively; that is, they are the rate constants when the electrodes are at thermodynamic standard potentials.

1.3.2.3 Butler-Volmer Equation

By introducing Equations 1.75, 1.76, and 1.77 into Equation 1.69, the net current density is obtained:

$$i = nF[k_{0,f}C_{Ox} \exp(\frac{-\alpha_{Rd}nFE}{RT}) - k_{0,b}C_{Rd} \exp(\frac{(1-\alpha_{Rd})nFE}{RT})] \quad (1.78)$$

At equilibrium, we have

$$i_0 = nFk_{0,f}C_{Ox}^b \exp(\frac{-\alpha_{Rd}nFE_{eq}}{RT}) = nFk_{0,b}C_{Rd}^b \exp(\frac{(1-\alpha_{Rd})nFE_{eq}}{RT}) \quad (1.79)$$

where E_{eq} is the reversible or equilibrium potential, and C_{Ox}^b and C_{Rd}^b are the bulk concentration of the reacting species (mol/cm^2). As described in Section 1.2, the reversible or equilibrium potential at the fuel cell anode and cathode at 25 °C and atmospheric pressure are 0 and 1.229 V, respectively. For simplicity, we define α as α_{Rd} .

According to Equation 1.78 and 1.79, we have

$$i = i_0 [\frac{C_{Ox}}{C_{Ox}^b} \exp(\frac{-\alpha nF(E - E_{eq})}{RT}) - \frac{C_{Rd}}{C_{Rd}^b} \exp(\frac{(1-\alpha)nF(E - E_{eq})}{RT})] \quad (1.80)$$

Then Equation 1.80 can be simplified as

$$i = i_0 [\frac{C_{Ox}}{C_{Ox}^b} \exp(\frac{-\alpha nF\eta}{RT}) - \frac{C_{Rd}}{C_{Rd}^b} \exp(\frac{(1-\alpha)nF\eta}{RT})] \quad (1.81)$$

where η is the overpotential (for the anode reaction $\eta_a = E_a - E_{eq} > 0$; for the cathode reaction $\eta_c = E_c - E_{eq} < 0$). Assuming $C_{Ox} = C_{Ox}^b$, and $C_{Rd} = C_{Rd}^b$,

$$i = i_0 [\exp(\frac{-\alpha nF\eta}{RT}) - \exp(\frac{(1-\alpha)nF\eta}{RT})] \quad (1.82)$$

Equation 1.82 is known as the Butler-Volmer equation, describing the current-potential relationship.

Applying the Butler-Volmer equation to a fuel cell anode and cathode reaction, the anodic and cathodic kinetic current densities can be expressed as Equations 1.83 and 1.84, respectively, and it is obvious that we have $i_c = -i_a$, where the

cathode current density is defined as positive and anode current density is defined as negative, when the fuel cell is under load.

$$i_a = i_{0,H_2} \left[\exp\left(\frac{-\alpha_H n_{\alpha,H} F \eta_a}{RT}\right) - \exp\left(\frac{(1-\alpha_H) n_{\alpha,H} F \eta_a}{RT}\right) \right] \quad (1.83)$$

$$i_c = i_{0,O_2} \left[\exp\left(\frac{-\alpha_O n_{\alpha,O} F \eta_c}{RT}\right) - \exp\left(\frac{(1-\alpha_O) n_{\alpha,O} F \eta_c}{RT}\right) \right] \quad (1.84)$$

where

- i_c = the cathodic current density
- i_a = the anodic current density
- i_{0,O_2} = the apparent exchange current density for cathodic O₂ reduction
- i_{0,H_2} = the apparent exchange current density for the anodic H₂ oxidation reaction
- R = the universal gas constant (8.314 J / mol · K)
- T = the temperature (K).
- F = Faraday constant (96485 C/mol)
- $n_{\alpha,O}$ = the electron transfer number in the rate determining step for cathodic O₂ reduction
- $n_{\alpha,H}$ = the electron transfer number in the rate determining step for anodic H₂ oxidation reaction
- α_O = the transfer coefficient in the rate determining step for cathodic O₂ reduction ($\alpha_O = \alpha_{O,Rd}$)
- α_H = the transfer coefficient in the rate determining step for anodic H₂ oxidation ($\alpha_H = \alpha_{H,Rd}$)

The value of $n_{\alpha,H}$ is 1.0, which has been widely reported in the literature [135–137]. For the value of $n_{\alpha,O}$, the literature presents two Tafel slopes for the oxygen reduction polarization curve [138–141]. The first case, where the slope is approximately 60 mV/decade at 25 °C, corresponds to a $n_{\alpha,O}$ value of 2.0 for $\alpha_O \approx 0.5$ in the low current density range (the higher cathode potential range where the electrode surface is partially covered by PtO). For the second case, the Tafel slope in the higher current density range is around 120 mV/decade with a $n_{\alpha,O}$ value of 1.0, corresponding to a low cathode potential range where the electrode surface is pure Pt.

α_O and α_H in Equations 1.83 and 1.84 are the electron transfer coefficients for cathodic O₂ reduction and anodic H₂ oxidation, respectively. On a Pt electrode, α_O is a temperature-dependent parameter as reported in the literature [142–145], and can be expressed as

$$\alpha_o = \alpha_o^0 T \quad (1.85)$$

where $\alpha_{O-Pt/PtO}^0 = 0.00168 \text{ K}^{-1}$ in the temperature range of 20 °C to 250 °C. However, α_H for H_2 oxidation on a Pt electrode seems to be independent of temperature and a value of 0.5 is widely reported in the literature [146–148].

1.3.2.4 Linear Polarization

At a small overpotential, that is, $\left| \frac{nF\eta}{RT} \right| \ll 1$, the Butler-Volmer equation can be simplified as

$$i = i_0 \left[1 - \frac{\alpha n F \eta}{RT} - \left(1 + (1 - \alpha) \frac{n F \eta}{RT} \right) \right] \quad (1.86)$$

That is,

$$i = -i_0 \frac{n F \eta}{RT} \quad (1.87)$$

Therefore, we have

$$R_{ct} = -\eta / i = \frac{RT}{n F i_0} \quad (1.88)$$

where R_{ct} is the charge transfer resistance, which refers to the barrier across which the electrons pass from the electrode surface to the adsorbed species or from the adsorbed species to the electrode. The resistance is related to the electrode potential, or more precisely, to the overpotential. R_{ct} is a very important kinetic parameter, describing the speed of the electrode reaction. R_{ct} can be obtained by AC impedance method.

Again, the electron number refers only to the electrons involved in the rate determining step. For a multi-electron, multi-step reaction, n does not equal the total electrons involved in the whole reaction. For example, the ORR involves a total of 4 electrons. However, the apparent electron number changes with the Tafel slope. At the low current density range (low overpotential), a Tafel slope of 60 mV/dec has been observed, indicating that the apparent electron number in the rate determining step is 2.

1.3.2.5 Tafel Equation – Simplified Activation Kinetics

At high overpotential, one term in the Butler-Volmer equation can be ignored and the equation can be simplified. For the forward reaction,

$$i = i_0 \exp\left(\frac{-\alpha nF\eta}{RT}\right) \quad (1.89)$$

For the backward reaction,

$$i = -i_0 \exp\left(\frac{(1-\alpha)nF\eta}{RT}\right) \quad (1.90)$$

Rearrangement of the two equations gives the forward reaction as

$$\eta = \frac{RT}{\alpha nF} \ln i_0 - \frac{RT}{\alpha nF} \ln i \quad (1.91)$$

$$\eta = \frac{2.303RT}{\alpha nF} \log i_0 - \frac{2.303RT}{\alpha nF} \log i \quad (1.92)$$

Assuming

$$a = \frac{2.303RT}{\alpha nF} \log i_0 \quad (1.93)$$

$$b = -\frac{2.303RT}{\alpha nF} \quad (1.94)$$

then Equation 1.92 is simplified as

$$\eta = a + b \log i \quad (1.95)$$

At 25 °C, $a = \frac{0.059}{\alpha n} \log i_0$, and $b = -\frac{0.059}{\alpha n}$. Equation 1.95 is the well-known Tafel equation, which tells us that in a certain current density range, overpotential is linearly dependent on the logarithm of current density. The exchange current density can be obtained from the intercept at the current density axis. The slope of the line is called the Tafel slope. The higher the Tafel slope, the slower the reaction kinetics.

For the backward reaction,

$$\eta = -\frac{RT}{(1-\alpha)nF} \ln i_0 + \frac{RT}{(1-\alpha)nF} \ln(-i) \quad (1.96)$$

$$\eta = -\frac{2.303RT}{(1-\alpha)nF} \log i_0 + \frac{2.303RT}{(1-\alpha)nF} \log(-i) \quad (1.97)$$

Assuming

$$a = -\frac{2.303RT}{(1-\alpha)nF} \log i_0 \quad (1.98)$$

$$b = \frac{2.303RT}{(1-\alpha)nF} \quad (1.99)$$

then for the backward reaction we also have

$$\eta = a + b \log(-i) \quad (1.100)$$

The values of $-\frac{2.303RT}{\alpha nF}$ and $\frac{2.303RT}{(1-\alpha)nF}$ are the Tafel slopes for the forward and backward reactions, respectively.

Now we can apply the Tafel equation to fuel cell electrode reactions. As the overpotential at the anode is positive ($\eta_a > 0$), the first term in Equation 1.83 is negligible. Equation 1.83 can be simplified as

$$i_a = -i_{0,H_2} \exp\left(\frac{(1-\alpha_H)n_{\alpha,H}F\eta_a}{RT}\right) \quad (1.101)$$

Similarly, as the overpotential at the cathode is negative ($\eta_c < 0$), Equation 1.84 can be simplified as

$$i_c = i_{0,O_2} \exp\left(\frac{-\alpha_O n_{\alpha,O} F \eta_c}{RT}\right) \quad (1.102)$$

Their Tafel forms are therefore written as follows:

$$\eta_a = -\frac{2.303RT}{(1-\alpha_H)n_{\alpha,H}F} \log i_{0,H_2} + \frac{2.303RT}{(1-\alpha_H)n_{\alpha,H}F} \log(-i_a) \quad (1.103)$$

$$\eta_c = \frac{2.303RT}{\alpha_O n_{\alpha,O} F} \log i_{0,O_2} - \frac{2.303RT}{\alpha_O n_{\alpha,O} F} \log i_c \quad (1.104]$$

1.3.3 Mass Transfer

Transport processes are involved when a current is passed through a fuel cell. Ions and neutral species that participate in the electrochemical reactions at the anode or cathode have to be transported to the respective electrode surfaces. In Section 1.3.2, we introduced the charge transfer kinetics-controlled electrode reactions in

which the rates of mass transfer processes are very rapid compared to those of all associated chemical reactions. The Tafel characteristic is representative of an irreversible electrode reaction in which the exchange current density is very small. Another case is the mass transfer-controlled reactions in which the rates of all associated chemical reactions are very rapid compared to those of the mass transfer processes.

1.3.3.1 Fast-Speed Electrode Reaction

Rearrangement of Equation 1.81 gives

$$\frac{i}{i_0} = \frac{C_{Ox}}{C_{Ox}^b} \exp\left(\frac{-\alpha nF\eta}{RT}\right) - \frac{C_{Rd}}{C_{Rd}^b} \exp\left(\frac{(1-\alpha)nF\eta}{RT}\right) \quad (1.105)$$

When the exchange current density is very large compared with the electrode reaction current density, that is, $i_0 \gg i$, the left side of Equation 1.105 is approximately equal to zero. Then Equation 1.105 can be written as

$$\frac{C_{Ox}}{C_{Rd}} = \frac{C_{Ox}^b}{C_{Rd}^b} \exp\left(\frac{nF(E - E_{eq})}{RT}\right) \quad (1.106)$$

Based on the Nernst equation,

$$E_{eq} = E_{eq}^0 + \frac{RT}{nF} \ln \frac{C_{Ox}^b}{C_{Rd}^b} \quad (1.107)$$

That is,

$$\frac{C_{Ox}^b}{C_{Rd}^b} = \exp\left[\frac{nF(E_{eq} - E_{eq}^0)}{RT}\right] \quad (1.108)$$

We obtain

$$E = E_{eq}^0 + \frac{RT}{nF} \ln \frac{C_{Ox}}{C_{Rd}} \quad (1.109)$$

Equation 1.109 has the same form as the Nernst equation. It indicates that the surface concentrations of species involved in the Faradaic process are related to the electrode potential by an equation of the Nernst form when the exchange current density is very large. Such electrode reactions are often called reversible or Nernstian, because the principal species obey thermodynamic relationships at the electrode surface.

1.3.3.2 Modes of Mass Transfer

For a reversible electrode reaction, the electrode potential is related to the surface concentrations of species by the Nernst equation. The net rate of the electrode reaction, v_{net} , is then governed completely by the rate at which the electroactive species is brought to the surface by mass transfer, v_{mt} . Hence,

$$v_{net} = v_{mt} = \frac{i}{nF} \quad (1.110)$$

There are three modes of mass transfer, which plays an important role in electrochemical dynamics.

1. Migration: movement of a charged body under the influence of an electric field (a gradient of electrical potential).
2. Diffusion: movement of a species under the influence of a gradient of chemical potential (i.e., a concentration gradient).
3. Convection: stirring or hydrodynamic transport. Generally fluid flow occurs because of natural convection (convection caused by density gradients) and forced convection, and may be characterized by stagnant regions, laminar flow, and turbulent flow.

Mass transfer to an electrode is governed by the Nernst-Planck equation, written for one-dimensional mass transfer along the x -axis as

$$J_i = -D_i \nabla C_i - \frac{Z_i F}{RT} D_i C_i \nabla \phi + C_i v \quad (1.111)$$

where J_i is the flux of species i (mols⁻¹ cm⁻²) at distance x from the surface, D_i is the diffusion coefficient (cm²s), ∇ is a vector operator, C_i is the concentration, ϕ is the electrical potential, Z_i is the charge number, v is the velocity of the solution, and F is the Faraday constant. The three terms on the right-hand side represent the contributions of diffusion, migration, and convection, respectively, to the flux. A rigorous solution is generally not very easy when all three forms of mass transfer are in effect; hence electrochemical systems are frequently designed so that one or more of the contributions to mass transfer are negligible. For example, the migrational component can be reduced to negligible levels by the addition of an inert electrolyte (a supporting electrolyte) at a concentration much larger than that of the electroactive species. Convection can be avoided by preventing stirring and vibrations in the electrochemical cell.

1.3.3.3 Semi-Empirical Treatment of Steady-State Mass Transfer

For the cathode reaction of a reversible electrode reaction (Reaction 1.64), without considering migration and convection, the electrode reaction rate equals the diffusion rate of O_x at the electrode surface:

$$v_{mt} = -D_{Ox} \left(\frac{\partial C_{Ox}(x)}{\partial x} \right)_{x=0} \quad (1.112)$$

Under the condition of steady-state diffusion, we assume that the diffusion distance is δ . Equation 1.112 turns out to be

$$v_{mt} = D_{Ox} \frac{C_{Ox}^b - C_{Ox}}{\delta} \quad (1.113)$$

where C_{Ox} is the surface concentration of O_x . Then we have,

$$\frac{i}{nF} = D_{Ox} \frac{C_{Ox}^b - C_{Ox}}{\delta} \quad (1.114)$$

Obviously, if $C_{Ox} = 0$ or $C_{Ox} \ll C_{Ox}^b$,

$$\frac{i_l^f}{nF} = \frac{D_{Ox} C_{Ox}^b}{\delta} \quad (1.115)$$

where i_l^f is the forward limiting current density. Equation 1.114 can be transformed to

$$i = \frac{nFD_{Ox}}{\delta} C_{Ox}^b \left(1 - \frac{C_{Ox}}{C_{Ox}^b} \right) \quad (1.116)$$

Then,

$$\frac{C_{Ox}}{C_{Ox}^b} = 1 - \frac{i}{i_l^f} \quad (1.117)$$

Similarly,

$$\frac{C_{Rd}}{C_{Rd}^b} = 1 - \frac{i}{i_l^b} \quad (1.118)$$

where i_l^b is the backward limiting current density.

1.3.3.4 Effect of Mass Transfer on Voltage-Current Relationship

Substitution of the expressions in Equations 1.117 and 1.118 into 1.81 yields

$$i = i_0 \left[\left(1 - \frac{i}{i_f^f}\right) \exp\left(\frac{-\alpha n F \eta}{RT}\right) - \left(1 - \frac{i}{i_f^b}\right) \exp\left(\frac{(1-\alpha)n F \eta}{RT}\right) \right] \quad (1.119)$$

Equation 1.119 is the $i - \eta$ relationship including the effect of mass transfer.

When the overpotential is very small, that is, $\left| \frac{n F \eta}{RT} \right| \ll 1$,

$$\exp\left(\frac{-\alpha n F \eta}{RT}\right) \approx 1 - \frac{\alpha n F \eta}{RT} \quad (1.120)$$

$$\exp\left(\frac{(1-\alpha)n F \eta}{RT}\right) \approx 1 + \frac{(1-\alpha)n F \eta}{RT} \quad (1.121)$$

These two expressions combine with Equation 1.119 to yield

$$i = i_0 \left[\left(1 - \frac{i}{i_f^f}\right) \left(1 - \frac{\alpha n F \eta}{RT}\right) - \left(1 - \frac{i}{i_f^b}\right) \left(1 + \frac{(1-\alpha)n F \eta}{RT}\right) \right] \quad (1.122)$$

When the overpotential is very small, we also have $i/i_f^f \ll 1$, and $i/i_f^b \ll 1$.

Then $\frac{i}{i_f^f} \left(\frac{\alpha n F \eta}{RT}\right)$ and $\frac{i}{i_f^b} \left(\frac{(1-\alpha)n F \eta}{RT}\right)$ are negligible and Equation 1.122 becomes

$$\frac{i}{i_0} = -\frac{i}{i_f^f} + \frac{i}{i_f^b} - \frac{n F \eta}{RT} \quad (1.123)$$

or

$$\eta = -i \left(\frac{RT}{n F i_0} + \frac{RT}{n F i_f^f} - \frac{RT}{n F i_f^b} \right) \quad (1.124)$$

Previously we defined $\frac{RT}{n F i_0}$ as the charge transfer resistance (see Equation 1.88). Similarly, $\frac{RT}{n F i_f^f}$ and $\frac{RT}{n F i_f^b}$ have the same unit as $\frac{RT}{n F i_0}$. So they are defined as the mass transfer resistance, $R_{m,c}$ and $R_{m,a}$, respectively; that is,

$$R_{m,f} = \frac{RT}{n F i_f^f} \quad (1.125)$$

$$R_{mt,b} = -\frac{RT}{nF\hat{i}_l^b} \quad (1.126)$$

Therefore, Equation 1.124 can be written as

$$\eta = -i(R_{ct} + R_{mt,f} + R_{mt,b}) \quad (1.127)$$

Obviously, when i_0 is very large, we have

$$R_{ct} \ll R_{mt,f} + R_{mt,b} \quad (1.128)$$

and when i_0 is very small, we have

$$R_{ct} \gg R_{mt,f} + R_{mt,b} \quad (1.129)$$

Note that the equations derived in this section apply when the overpotential is small. Therefore, Equations 1.128 and 1.129 indicate that near the equilibrium electrode potential, the overpotential is controlled by the mass transfer when i_0 is very large. On the contrary, near the equilibrium electrode potential, the overpotential is controlled by the charge transfer when i_0 is very small.

1.3.4 Multiple Kinetics

1.3.4.1 Electrode Kinetic and Mass Transfer for Fuel Cell Reactions

For the reaction occurring inside a porous three-dimensional catalyst layer, a thin-film flooded agglomerate model has been developed [149, 150] to describe the potential-current behavior as a function of reaction kinetics and reactant diffusion. For simplicity, if the kinetic parameters, such as the exchange current density and diffusion limiting current density, can be defined as apparent parameters, the corresponding Butler-Volmer and mass diffusion relationships can be obtained [134]. For an H_2 /air (O_2) fuel cell, considering both the electrode kinetic and the mass transfer, the $i-\eta$ relationships of the fuel cell electrode reactions within the catalyst layer can be expressed as Equations 1.130 and 1.131, respectively, based on Equation 1.122. The $i-\eta$ relationship of the catalyzed cathode reaction within the catalyst layer is

$$i_c = i_{0,O_2} \left[\left(1 - \frac{i_c}{i_{l,O}^f}\right) \exp\left(\frac{-\alpha_O n_{\alpha,O} F \eta_c}{RT}\right) - \left(1 - \frac{i_c}{i_{l,O}^b}\right) \exp\left(\frac{(1-\alpha_O) n_{\alpha,O} F \eta_c}{RT}\right) \right] \quad (1.130)$$

and the corresponding $i-\eta$ relationship of the anode reaction is

$$i_a = i_{0,H_2} \left[\left(1 - \frac{i_a}{i_{1,H}^f}\right) \exp\left(\frac{-\alpha_H n_{\alpha,H} F \eta_a}{RT}\right) - \left(1 - \frac{i_a}{i_{1,H}^b}\right) \exp\left(\frac{(1-\alpha_H) n_{\alpha,H} F \eta_a}{RT}\right) \right] \quad (1.131)$$

where R is the gas constant ($8.314 \text{ Jmol}^{-1}\text{K}^{-1}$) and T is the temperature (K). i_c and i_a are the cathode and anode current densities, respectively. i_{0,O_2} and i_{0,H_2} are the apparent exchange current densities for cathodic O_2 reduction and anodic H_2 oxidation reactions, respectively. $i_{1,O}^f$ and $i_{1,O}^b$ are the apparent diffusion limiting current densities for the cathodic forward and reverse reactions, respectively, and $i_{1,H}^f$ and $i_{1,H}^b$ are the corresponding apparent diffusion limiting current densities for anode reactions. It is assumed that these six apparent current densities are all a function of the morphology and structure of the three-dimensional catalyst layer matrix [151]. η_c and η_a in Equations 1.130 and 1.131 are the cathodic and anodic overpotentials, respectively. η_c can be expressed as $E_c - E_c^{eq}$, and η_a can be expressed as $E_a - E_a^{eq}$, where E_c^{eq} and E_a^{eq} are the thermodynamic electrode potentials (or reversible electrode potentials) for cathodic O_2 reduction and anodic H_2 oxidation, respectively. $n_{\alpha O}$ and $n_{\alpha H}$ in Equations 1.130 and 1.131 are the electron transfer numbers in the rate determining steps for the cathodic O_2 reduction and anodic H_2 oxidation reactions, respectively.

1.3.4.2 Low Current Density

In the low current density range, the contribution of mass transfer polarization is negligible and the electrode charge transfer and membrane resistance polarization are significant. In this case, Equations 1.130 and 1.131 can be simplified into Equations 1.132 and 1.133, respectively.

$$i_c = i_{0,O_2} \left[\exp\left(\frac{-\alpha_O n_{\alpha,O} F \eta_c}{RT}\right) - \exp\left(\frac{(1-\alpha_O) n_{\alpha,O} F \eta_c}{RT}\right) \right] \quad (1.132)$$

$$i_a = i_{0,H_2} \left[\exp\left(\frac{-\alpha_H n_{\alpha,H} F \eta_a}{RT}\right) - \exp\left(\frac{(1-\alpha_H) n_{\alpha,H} F \eta_a}{RT}\right) \right] \quad (1.133)$$

From the AC impedance spectra, the exchange current density of the ORR can be calculated from the charge transfer resistance. In the low current density range ($< 0.4 \text{ A/cm}^2$, the Pt catalyst surface will be covered partially by a PtO layer with surface coverage of approximately 0.3 [125, 152, 153], the numerical relationship between η_c and i_c can thus be obtained.

1.3.4.3 High Current Density

In the high current density range ($> 0.4 \text{ A/cm}^2$, the catalyst surface will be covered with pure Pt [154, 155]), the diffusion-related terms in Equations 1.130 and 1.131 must be considered. As a result, at high overpotentials (both η_c and η_a are large),

the second terms will be insignificant compared to the first terms, suggesting that the second terms are negligible. Therefore, Equations 1.130 and 1.131 can be simplified as Equations 1.134 and 1.135, respectively:

$$i_c = i_{0,O_2} \left[\left(1 - \frac{i_c}{i_{i,O}^f} \right) \exp\left(\frac{-\alpha_O n_{\alpha,O} F \eta_c}{RT}\right) \right] \quad (1.134)$$

$$i_a = -i_{0,H_2} \left(1 - \frac{i_a}{i_{i,H}^b} \right) \exp\left(\frac{(1-\alpha_H) n_{\alpha,H} F \eta_a}{RT}\right) \quad (1.135)$$

1.3.5 Polarization Curve and Voltage Losses

1.3.5.1 Polarization

When the fuel cell operates, the actual voltage of the cell is less than the value of the OCV. Cell voltage is the actual voltage of the fuel cell and the current density, i , is the cell current, I , per cell active area, A .

$$i = \frac{I}{A} \quad (1.136)$$

The cell current is equal to the stack current because the stack is formed by connecting the individual cells in series.

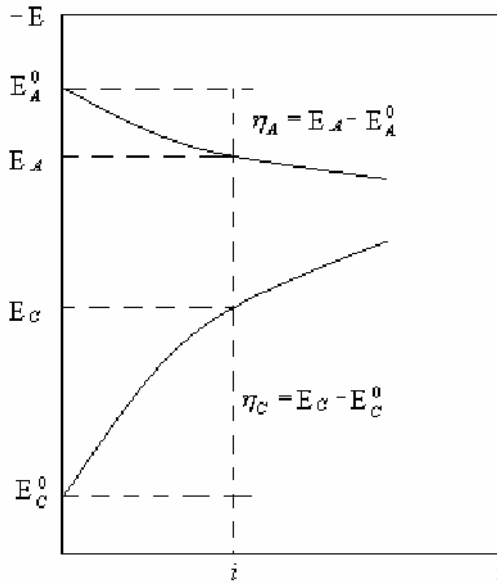


Figure 1.26. A schematic plot of electrode polarization and voltage drop

Once the fuel cell circuit is connected, there is a current flow, which causes the electrode to be polarized. This means that the anode electrode potential will move to a more positive value, and the cathode electrode potential will move to a more negative value, resulting in a decrease in the cell voltage, which is known as the voltage loss. The principle is shown in Figure 1.26.

1.3.5.2 Polarization Curve

A plot of cell potential against current density under a set of constant operating conditions, known as a polarization curve, is the standard electrochemical technique for characterizing the performance of fuel cells (both single cells and stacks) [156]. It yields information on the performance losses in the cell or stack under operating conditions. A steady-state polarization curve can be obtained by recording the current as a function of cell potential or recording the cell potential as the cell current changes. A non-steady-state polarization curve can be obtained using a rapid current sweep [157]. By measuring polarization curves, certain parameters such as the effects of the composition, flow rate, temperature, and RH of the reactant gases on cell performance can be characterized and compared systematically. A sample polarization curve is shown in Figure 1.27. Very often, polarization curves are converted to power density versus current density plots by multiplying the potential by the current density at each point of the curve, also seen in Figure 1.27.

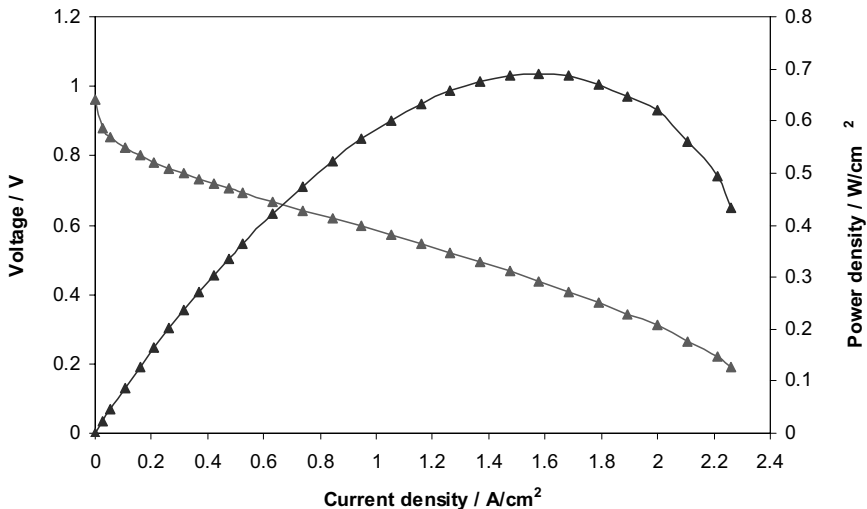


Figure 1.27. A sample fuel cell polarization curve obtained from the diagnostic modeling PEM fuel cell with an active area of 192 cm², designed by NRC-IFCI

Polarization curves provide information on the performance of the cell or stack as a whole. While they are useful indicators of overall performance under specific operating conditions, they fail to produce much information about the performance of individual components within the cell. They cannot be obtained during normal operation of a fuel cell and take significant time. In addition, they fail to

differentiate different mechanisms; for example, flooding and drying inside a fuel cell cannot be distinguished in a single polarization curve. They are also incapable of resolving time-dependent processes occurring in the fuel cell and the stack. For the latter purpose, current interrupt, EIS measurements, and other electrochemical approaches are preferred. These techniques will be introduced in the following sections.

1.3.5.3 Voltage Loss

The fuel cell voltage losses are classified into three categories: the activation loss (activation polarization), the ohmic loss (ohmic polarization), and the concentration loss (concentration polarization). Plots of voltage drops caused by each of the losses are shown in Figure 1.28. At low current densities (the region of activation polarization), the cell potential drops sharply and the majority of these losses are due to the sluggish kinetics of the ORR [1]. At intermediate current densities (the region of ohmic polarization), the voltage loss caused by ohmic resistance becomes significant and results mainly from resistance to the flow of ions in the electrolyte and resistance to the flow of electrons through the electrode [158]. In this region, the cell potential decreases nearly linearly with current density, while the activation overpotential reaches a relatively constant value [1]. At high current densities (the region of concentration polarization), mass transport effects dominate due to the transport limit of the reactant gas through the pore structure of the GDLs and electrocatalyst layers, and cell performance drops drastically [159].

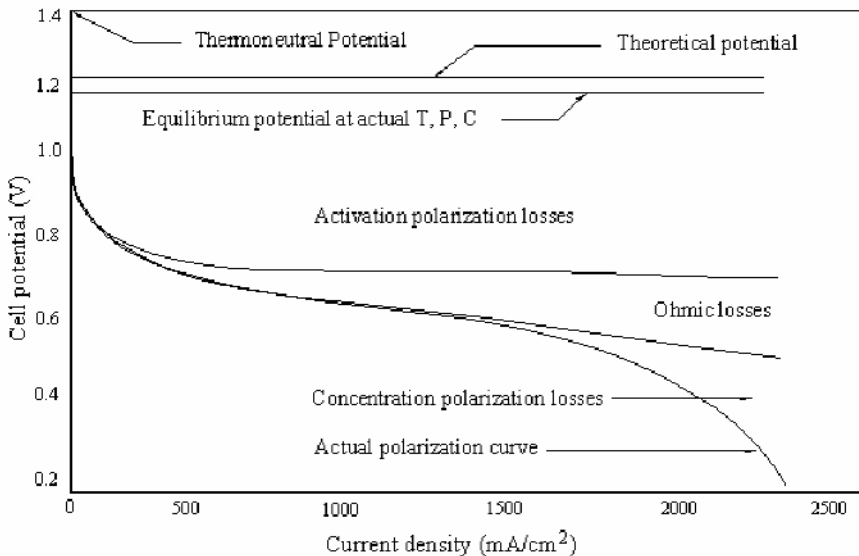


Figure 1.28. Schematic of an ideal polarization curve with the corresponding regions and overpotentials [1]. (Reprinted from Barbir F. PEM fuel cells: theory and practice. New York: Elsevier Academic Press, ©2005, with permission from Elsevier.)

The output voltage of a single cell, E_{cell} , can be defined as follows:

$$E_{cell} = E_{OCV} - \Delta E_{act} - \Delta E_{ohmic} - \Delta E_{con} \quad (1.137)$$

where E_{cell} is the voltage for a certain operating condition, E_{OCV} represents the fuel cell OCV, ΔE_{act} is the voltage drop associated with the activation of the anode and of the cathode, ΔE_{ohmic} is the ohmic voltage drop associated with the conduction of protons and electrons, and ΔE_{con} is the voltage drop resulting from the decrease in the concentration of oxygen and hydrogen. Each of these losses is discussed separately in the following sections.

Activation Loss

Activation overvoltage or activation loss is caused by activation polarization, which arises from the need to move electrons and to break and form chemical bonds in both the anode and the cathode.

$$\Delta E_{act} = |\eta_a| + |\eta_c| \quad (1.138)$$

In low- and medium-temperature fuel cells, activation overvoltage is the most important irreversibility and cause of voltage drop. The relation between activation overvoltage and current density is described by the Tafel equation, e.g.,

$$\eta_c = a + b \log i \quad (1.139)$$

Therefore, based on Equations 1.103 and 1.104, the activation loss can be expressed as

$$\begin{aligned} \Delta V_{act} = & \left[-\frac{2.303RT}{(1-\alpha_H)n_{\alpha,H}F} \log i_{0,H_2} + \frac{2.303RT}{(1-\alpha_H)n_{\alpha,H}F} \log i \right] \\ & + \left[-\frac{2.303RT}{\alpha_O n_{\alpha,O} F} \log i_{0,O_2} + \frac{2.303RT}{\alpha_O n_{\alpha,O} F} \log i \right] \end{aligned} \quad (1.140)$$

This is simplified as

$$\Delta V_{act} = A_c \ln\left(\frac{i}{i_{0,O_2}}\right) + A_a \ln\left(\frac{i}{i_{0,H_2}}\right) \quad (1.141)$$

where $A_c = \frac{RT}{\alpha_O n_{\alpha,O} F}$ and $A_a = \frac{RT}{(1-\alpha_H)n_{\alpha,H} F}$.

As the reaction of hydrogen oxidation at the anode is much faster than that of oxygen reduction at the cathode the voltage drop due to the activation loss is

dominated by the cathode reaction, and activation overvoltage occurs mainly at the cathode.

Then, Equation 1.140 is simplified as

$$\Delta V_{act} = -\frac{2.303RT}{\alpha_O n_{a,O} F} \log i_{0,O_2} + \frac{2.303RT}{\alpha_O n_{a,O} F} \log i \quad (1.142)$$

or

$$\Delta V_{act} = A_c \ln\left(\frac{i}{i_{0,O_2}}\right) \quad (1.143)$$

Activation overvoltage at both electrodes is important in cells using fuels other than hydrogen, such as methanol. At higher temperatures and pressures the activation overvoltage becomes less important.

Mass Transport or Concentration Loss

Concentration polarization will cause concentration loss or concentration overvoltage, which arises from the drop in concentration of the reactants as they are consumed in the reaction. This concentration loss can cause rapid voltage drop at high current density. As the concentration loss or voltage drop is composed of concentration polarization on the anode and the cathode, the total concentration loss is expressed as

$$\Delta E_{con} = \Delta E_{con,c} + \Delta E_{con,a} \quad (1.144)$$

According to the Nernst equation, we have

$$\Delta E = \frac{RT}{nF} \ln\left(\frac{C_{Ox}^b}{C_{Ox}}\right) \quad (1.145)$$

By combining Equations 1.145, 1.114, and 1.115, a relationship for voltage loss due to concentration polarization is obtained:

$$\Delta E_{con,c} = \frac{RT}{nF} \ln\left(\frac{i_{l,c}}{i_{l,c} - i}\right) \quad (1.146)$$

Similarly, we have

$$\Delta E_{con,a} = \frac{RT}{nF} \ln\left(\frac{i_{l,a}}{i_{l,a} - i}\right) \quad (1.147)$$

Therefore, the total concentration loss is written as

$$\Delta E_{con} = \frac{RT}{nF} \ln\left(\frac{i_{l,c}}{i_{l,c} - i}\right) + \frac{RT}{nF} \ln\left(\frac{i_{l,a}}{i_{l,a} - i}\right) \quad (1.148)$$

Ohmic Loss

Ohmic loss is the simplest voltage loss to understand. Ohmic loss or ohmic overvoltage is caused by ohmic polarization, which arises from the resistance of the polymer membrane to the transfer of ions and the resistance of the electrode and the collector plate to the transfer of electrons.

The voltage drop related to the ohmic polarization is described by Ohm's law,

$$\Delta E_{ohm} = iR_{ohm} \quad (1.149)$$

where R_{ohm} (Ωcm^2) is the internal electrical resistance, which includes ionic, electronic, and contact resistances. In most fuel cells, electronic resistance is almost negligible, even when graphite or graphite/polymer composites are used as current collectors, and the resistance is caused primarily by the electrolyte (ionic), though the contact resistances can also be important. Generally, it is possible to distinguish this particular voltage loss from other voltage losses through techniques like AC impedance and current interruption.

Summary

There is another voltage loss, which is caused by fuel crossover and internal currents. Basically, fuel crossover and internal currents have very marked effects on the OCV, E_{OCV} . For more information on this voltage loss, please see Section 1.2.4.

To summarize, the cell potential is equal to the open circuit potential reduced by the potential loss or voltage drop [1]:

$$E_{cell} = E_{OCV} - E_{loss} \quad (1.150)$$

where the voltage drop is composed of activation and concentration polarization losses on both the anode and the cathode and of ohmic losses,

$$E_{loss} = (\Delta E_{act} + \Delta E_{con})_a + (\Delta E_{act} + \Delta E_{con})_c + \Delta E_{Ohmic} \quad (1.151)$$

and the actual OCV is expressed as

$$E_{OCV} = E_{theor}^{OCV} - E_{cross} - E_{mix} \quad (1.152)$$

A theoretical OCV can be obtained as described in Section 1.2.4.1:

$$E_{theor}^{OCV} = 1.229 - 0.000846(T - 298.15) + \frac{RT}{4F} \ln[P_{O_2} (P_{H_2})^2] \quad (1.153)$$

1.3.5.4 Empirical Equations for the Polarization Curves

So far, numerous modeling studies have been carried out to elucidate the electrochemical behavior of PEM fuel cells, and for this purpose, many empirical equations have been introduced to mimic the polarization curves. Srinivasan et al. [160, 161] developed the following equation to describe the relation between the cell voltage, E , and current density, i , in the low and intermediate current density ranges, where the electrochemical reaction is controlled by the activation and ohmic losses:

$$E = E_0 - b \log(i) - Ri \quad (1.154)$$

where $E_0 = E_r + b \log i_0$ and the two subsequent terms describe the different loss mechanisms. E_r is the reversible potential of the cell, and i_0 and b are the exchange current density and the Tafel slope for oxygen reduction, respectively. The second term in Equation 1.154 is predominant at low current densities and describes the activation overpotential. In the third term, R represents the resistance that causes a linear variation of the cell potential with the current density, which is predominant in the intermediate current density region.

Kim et al. [162] modified Equation 1.154 by introducing an additional term in order to fit the cell voltage against current density behavior over the whole current density range:

$$E = E_0 - b \log(i) - Ri - m \exp(ni) \quad (1.155)$$

where m and n are the parameters related to mass transport limitation. Bevers et al. [163] found in their one-dimensional model that m correlates to the electrolyte conductivity and n to the porosity of the GDL. In the high current density region the last term becomes predominant, and is used to match the losses due to the mass transport limitations.

Lee et al. [164] took into account the influence of pressure parameters on the concentration polarization in PEM fuel cell stack models,

$$E = E_0 - b \log(i) - Ri - m \exp(ni) - a \log\left(\frac{P}{P_{O_2}}\right) \quad (1.156)$$

where P is the total pressure, P_{O_2} is the partial pressure of oxygen, and a is an empirical equation constant.

Squadrito et al. [165] developed a logarithmic equation based on a mechanistic analysis in order to find an expression for the concentration polarization, which was then modified to fit a set of experimental data:

$$E = E_0 - b \log(i) - Ri + \alpha i^k \ln(1 - \beta i) \quad (1.157)$$

where the term αi^k accounts for the pre-logarithmic terms attributed to the different contributions and acts as an “amplification term,” expressed in potential units; k is a dimensionless number; β is the inverse of the limiting current density; and α is the transfer coefficient. Squadrito et al. further claimed that Equation 1.157 is able to predict a more accurate behavior at high current densities since k influences primarily the point at which there is departure from the linear behavior, and α determines the shape of the curve at high current densities.

The non-linear contributions to the cell potential drop at high current densities result from interface phenomena occurring in the cathode reactive region. Pisani et al. [166] developed a semi-empirical equation, based on the integral of the oxygen concentration over the reactive region,

$$E = E_0 - b \ln(i) - Ri + a \ln \left(1 - \frac{i}{i_l} S^{-\mu(1-i/i_l)} \right) \quad (1.158)$$

where S is a flooding parameter, μ is an empirical constant, and i_l is the limiting current density.

More complex empirical equations based on Equation 1.155 have also been developed. For example, Amphlett et al. [167] presented empirical equations and terms that relate activation losses, internal resistance, and all temperature dependencies through fitting parameters. Sena et al. [168] analyzed the catalyst layer and considered it as a thin-film flooded agglomerate; thus, the GDE is assumed to be formed by an assembly of flooded zones (catalytic zones) and empty zones (no catalyst present). The final equation relates the oxygen diffusion effects in the GDE:

$$E = E_0 - b \log(i) - Ri + b \log \left(1 - \frac{i}{i_L^{O_2}} \right) \quad (1.159)$$

where $i_L^{O_2}$ is the limiting current density due to a limiting oxygen diffusion effect.

1.3.5.5 Distinguishing the Voltage Losses

Current Interruption

In general, the current interruption method is used to measure the ohmic losses in a PEM fuel cell. The principle of the technique is that the ohmic losses vanish much faster than the electrochemical overpotentials when the current is interrupted, as shown in Figure 1.29. It is shown that the ohmic losses disappear almost immediately and the electrochemical (or activation) overpotentials decline to the OCV at a considerably slower rate. Therefore, rapid acquisition of the voltage transient data is of vital importance to adequate separation of the ohmic and activation losses.

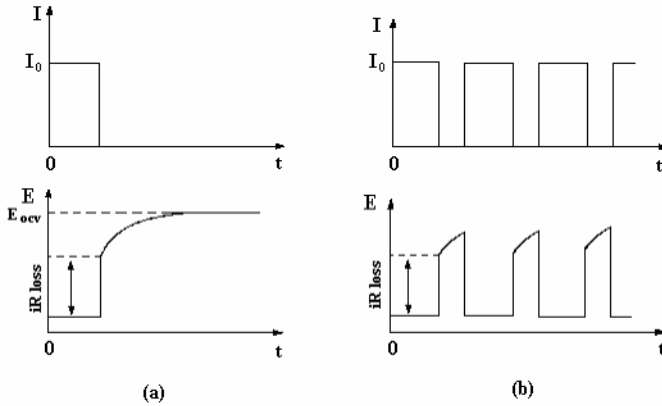


Figure 1.29. An ideal voltage transient in a fuel cell after current interruption, (a) single interruption technique, (b) periodic interruption technique

The crucial issue in measuring *in situ* ohmic losses is to separate the above two processes [169]. Many attempts using this method have been made to determine the ohmic resistances in single cells or individual cells of a PEM fuel cell stack. For example, Mennola et al. [170] have employed this method to determine the ohmic resistances in individual cells of a PEM fuel cell stack. Figure 1.30 shows one of their results. It was achieved by producing voltage transients and monitoring them with a digital oscilloscope connected in parallel with the individual cell. Their results show good agreement between the ohmic losses in the entire stack and the sum of the ohmic losses in each individual cell

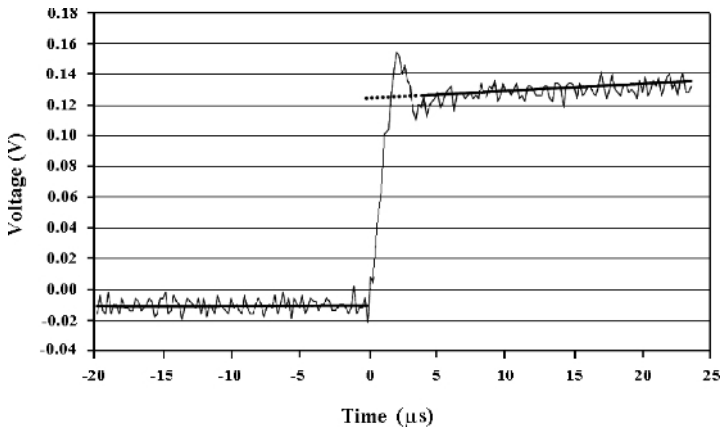


Figure 1.30. Voltage transient (thin line) and fitted average voltage (bold line) for the whole stack. Extrapolation is indicated with a dotted line. Air supply: free convection; $i = 200 \text{ mA cm}^{-2}$ 171. (Reprinted from Journal of Power Sources, 112(1), Mennola Tuomas, Mikkola Mikko, Noponen Matti, Hottinen Tero and Lund Peter, Measurement of ohmic voltage losses in individual cells of a PEMFC stack, 261–72, ©2002, with permission from Elsevier.)

Compared to other methods, the current interrupt method has the advantage of relatively straightforward data analysis. However, one of the weaknesses of this method is that the information obtained for a single cell or stack is limited. Another issue with this method is the difficulty in determining the exact point at which the voltage jumps instantaneously; thus, a fast oscilloscope should be used to record the voltage changes.

AC Impedance

AC impedance, also known as EIS, applies a small AC voltage or current perturbation/signal to the cell and the amplitude and phase of the resulting signal are measured as a function of frequency. This may be repeated through a wide range of frequencies. Basically, impedance is a measure of the ability of a system to impede the flow of electrical current; thus, EIS is a powerful technique that can resolve various sources of polarization loss in a short time and has been widely applied to PEM fuel cells.

Impedance spectra are conventionally plotted in both Bode and Nyquist form. In a Bode plot, the amplitude and phase of the impedance are plotted as a function of frequency, while in a Nyquist plot the imaginary part of the impedance is plotted against the real part at each frequency. Figure 1.31 shows the typical EIS spectra in Nyquist form with two arcs, where the frequency increases from the right to the left. The simple form of the equivalent circuit for the spectra in Figure 1.31 is depicted in Figure 1.32. The high-frequency intercept is related to the ohmic resistance of the stack, R_{Ω} , which can be directly compared with the data obtained from current interrupt measurements. The high-frequency arc reflects the combination of the double-layer capacitance in the catalyst layer and the effective charge transfer resistance. The low-frequency arc corresponds to the impedance due to mass transport limitations. The reason for replacing C, the double layer capacitor, by the constant phase element (CPE) results from the fact that the capacitance due to the double-layer charging is distributed along the length of the pores in the porous electrode.

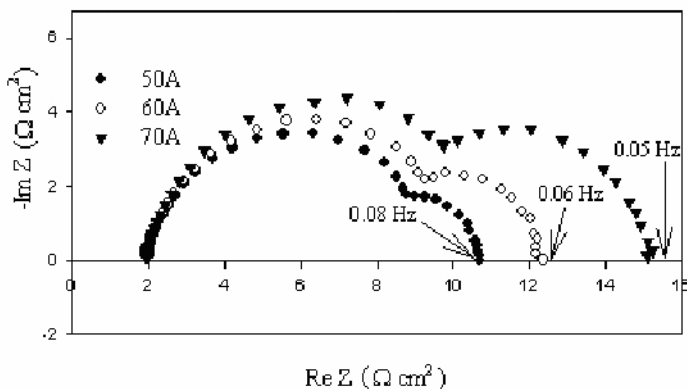


Figure 1.31. Typical impedance spectra of a PEM fuel cell. The spectra were obtained at 30 °C using a Ballard Mark V six-cell stack with an active area of 280 cm².

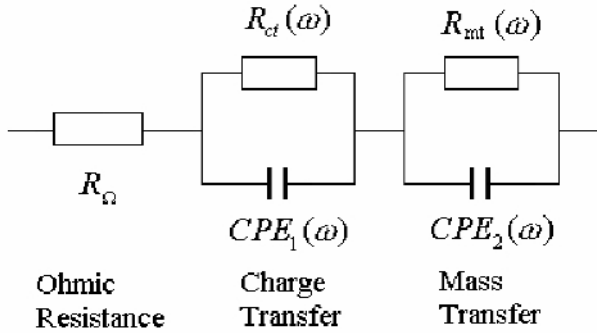


Figure 1.32. Simple equivalent circuit for the spectra in Figure 1.31

The impedance can be measured using various instruments and techniques, ranging from a simple oscilloscope display to a fast Fourier transform analyzer. The most common instrument used is a frequency response analyzer (FRA), such as a Solartron FRA. The AC impedance or FRA is a four-terminal measurement. Figure 1.33 shows a typical electronic connection for an AC impedance measurement between the Solartron 1260 FRA, TDI loadbank (RBL 488 series 100–60–400), and fuel cell.

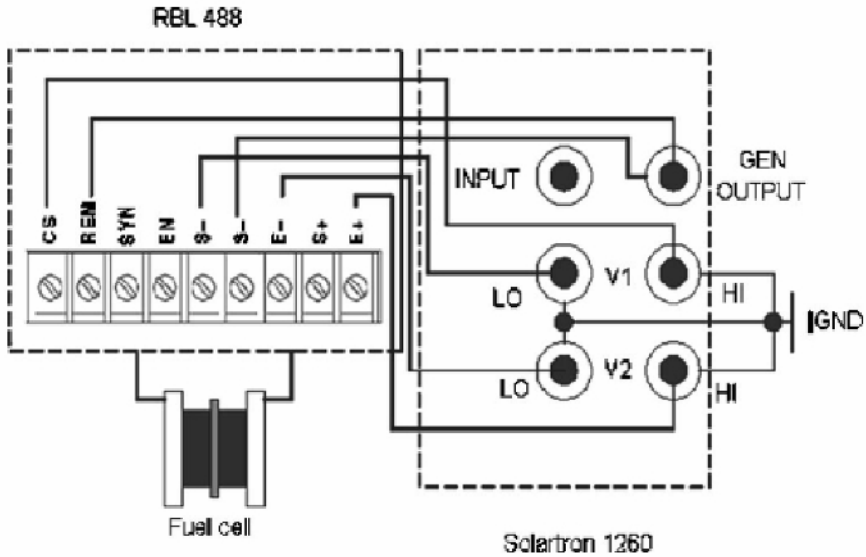


Figure 1.33. Typical electronic connections of AC impedance measurement of a PEM fuel cell [5]. (Reproduced by permission of ECS—The Electrochemical Society, from Tang Y, Zhang J, Song C, Liu H, Zhang J, Wang H, et al. Temperature-dependent performance and *in situ* AC impedance of high-temperature PEM fuel cells using the Nafion-112 membrane.)

The Solartron 1260 FRA can perform flexible signal processing. The TDI loadbank is a single channel loadbank that can be controlled with signals via an external program. When a controlling DC, AC, DC/AC combination, or FRA-generated waveform is connected into the REM and S- ports located on the rear panel of the loadbank, the loadbank will transfer the signal into the fuel cell load level. The values of all signals are referred to as S-. In Tang et al.'s [40] impedance experiments, the differential input with a floating ground was chosen to reduce noise and harmonic signals from externally wired circuits. An oscilloscope was connected to the fuel cell current collectors to monitor the noise level. The results showed that this electronic connection can effectively reduce noise. During the measurements, the FRA port, GEN OUTPUT, gave a software-command signal to the loadbank through the REM and S- ports. The cell voltage response went to FRA V1 and V2 for analysis. The obtained impedance information was sent to a computer for data display and more sophisticated data analysis performed by the powerful software Z-plot.

However, there are still unresolved issues regarding the explanation of the impedance spectra. For example, it is difficult to distinguish the individual contributions from the anode and cathode sides, although it is generally considered that the rapid kinetics and mass transport of the HOR result in a negligible impedance contribution from the anode catalyst layer. In addition, the interpretation of the low-frequency feature can be very sophisticated.

1.3.6 Measures to Improve Cell Performance [26]

1.3.6.1 Reducing the Activation Overvoltage

As described in the previous sections, the exchange current density, i_0 , is a crucial factor in reducing the activation overvoltage. Therefore, the most important step for improving the fuel cell performance is to increase the value of i_0 , especially at the cathode. The increase of i_0 can be achieved in several ways summarized, as follows:

- Raising the cell temperature. For a low-temperature cell, i_0 at the cathode will be about 0.1 mAcm⁻², whereas for a typical 800 °C cell, it will be about 10 mAcm⁻², a 100-fold improvement.
- Using more effective catalysts.
- Increasing the roughness of the electrodes. This increases the real surface area of the electrodes, leading to an increase in i_0 .
- Increasing reactant concentration. This is achieved by greater occupation of reactants on the catalyst sites.
- Increasing the pressure. This is also achieved by increasing catalyst site occupancies.

1.3.6.2 Reducing the Concentration Overvoltage

Reducing the concentration overvoltage can be achieved by enhancing mass transfer through the following ways:

- Increasing reactant concentration by, for example, using pure O₂ instead of air.

- Increasing the gas flow rate or pressure to enhance mass transfer.
- Designing the flow field to help mass transfer through the channels.
- Optimizing the GDL porosity and improving GDL structure.

1.3.6.3 Reducing the Ohmic Overvoltage

There are three main ways of reducing the internal resistance of the cell:

- The use of electrodes with the highest possible conductivity.
- Good design and use of appropriate materials for the bipolar plates or cell interconnects.
- Making the electrolyte as thin as possible. However, this is often difficult because the electrolyte needs to be thick enough to support the electrodes, or it needs to be wide enough to allow a circulating flow of electrolyte.

References

1. Barbir F. PEM fuel cells: theory and practice. New York: Elsevier Academic Press, 2005.
2. Smithsonian Institute [homepage on the Internet]. Washington, DC: National Museum of American History; c1990–2008 [updated 2004]. PEM fuel cells. Available from: <http://americanhistory.si.edu/fuelcells/pem/pemmain.htm>.
3. Wikipedia [updated 18 April 2008]. Proton exchange membrane fuel cells. Available from: http://en.wikipedia.org/wiki/Proton_exchange_membrane_fuel_cell.
4. Ballard Power Systems [homepage on the Internet]. Burnaby, Canada: Ballard Power Systems; c2008 [updated 2008]. Company history. Available from: http://www.ballard.com/About_Ballard/Corporate_Information/Company_History.htm
5. Tang Y, Zhang J, Song C, Liu H, Zhang J, Wang H, et al. Temperature-dependent performance and in situ AC impedance of high-temperature PEM fuel cells using the Nafion-112 membrane. *J Electrochem Soc* 2006;153(11): A2036–43.
6. Martin J, Blanco M, Pazos-Knoop S, Gu E, Wang H, Vanderhoek T, et al. (National Research Council of Canada Institute for Fuel Cell Innovation). Controlled Technical Report. Vancouver (BC) Canada: NRC-IFCI; 2005. Report No.: IFCI-PEMFC-CTR-015.
7. Nguyen TV, Knobbe MW. A liquid water management strategy for PEM fuel cell stacks. *J Power Sources* 2003;114:70–79.
8. Wilkinson D, Vanderleeden O. Handbook of Fuel Cells: Fundamentals, Technology and Applications Vol. 3. In: Vielstich W, Lamm A, Gasteriger HA, editors. Chichester, England: John Wiley and Sons, 2003; 315–36.
9. Mehta V, Cooper JS. Review and analysis of PEM fuel cell design and manufacturing. *J Power Sources* 2003;114:32–53.
10. EG&G Technical Services, Ltd. Fuel cell handbook. Morgantown, West Virginia: U.S. Department of Energy, 2004.
11. Pukrushpan JT, Stefanopoulou AG, Peng H. Control of fuel cell breathing. *IEEE Control Systems Magazine* 2004;24:30–46.
12. Panchenko A. Polymer electrolyte membrane degradation and oxygen reduction in fuel cells: an EPR and DFT investigation. Doctoral thesis, Institute für Phyzikalische Chemie der Universität, Stuttgart, 2004. Available from: <http://elib.uni-stuttgart.de/opus/volltexte/2004/2088/pdf/Panchenko.pdf>.

13. Kadirov MK, Bosnjakovic A, Schlick S. Membrane-derived fluorinated radicals detected by electron spin resonance in UV-irradiated Nafion and Dow ionomers: effect of counterions and H₂O₂. *J Phys Chem B* 2005;109:7664–766.
14. LaConti AB, Hamdan M, McDonald RC. Mechanisms of chemical degradation. In: *Handbook of fuel cells: fundamentals, technology, and applications*, vol. 3. Vielstich W, Lamm A, Gasteiger H, editors. Chichester, England: John Wiley and Sons; 2003;647–62.
15. Hodgdon RB Jr, Enos JF, Aiken EJ. Sulfonated polymers of α, β, β -trifluorostyrene, with applications to structures and cell. US Patent 3 341 366 1967.
16. Hodgdon RB Jr, Enos JF, Aiken EJ. Process of sulfonating poly-alpha, beta, beta-trifluorostyrene. US Patent 3 442 825 1969.
17. D'Agostino VF, Lee JY, Cook EH. Trifluorostyrene sulfonic acid membranes. US Patent 4 012 303 1977.
18. Yu J, Yi B, Xing D, Liu F, Shao Z, Fu Y, Zhang H. Degradation mechanism of polystyrene sulfonic acid membrane and application of its composite membranes in fuel cells. *Phys Chem Chem Phys* 2003;5:611–5.
19. Feldheim DL, Lawson DR, Martin CR. Influence of the sulfonate counteraction on the thermal stability of Nafion perfluorosulfonate membranes. *J Polym Sci Part B: Polym Phys* 1993;31:953–7.
20. Patil YP, Seery TAP, Shaw MT, Parnas RS. In-situ water sensing in a Nafion membrane by fluorescence spectroscopy. *Ind Eng Chem Res* 2005;44:6141–7.
21. Huang C, Tan KS, Lin J, Tan KL. XRD and XPS analysis of the degradation of the polymer electrolyte in H₂-O₂ fuel cell. *Chem Phys Lett* 2003;371:80–5.
22. Hinds G. Performance and durability of PEM fuel cells: a review. Teddington, UK: National Physical Laboratory; 2004. NPL Report No.: DEPC-MPE 002.
23. Bauer B, Jones DJ, Rozière J, Tchicaya L, Alberti G, Casciola M, et al. Electrochemical characterization of sulfonated polyetherketone membranes. *J New Mat Electrochem Systems* 2000;3:93–8.
24. Colliera A, Wang H, Yuan XZ, Zhang J, Wilkinson DP. Degradation of polymer electrolyte membranes. *Intern J Hydrogen Energy* 2006;31:1838–54.
25. Perahia, D. Structure and dynamics of thin ionomer films: a key to a stable fuel cell membrane. American Physical Society Meeting; 2000 March 20–24; Minneapolis, MN. Available from: <http://flux.aps.org/meetings/YR00/MAR00/abs/S4010.html>.
26. Larminie J, Dicks A. *Fuel cell systems explained*. Chichester, England: John Wiley and Sons, 2003.
27. Lee JH, Lalk TR. Modeling fuel cell stack systems. *J Power Sources* 1998;73:229–41.
28. Bever D, Wagner N, VonBradke M. Innovative production procedure for low cost PEFC electrodes and electrode/membrane structures. *Intern J Hydrogen Energy* 1998;23:57–63.
29. Giorgi L, Antolini E, Pozio A, Passalacqua E. Influence of the PTFE content in the diffusion layer of low-Pt loading electrodes for polymer electrolyte fuel cells. *Electrochim Acta* 1998;43:3675–80.
30. Ralph TR, Hards GA, Keating JE, Campbell SA, Wilkinson DP, Davis H, et al. Low-cost electrodes for proton exchange membrane fuel cells. *J Electrochem Sci* 1997;144:3845–57.
31. Itescu, J. *Polymer electrolyte fuel cells: the gas diffusion layer* [monograph on the Internet]. Princeton Institute for the Science and Technology of Materials. Princeton, NJ: Princeton University; 2004. Available from: <http://www.princeton.edu/~pccm/outreach/REU2004/REU-2004-Presentations/JOHANNAH%20ITESCU.pdf>.
32. US Department of Energy [homepage on the Internet]. Parts of a fuel cell. Washington, DC: US Department of Energy; c2008 [last updated 2007 Jan 31]. Hydrogen, fuel cells

- and infrastructure technologies program. Available from: http://www.eere.energy.gov/hydrogenandfuelcells/fuelcells/fc_parts.html.
33. Williams MV, Begg E, Bonville L, Kunz HR, Fenton JM. Characterization of gas diffusion layers for PEMFC. *J Electrochem Soc* 2004;151:A1173–80.
 34. Yuan XZ, Wang HJ, Zhang JJ, Wilkinson D. Bipolar plates for PEM fuel cells – from materials to processing. *J New Mat Electrochem Syst* 2005;8:257–67.
 35. Cooper JS. Design analysis of PEMFC bipolar plates considering stack manufacturing and environment impact. *J Power Sources* 2004;129:152–69.
 36. Davies DP, Adcock PL, Turpin M, Rowen SJ. Stainless steel as a bipolar plate material for solid polymer fuel cells. *J Power Sources* 2000;86:237–42.
 37. Busick D, Wilson M. Development of composite materials for PEFC bipolar plates. *Mat Res Soc Symp Proc* 2000;575:247–51.
 38. Heinzel A, Mahlendorf F, Niemzig O, Kreuz C. Injection moulded low cost bipolar plates for PEM fuel cells. *J Power Sources* 2004;131:35–40.
 39. Borup RL, Vanderborgh NE. Design and testing criteria for bipolar plate materials for PEM fuel cell applications. *Mat Res Soc Symp Proc* 1995;393:151–5.
 40. Jung UH, Jeong SU, Park KT, Lee HM, Chun K et al. Improvement of water management in air-breathing and air-blowing PEMFC at low temperature using hydrophilic silica nanoparticles. *Intern J Hydrogen Energ*. In press, 2007.
 41. Li X, Sabir I, Park J. A flow channel design procedure for PEM fuel cells with effective water removal. *J Power Sources* 2007;163:933–42.
 42. Wu J, Yuan XZ, Wang H, Blanco M, Martin J, Wilkinson DP, et al. Durability of PEM fuel cells. Presented at: Hydrogen and Fuel Cells 2007 International Conference and Trade Show; 2007 Apr 29–May 3; Vancouver, Canada.
 43. Healy J, Hayden C, Xie T, Olson K, Waldo R, Brundage M, et al. Aspects of the chemical degradation of PFSA ionomers used in PEM fuel cells. *Fuel Cells* 2005;5:302–8.
 44. Knights SD, Colbow KM, St-Pierre J, Wilkinson DP. Aging mechanisms and lifetime of PEFC and DMFC. *J Power Sources* 2004;127:127–34.
 45. Meeker WQ, Escobar LA. Statistical methods for reliability data. New York: John Wiley and Sons, 1998.
 46. Nelson W. Accelerated testing: statistical models, test plans, and data analyses. New York: John Wiley and Sons, 1990.
 47. Hicks M. Membrane and catalyst durability under accelerated testing. In: Conference Proceedings of Fuel Cell Durability: Stationary, Automotive, Portable; 2005 Dec 8–9; Washington, DC. Brookline, MA: Knowledge Press; 2005.
 48. Bonneville Power Administration [homepage on the Internet]. Portland, OR: Bonneville Power Administration; c2008 [updated 2004 Apr 19]. PEM fuel cells. Available from: http://www.bpa.gov/energy/n/tech/fuel_cell/pem_fuel_cells.cfm.
 49. Fueleconomy.gov [homepage on the Internet]. Washington, DC: US Environmental Protection Agency; c2008 [updated 2008 Apr 18]. How they work: fuel cell systems. Available from: http://www.fueleconomy.gov/feg/fcv_components.shtml#.
 50. Millett S, Mahadevan K. Commercialization scenarios of polymer electrolyte membrane fuel cell applications for stationary power generation in the United States by the year 2015. *J Power Sources* 2005;150:187–91.
 51. BatteryUniversity.com [homepage on the Internet]. Richmond, Canada: Cadex Electronics Inc.; c2008 [updated 2006 Nov]. The miniature fuel cell. Available from: <http://www.batteryuniversity.com/parttwo-52A.htm>.
 52. Wang B. Recent development of non-platinum catalysts for oxygen reduction reaction. *J Power Sources* 2005;152:1–15.

53. Neyerlin KC, Gu W, Jorne J, Gasteiger HA. Determination of catalyst unique parameters for the oxygen reduction reaction in a PEMFC. *J Electrochem Soc* 2006;153:A1955–63.
54. Ilevbare GO, Scully JR. Oxygen reduction reaction kinetics on chromate conversion coated Al-Cu, Al-Cu-Mg, and Al-Cu-Mn-Fe intermetallic compounds. *J Electrochem Soc* 2001;148:B196–207.
55. Neyerlin KC, Gasteiger HA, Mittelsteadt CK, Jorne J, Gu W. Effect of relative humidity on oxygen reduction kinetics in a PEMFC. *J Electrochem Soc* 2005;152:A1073–108.
56. Xu, Song Y, Kunz HR, Fenton JM. *J Electrochem Soc* 2005;152(9):A1828–36.
57. Prakash J, Joachin H. Electrocatalytic activity of ruthenium for oxygen reduction in alkaline solution. *Electrochim Acta* 2000;45:2289–96.
58. Otero R, Calleja F, García-Suárez VM, Hinarejos JJ, de la Figuera J, Ferrer J, et al. Tailoring surface electronic states via strain to control adsorption: O/Cu/Ru(0 0 0 1). *Surf Sci* 2004;550:65–72.
59. Xu Y, Mavrikakis M. Adsorption and dissociation of O₂ on gold surfaces: effect of steps and strain. *J Phys Chem B* 2003;107:9298–307.
60. Stiehl JD, Kim TS, McClure SM, Mullins CB. Evidence for molecularly chemisorbed oxygen on TiO₂ supported gold nanoclusters and Au(111). *J Am Chem Soc* 2004;126:1606–7.
61. Fernández JL, Walsh DA, Bard AJ. Thermodynamic guidelines for the design of bimetallic catalysts for oxygen electroreduction and rapid screening by scanning electrochemical microscopy. M–Co (M: Pd, Ag, Au). *J Am Chem Soc* 2005;127:357–365
62. Shen Y, Bi L, Liu B, Dong S. Simple preparation method of Pd nanoparticles on an Au electrode and its catalysis for dioxygen reduction. *New J Chem* 2003;27:938–41.
63. Lin Y, Cui X, Ye X. Electrocatalytic reactivity for oxygen reduction of palladium-modified carbon nanotubes synthesized in supercritical fluid. *Electrochem Commun* 2005;7:267–274
64. Demarconnay L, Coutanceau C, Léger JM. Electroreduction of dioxygen (ORR) in alkaline medium on Ag/C and Pt/C nanostructured catalysts: effect of the presence of methanol. *Electrochim Acta* 2004;49:4513–21.
65. Ohno S, Yagyu K, Nakatsuji K, Komori F. Dissociation preference of oxygen molecules on an inhomogeneously strained Cu(0 0 1) surface. *Surf Sci* 2004;554:183–92.
66. Lescop B, Jay J-Ph, Fanjoux G. Reduction of oxygen pre-treated Ni(111) by H₂ exposure: UPS and MIES studies compared with Monte Carlo simulations. *Surf Sci* 2004;548:83–94.
67. Mentus SV. Oxygen reduction on anodically formed titanium dioxide. *Electrochim Acta* 2004;50:27–32.
68. Limoges BR, Stanis RJ, Turner JA, Herring AM. Electrocatalyst materials for fuel cells based on the polyoxometalates [PMo_(12-n)VnO₄₀]^{(3 + n)-} (n = 0–3). *Electrochim Acta* 2005;50:1169–79.
69. Lee K, Ishihara A, Mitsushima S, Kamiya N, Ota K. Stability and electrocatalytic activity for oxygen reduction in WC + Ta catalyst. *Electrochim Acta* 2004;49:3479–85.
70. Hayashi M, Uemura H, Shimanoe K, Miura N, Yamazoe N. Reverse micelle assisted dispersion of lanthanum manganite on carbon support for oxygen reduction cathode. *J Electrochem Soc* 2004;151:A158–63.
71. Yoshimoto S, Inukai J, Tada A, Abe T, Morimoto T, Osuka A, et al. Adlayer structure of and electrochemical O₂ reduction on cobalt porphine-modified and cobalt octaethylporphyrinmodified Au(1 1 1) in HClO₄. *J Phys Chem B* 2004;108:1948–54.

72. Chang CJ, Loh ZH, Shi C, Anson FC, Nocera DG. Targeted proton delivery in the catalyzed reduction of oxygen to water by bimetallic Pacman porphyrins. *J Am Chem Soc* 2004;126:10013–20.
73. Shen Y, Liu J, Jiang J, Liu B, Dong S. Fabrication of a metalloporphyrin-polyoxometalate hybrid film by a layer-by-layer method and its catalysis for hydrogen evolution and dioxygen reduction. *J Phys Chem B* 2003;107:9744–8.
74. Araki K, Dovidauskas S, Winnischofer H, Alexiou ADP, Toma HE. A new highly efficient tetra-electronic catalyst based on a cobalt porphyrin bound to four 3-oxo-ruthenium acetate clusters. *J Electroanal Chem* 2001;498:152–60.
75. Yoshimoto S, Tada A, Suto K, Itaya K. Adlayer structures and electrocatalytic activity for O₂ of metallophthalocyanines on Au(1 1 1): in situ scanning tunnelling microscopy study. *J Phys Chem B* 2003;107:5836–43.
76. Zhang CX, Liang HC, Kim E, Shearer J, Helton ME, Kim E, et al. Tuning copper-dioxygen reactivity and exogenous substrate oxidations via alterations in ligand electronics. *J Am Chem Soc* 2003;125:634–5.
77. Kieber-Emmons MT, Schenker R, Yap GPA, Brunold TC, Riordan CG. Spectroscopic elucidation of a peroxo Ni₂(μ-O₂) intermediate derived from a nickel(I) complex and dioxygen. *Angew Chem Int Ed* 2004;43:6716–18.
78. Aboeella NW, Lewis EA, Reynolds AM, Brennessel WW, Cramer CJ, Tolman WB. Snapshots of dioxygen activation by copper: the structure of a 2002;1:1 Cu/O₂ adduct and its use in syntheses of asymmetric bis(-oxo) complexes. *J Am Chem Soc* 124: 10660–1.
79. Wagner N, Schnurnberger W, Mueller B, Lang M. Electrochemical impedance spectra of solid-oxide fuel cells and polymer membrane fuel cells. *Electrochim Acta* 1998;43:3785–93.
80. Wendt H, Spinacé EV, Oliveira Neto A, Linardi M. Electrocatalysis and electrocatalysts for low temperature fuel cells: fundamentals, state of the art, research and development. *Quim Nova* 2005;28:1066–75.
81. Santiago EI, Batista MS, Assaf EM, Ticianelli EA. Mechanism of CO tolerance on molybdenum-based electrocatalysts for PEMFC. *J Electrochem Soc* 2004; 151: A944–9.
82. Papageorgopoulos DC, de Heer MP, Keijzer M, Pieterse JAZ, de Bruijn FA. Nonalloyed carbon-supported PtRu catalysts for PEMFC applications. *J Electrochem Soc* 2004; 151: A763–8.
83. Lu G, Cooper JS, McGinn PJ. SECM characterization of Pt–Ru–WC and Pt–Ru–Co ternary thin film combinatorial libraries as anode electrocatalysts for PEMFC. *J Power Sources* 2006; 161: 106–14.
84. Blum A, Duvdevani T, Philosoph M, Rudoy N, Peled E. Water-neutral micro direct-methanol fuel cell (DMFC) for portable applications. *J Power Sources* 2003; 117: 22–5.
85. Chang H, Kim JR, Cho JH, Kim HK, Choi KH. Materials and processes for small fuel cells. *Solid State Ionics* 2002; 148: 601–6.
86. Rice C., Ha S, Masel RI, Waszczuk P, Wieckowski A, Barnard T. Direct formic acid fuel cells. *J Power Sources* 2002; 111: 83–9.
87. Rice C, Ha S, Masel RI, Wieckowski A. Catalysts for direct formic acid fuel cells. *J Power Sources* 2003; 115: 229–35.
88. Ha S, Adams B, Masel RI. A miniature air breathing direct formic acid fuel cells. *J Power Sources* 2004; 128: 119–24.
89. Zhu Y, Ha S, Masel RI. High power density direct formic acid fuel cells. *J Power Sources* 2004; 130: 8–14.
90. Ha S, Larsen R, Zhu Y, Masel RI. Direct formic acid fuel cells with 600Acm⁻² at 0.4V and 22 °C. *Fuel Cells* 2004; 4: 337–43.

91. Qian W, Wilkinson DP, Shen J, Wang H, Zhang J. Architecture for portable direct liquid fuel cells. *J Power Sources* 2006; 154: 202–13.
92. Parsons TV. The oxidation of small organic molecules: A survey of recent fuel cell related research. *J Electroanal Chem* 1988; 257: 9–45.
93. Gupta SS, Datta J. Electrode kinetics of ethanol oxidation on novel CuNi alloy supported catalysts synthesized from PTFE suspension. *J Power Sources* 2005; 145: 124–32.
94. Lamy C, Lima A, LeRhun V, Delime F, Coutanceau C, Léger JM. Recent advances in the development of direct alcohol fuel cells (DAFC). *J Power Sources* 2002; 105: 283–96.
95. Vigier F, Coutanceau C, Hahn F, Belgsir EM, Lamy C. On the mechanism of ethanol electro-oxidation on Pt and PtSn catalysts: electrochemical and in situ IR reflectance spectroscopy studies. *J Electroanal Chem* 2004; 563: 81–9.
96. Raicheva SN, Christov MV, Sokolova EI. Effect of the temperature on the electrochemical behaviour of aliphatic alcohols. *Electrochim Acta* 1981; 26: 1669–76.
97. Ota K, Nakagawa Y, Takahashi M. Reaction products of anodic oxidation of methanol in sulfuric acid solution. *J Electroanal Chem* 1984; 179: 179–86.
98. Andreadis G, Song S, Tsiakaras P. Direct ethanol fuel cell anode simulation model. *J Power Sources* 2006; 157: 657–65.
99. Wang ZB, Yin GP, Zhang J, Sun YC, Shi PF. Investigation of ethanol electrooxidation on a Pt–Ru–Ni/C catalyst for a direct ethanol fuel cell. *J Power Sources* 2006; 160: 37–43.
100. Lux KW, Cairns EJ. Lanthanide-platinum intermetallic compounds as anode electrocatalysts for direct ethanol PEM fuel cells. *J Electrochem Soc* 2006; 153: A1139–47.
101. Lux KW, Cairns EJ. Lanthanide-platinum intermetallic compounds as anode electrocatalysts for direct ethanol PEM fuel cells. *J Electrochem Soc* 2006; 153: A1132–38.
102. Zhou WJ, Li WZ, Song SQ, Zhou ZH, Jiang LH, Sun GQ, et al. Bi- and tri-metallic Pt-based anode catalysts for direct ethanol fuel cells. *J Power Sources* 2004; 131: 217–23.
103. Oliveira Neto A, Giz MJ, Perez J, Ticianelli EA, Gonzalez ER. The electro-oxidation of ethanol on Pt-Ru and Pt-Mo particles supported on high-surface-area carbon. *J Electrochem Soc* 2002; 149: A272–9.
104. Colmati F, Antolini E, Gonzalez ER. Ethanol oxidation on carbon supported Pt-Sn electrocatalysts prepared by reduction with formic acid. *J Electrochem Soc* 2007; 154: B39–47.
105. Zhou WJ, Song SQ, Li WZ, Sun GQ, Xin Q, Kontou S, et al. Pt-based anode catalysts for direct ethanol fuel cells. *Solid State Ionics* 2004; 175: 797–803.
106. Rousseau S, Coutanceau C, Lamy C, Léger JM. Direct ethanol fuel cell (DEFC): Electrical performances and reaction products distribution under operating conditions with different platinum-based anodes. *J Power Sources* 2006; 158: 18–24.
107. Song SQ, Zhou WJ, Zhou ZH, Jiang LH, Sun GQ, Q. Xin, et al. Direct ethanol PEM fuel cells: The case of platinum based anodes. *Intern J Hydrogen Energy* 2005; 30: 995–1001.
108. Wang H, Jusys Z, Behm RJ. Ethanol electro-oxidation on carbon-supported Pt, PtRu and Pt₃Sn catalysts: A quantitative DEMS study. *J Power Sources* 2006; 154: 351–9.
109. Gupta SS, Mahapatra SS, Datta J. A potential anode material for the direct alcohol fuel cell. *J Power Sources* 2004; 131: 169–74.
110. Rhee YW, Ha S, Rice C, Masel RI. Crossover of formic acid through Nafion® membranes. *J Power Sources* 2003; 117:35–8.

111. Lee J, Christoph J, Strasser P, Eiswirth M, Ertl G. Spatio-temporal interfacial potential patterns during the electrocatalyzed oxidation of formic acid on Bi-modified Pt. *J Chem Phys* 2001; 115: 1485–92.
112. Becerik İ, Kadirgan F. Electr-oxidation of formic acid on highly dispersed platinum and perchlorate doped polypyrrole electrodes. *J Electrochem Soc* 2001; 148: D49–54.
113. Zhao M, Rice C, Masel RI, Waszczuk P, Wieckowski A. Kinetic study of electro-oxidation of formic acid on spontaneously-deposited Pt/Pd nanoparticles. *J Electrochem Soc* 2004; 151: A131–6.
114. Larsen R, Masel RI. Kinetic study of CO tolerance during electeo-oxidation of formic acid on spontaneously deposited Pt/Pd and Pt/Ru nanoparticles. *Electrochem Solid-State Lett* 2004; 7: A148–50.
115. Zhang L, Lu T, Bao J, Tang Y, Li C. Preparation method of an ultrafine carbon supported Pd catalyst as an anodic catalyst in a direct formic acid fuel cell. *Electrochem Commun* 2006; 8: 1625–7.
116. Zhang L, Tang Y, Bao J, Lu T, Li C. A carbon-supported Pd-P catalyst as the anodic catalyst in a direct formic acid fuel cell. *J Power Sources* 2006; 162: 177–9.
117. Larsen R, Zakzeski J, Masel RI. Unexpected activity of palladium on vanadia catalysts for formic acid electro-oxidation. *Electrochem Solid-State Lett* 2005; 8: A291–3.
118. Weber M, Wang JT, Wasmus S, Savinell RF. Formic acid oxidation in a polymer electrolyte fuel cell. *J Electrochem Soc* 1996; 143: L158–60.
119. Pukrushpan JT, Stefanopoulou AG, Peng H. *Control of Fuel Cell Power Systems: Principles, Modeling, Analysis, and Feedback Design*. London Berlin Heidelberg New York Hong Kong Milan Paris Tokyo: Springer, 2004; 31–56.
120. Amphett JC, Baumert RM, Peppley RF, Roberge PR, Harris TJ. Performance modeling of the Ballard Mark IV solid polymer electrolyte fuel cell. *J Electrochem Soc* 1995; 142: 9–15.
121. Wroblowa H, Rao MLB, Damijanovic A, Bockris JO'M. Adsorption and kinetics at platinum electrodes in the presence of oxygen at zero net current. *J Electroanal Chem* 1967; 15: 139–50.
122. Bockris JO'M, Srinivasan S. *Fuel Cells: Their Electrochemistry*. New York: McGraw-Hill, 1969.
123. Appleby AJ. Oxygen reduction on oxide-free platinum in 85% orthophosphoric acid: temperature and impurity dependence. *J Electrochem Soc* 1970; 117: 328–35.
124. Hoare JP. Rest potentials in the platinum-oxygen-acid system. *J Electrochem Soc* 1962; 109: 858–65.
125. Thacker R, Hoare JP. Sorption of oxygen from solution by noble metals: I. Bright platinum. *J Electroanal Chem* 1971; 30:1–14.
126. Cooper KR, Ramani V, Fenton JM, Kunz HR. *Experimental Methods and Data Analyses for Polymer Electrolyte Fuel Cells*, Edition 1.2. Scribner, 2005.
127. Ramani V, Kunz HR, Fenton JM. Investigation of Nafion[®]/HPA composite membranes for high temperature/low relative humidity PEMFC operation. *J Membr Sci* 2004; 232: 31–44.
128. Ramani V, Kunz HR, Fenton JM. Stabilized composite membranes and membrane electrode assemblies for elevated temperature/low relative humidity PEFC operation. *J Power Sources* 2005; 152: 182–8.
129. Song Y, Fenton JM, Kunz HR, Bonville LJ, Williams MV. High-performance PEMFCs at elevated temperatures using Nafion 112 membranes. *J Electrochem Soc* 2005; 152: A539–44.
130. Clegghorn S, Kolde J, Liu W. *Handbook of Fuel Cells: Fundamentals, Technology and Applications (Vol. 3)*. In: Vielstich W, Gasteiger HA, Lamm A, editors. Chichester: John Wiley & Sons, 2003; 566–75.

131. Yu J, Matsuura T, Yoshikawa Y, Islam MN, Hori M. In situ analysis of performance degradation of a PEMFC under nonsaturated humidification. *Electrochem Solid-State Lett* 2005; 8: A156–8.
132. Paganin VA, Sitta E, Iwasita T, Vielstich W. Methanol crossover effect on the cathode potential of a direct PEM fuel cell. *J Appl Electrochem* 2005; 35: 1239–43.
133. Jiang R, Chu D. Comparative Studies of Methanol Crossover and Cell Performance for a DMFC. *J Electrochem Soc* 2004; 151: A69–76.
134. Bard AJ, Faulkner LR. *Electrochemical Methods: Fundamentals and applications* (2nd edition). New York: John Wiley and Sons, 2001.
135. Vogel W, Lundquist J, Ross P, Stonehart P. Reaction pathways and poisons—II: The rate controlling step for electrochemical oxidation of hydrogen on Pt in acid and poisoning of the reaction by CO. *Electrochim Acta* 1975; 20: 79–93.
136. Jiang J, Kucernak A. Investigations of fuel cell reactions at the composite microelectrodesolid polymer electrolyte interface. I. Hydrogen oxidation at the nanostructured PtNafion[®] membrane interface. *J Electroanal Chem* 2004; 567: 123–37.
137. Markovic NM, Grgur BN, Ross PN. Temperature-Dependent Hydrogen Electrochemistry on Platinum Low-Index Single-Crystal Surfaces in Acid Solutions. *J Phys Chem B* 1997; 101: 5405–13.
138. Parthasarathy A, Srinivasan S, Appleby AJ. Temperature dependence of the electrode kinetics of oxygen reduction at the platinum/Nafion interface—a microelectrode investigation. *J Electrochem Soc* 1992; 139: 2530–7.
139. Appleby AJ, Baker BS. Oxygen reduction on platinum in trifluoromethane sulfuric acid. *J Electrochem Soc* 1978; 125: 404–6.
140. Damjanovic A, Genshaw MA. Dependence of the kinetics of O₂ dissolution at Pt on the conditions for adsorption of reaction intermediates. *Electrochim Acta* 1970; 15: 1281–3.
141. Damjanovic A, Brusic V. Electrode kinetics of oxygen reduction on oxide-free platinum electrodes. *Electrochim Acta* 1967; 12: 615–28.
142. Appleby AJ. Evolution and reduction of oxygen on oxidized platinum in 85% orthophosphoric acid. *J Electroanal Chem* 1970; 24: 97–117.
143. Yeager E. Electrocatalysts for O₂ reduction. *Electrochim Acta* 1984; 29: 1527–37.
144. Clouser SJ, Huang JC, Yeager E. Temperature dependence of the Tafel slope for oxygen reduction on platinum in concentrated phosphoric acid. *J Appl Electrochem* 1993; 23: 597–605.
145. Damjanovic A. Temperature dependence of symmetry factors and the significance of experimental activation energies. *J Electroanal Chem* 1993; 355: 57–7.
146. Mello RMQ, Ticianelli EA. Kinetic study of the hydrogen oxidation reaction on platinum and Nafion[®] covered platinum electrodes. *Electrochim Acta* 1997; 42: 1031–9.
147. Bockris JO'M, Gochev A. Temperature dependence of the symmetry factor in electrode kinetics. *J Electroanal Chem* 1986; 214: 655–74.
148. Ulstrup J. Temperature dependence of the transfer coefficient in electron and atom group transfer processes. *Electrochim Acta* 1984; 29: 1377–80.
149. Giner J, Hunter C. The mechanism of operation of the Teflon-bonded gas diffusion electrode: a mathematical model. *J Electrochem Soc* 1969; 116: 1124–30.
150. Springer TE, Raistrick ID. Electrical impedance of a pore wall for the flooded-agglomerate model of porous gas-diffusion electrodes. *J Electrochem Soc* 1989; 136: 1594–603.
151. Zhang J, Wang H, Wilkinson DP, Song D, Shen J, Liu Z. Model for the contamination of fuel cell anode catalyst in the presence of fuel stream impurities. *J Power Sources* 2005; 147: 58–71.

152. Nagerl K, Dietz H. Elektrochemisches Verhalten anodisch hergestellter Oxidschichten auf Platin. *Electrochim Acta* 1961; 4: 1–11.
153. Dietz H, Göhr H. Über den elektrochemischen Aufbau und Abbau von Sauerstoff- und Wasserstoff-Belegungen auf Platin in wässriger Lösung. *Electrochim Acta* 1963; 8: 343–59.
154. Damjanovic A, Bockris JO'M. The rate constants for oxygen dissolution on bare and oxide-covered platinum. *Electrochim Acta* 1966; 11: 376–7.
155. Sawyer DT, Day RJ. Kinetics for oxygen reduction at platinum, palladium and silver electrodes. *Electrochim Acta* 1963; 8: 589–94.
156. Li X. *Principle of Fuel Cells*. New York: Taylor and Francis, 2006.
157. Lim CY, Haas HR. A diagnostic method for an electrochemical fuel cell and fuel cell components. WO patent 2006029254, 2006.
158. Hirschenhofer JH, Stauffer DB, Engleman RR, Klett MG. *Fuel Cell Handbook* (4th edition). Reading PA: Parsons Corporation for U.S. Dept. of Energy, Office of Fossil Energy, Federal Energy Technology Center, 1998.
159. Ju H, Wang CY. Experimental validation of a PEM fuel cell model by current distribution data. *J Electrochem Soc* 2004; 151: A1954–60.
160. Srinivasan S, Ticianelli EA, Derouin CR, Redondo A. Advances in solid polymer electrolyte fuel cell technology with low platinum loading electrodes. *J Power Sources* 1988; 22: 359–75.
161. Srinivasan S, Velew OA, Parthasarathy A, Manko DJ, Appleby AJ. High energy efficiency and high power density proton exchange membrane fuel cells – electrode kinetics and mass transport. *J Power Sources* 1991; 36: 299–320.
162. Kim J, Lee SM, Srinivasan S. Modeling of proton exchange membrane fuel cell performance with an empirical equation. *J Electrochem Soc* 1995; 142: 2670–4.
163. Bevers D, Wöhr M, Yasuda K, Oguro K. Simulation of a polymer electrolyte fuel cell electrode. *J Appl Electrochem* 1997; 27: 1254–64.
164. Lee JH, Lalk TR, Appleby AJ. Modeling electrochemical performance in large scale proton exchange membrane fuel cell stacks. *J Power Sources* 1998; 70: 258–68.
165. Squadrito G, Maggio G, Passalacqua E, Lufano F, Patti A. An empirical equation for polymer electrolyte fuel cell (PEFC) behaviour. *J Appl Electrochem* 1999; 29: 1449–55.
166. Pisani L, Murgia G, Valentini M, D'Agurno B. A new semi-empirical approach to performance curves of polymer electrolyte fuel cells. *J Power Sources* 2002; 108: 192–203.
167. Amphlett JC, Baumert RM, Mann RF, Peppley BA, Roberge PR, Harris TJ. Performance modeling of the Ballard Mark IV solid polymer electrolyte fuel cell. *J Electrochem Soc* 1995; 142: 1–8.
168. Sena DR, Ticianelli EA, Paganin VA, Gonzalez ER. Effect of water transport in a PEFC at low temperatures operating with dry hydrogen. *J Electroanal Chem* 1999; 477: 164–70.
169. Büchi FN, Marek A, Scherrer GG. In situ membrane resistance measurements in polymer electrolyte fuel cells by fast auxiliary current pulses. *J Electrochem Soc* 1995; 142: 1895–901.
170. Mennola T, Mikkola M, Noponen M. Measurement of ohmic voltage losses in individual cells of a PEMFC stack. *J Power Sources* 2002; 112: 261–72.